UNIVERSITY OF WOLLONGONG AUSTRALIA

University of Wollongong - Research Online

Thesis Collection

Title: Charge collection in PET detectors

Author: Tony Young

Year: 2007

Repository DOI:

Copyright Warning
You may print or download ONE copy of this document for the purpose of your own research or study. The University does not authorise you to copy, communicate or otherwise make available electronically to any other person any copyright material contained on this site.
You are reminded of the following: This work is copyright. Apart from any use permitted under the Copyright Act 1968, no part of this work may be reproduced by any process, nor may any other exclusive right be exercised, without the permission of the author. Copyright owners are entitled to take legal action against persons who infringe their copyright. A reproduction of material that is protected by copyright may be a copyright infringement. A court may impose penalties and award damages in relation to offences and infringements relating to copyright material.
Higher penalties may apply, and higher damages may be awarded, for offences and infringements involving the conversion of material into digital or electronic form.

Unless otherwise indicated, the views expressed in this thesis are those of the author and do not necessarily represent the views of the University of Wollongong.

Research Online is the open access repository for the University of Wollongong. For further information contact the UOW Library: research-pubs@uow.edu.au

University of Wollongong Thesis Collections

University of Wollongong Thesis Collection

University of Wollongong *Year* 2007

Charge collection in PET detectors

Tony Young
University of Wollongong

Young, Tony, Charge collection in PET detectors, Master of Science - Research thesis, Faculty of Engineering, University of Wollongong, 2007. http://ro.uow.edu.au/theses/2690

This paper is posted at Research Online.

NOTE

This online version of the thesis may have different page formatting and pagination from the paper copy held in the University of Wollongong Library.

UNIVERSITY OF WOLLONGONG

COPYRIGHT WARNING

You may print or download ONE copy of this document for the purpose of your own research or study. The University does not authorise you to copy, communicate or otherwise make available electronically to any other person any copyright material contained on this site. You are reminded of the following:

Copyright owners are entitled to take legal action against persons who infringe their copyright. A reproduction of material that is protected by copyright may be a copyright infringement. A court may impose penalties and award damages in relation to offences and infringements relating to copyright material. Higher penalties may apply, and higher damages may be awarded, for offences and infringements involving the conversion of material into digital or electronic form.

Charge Collection in PET Detectors

By

Tony Young

Submitted in partial fulfilment of the requirements for the award of the degree of

Master of Science - Research

From

University of Wollongong

Faculty of Engineering

November, 2007

Acknowledgements

Many thanks to Dr Michael Lerch for his continued support and encouragement over the years. His enthusiasm for his research and his dedication to his students must be acknowledged. Without his input and assistance this project would have taken much longer to complete.

I'd also like to thank my family for supporting me as I completed this master's project. Their concern and encouragement spurred me on to complete this within the allotted time, even though I had started full time employment. Their patience and understanding was much appreciated.

Also, thanks must go to Dr Phil Simmonds and Michael Bailey for their assistance with Scintillation Program and DETECT2000. Thanks also to Dr Alexey Pan for profiling the LYSO crystals.

Also, thanks must go to the staff and post graduate students at the CMRP. Each contributed in some way or another and each effort was very much appreciated, whether it was discussions on different Monte Carlo code, to detector setup, or a break in work for coffee. I am grateful for all their guidance and help.

Thanks also to Sydney South West Area Health Service (SSWAHS), in particular Macarthur Cancer Therapy Centre for employing me whilst I was completing the thesis. The one day of allotted study time was appreciated!

Lastly, my deepest thanks must go to those who were with me during this project.

Abstract

Improving the spatial resolution in PET will increase the chance of accurate diagnosis of cancer. PET detectors are comprised in part of detectors such as photomultiplier tubes or solid state photodetectors optically coupled to scintillation materials, such as BGO or LSO. In this thesis a study of recently developed photodiode detectors, SPAD4 photodiodes, and LYSO crystals has been undertaken to investigate these properties.

As part of this research IV (current-voltage) and CV (capacitance-voltage) characterization measurements were carried out on the photodetectors and results indicate they are of excellent quality. Ion Beam Induced Charge Collection (IBICC) measurements were undertaken to fundamentally investigate the effect of bias on the efficiency and uniformity of charge collection within the photodetector. A reverse bias operating voltage of 50 V was eventually chosen as the optimum bias voltage for the SPAD4 photodiode for the gamma ray spectroscopy and timing resolution experiments that followed the IBICC characterisation. Charge collection uniformity was found to be excellent at this optimum voltage.

An investigation into the surface treatment of LYSO crystal and cladding was also completed. Physical measurements and simulations were conducted and the results are compared. Past simulation results have demonstrated that scintillation crystals produced a higher output when the surface was rough as opposed to the industry standard smooth polished surface [1]. Physical measurements and comparisons have also been completed with saw cut finish crystals and chemically etched crystals [2, 3]. Simulations were completed with "Scintillation Program", a simulation code developed at the CMRP, and DETECT2000. Measurements completed for this thesis produced no significant change in the deduced scintillator light output after roughening a crystal side.

Timing resolution in commercial PET scanners ranges from 8 to 16ns. Experimentally with a photomultiplier tube coupled to a photodiode, timing resolution as low as 9.4ns FWHM has been achieved [4]. Coincidence timing resolution measurements using standard NIM (Nuclear Instrumentation Module) electronic modules were taken with a

NaI-photomultiplier tube and the LYSO-SPAD4 photodiode module. The best result obtained was a FWHM coincident time resolution of 22 ns, which is similar to past results.

The SPAD4 photodiode and LYSO crystal combination show promise as the basis for a future PET detectors module, although further work needs to be completed to improve the timing performance.

Table of Contents

List of Figures

List of Tables

Notation/Abbreviation

CMRP = Centre for Medical Radiation Physics

UOW = University of Wollongong

PET = Positron Emission Tomography

CT = Computed Tomography

MRI = Magnetic Resonance Imaging

IBICC = Ion Beam Induced Charge Collection

PMT = Photomultiplier Tube

PD = Photodiode

LYSO = Lutetium Yttrium Oxyorthosilicate

LSO = Lutetium Oxyorthosilicate

BGO = Bismuth Germanium Oxide

GSO = Gadolinium Silicate

FWHM = Full Width at Half Maximum

IV = Current Voltage

CV = Capacitance Voltage

SLICE = Scintillator Light Collection Efficiency

Int = Integration

Diff = Differentiation

CFD = Constant Fraction Discriminator

TFA = Timing Filter Amplifier

TAC/SCA = Time to Amplitude Converter/Single Channel Analyser

Na–22 = Sodium 22

Cs–137 = Caesium 137

I-125 = Iodine 125

NECR = Noise Equivalent Count Rate

Publications List

Lerch, M.L., Simmonds, P.E., Young, T., Takacs, G.J., Rozenfeld, A., Perevertaylo, V. & Meikle, S., Modelling the readout performance of a new silicon photodetector for use in PET, IEEE Transactions on Nuclear Science (2007), Submitted.

Chapter 1 – Introduction

1.1 Overview of Project

Positron Emission Tomography (PET) is a medical imaging modality, providing information on the body's chemistry, cell function and disease location. PET creates an image from the uptake of radiotracer in the body providing physiological information, as opposed to other conventional imaging modalities such as x-rays, CT or MRI, which provide mainly anatomical information, though MRI can provide some physiological information.

PET has many advantages over a similar nuclear medicine imaging modality named Single Photon Emission Computerised Tomography (SPECT). The greatest advantage of PET is that a PET study is able to provide physiologic and metabolic information which SPECT cannot [7]. Attenuation corrections are inherently more accurate in PET than in SPECT as the pair of annihilation photons define a line through the patient such that the total path length through the patient is always traversed when a decay is detected. PET scans are also much quicker than SPECT scans, and PET also provides better spatial resolution [8].

Detector modules in PET systems have many requirements. These include good signal production and charge collection, with these being important aspects in the quality of the PET imaging. Having good charge collection characteristics produces improved energy and time resolution, which is imperative in producing high quality PET images. The Centre for Medical Radiation Physics (CMRP) has designed and is developing a new PET detector module to improve the spatial resolution by restricting the detector interaction point of the 511 keV γ-rays to a 3x3x3 mm^3 voxel. The new PET detector module is comprised of an 8x8 array of silicon photodetectors (here on referred to as SPAD4) optically coupled to an 8x8 array of Lutetium Yttrium Oxyorthosilicate (LYSO) crystals that are optically isolated from one another.

1.2 Reasons for Research

This research was conducted to determine the suitability of the new SPAD4 photodiodes and LYSO crystals for the application of PET. This involved investigations into the charge collection capabilities of the SPAD4 photodiodes and LYSO crystals, along with the coincidence timing resolution. Improvements in both energy and timing resolutions, along with charge collection efficiency using these detectors and crystals as opposed to current detector and crystal setups used in PET may increase the chances of accurate diagnosis of disease and of cancer.

1.3 Aims/Objectives

The objective of this research was to determine the suitability of the new SPAD4 photodiodes for the application of PET. This involved investigations into the charge collection properties of the SPAD4 detectors, the light conversion properties of the LYSO crystals used and the coincidence timing resolution properties of the LYSO crystals and SPAD4 detectors when combined to form a detection module.

The aim of investigating the charge collection properties was fulfilled through measurements of the SPAD 4 IV characteristics, CV characteristics and Ion Beam Induced Charge Collection (IBICC) measurements.

The aim of investigating the light collection properties of LYSO scintillator crystal was completed by profiling the LYSO crystal surface using an in-house developed Monte Carlo simulation package known as “Scintillation Program”. The results were compared with those from a well known commercial package, DETECT2000. The simulation results were then verified experimentally.

Another aim was to investigate the timing properties of different detectors used in PET; namely photomultiplier tubes (PMT) and the new SPAD photodiodes (PD). This began initially with electronics tests with NIM modules and characterisation of PMTs and PDs. Coincidence timing measurements were then completed using a PMT coupled with a PD, with measurements also taken using a double gating technique.

1.4 Thesis Outline

The work conducted and presented in this thesis is divided into different chapters. The first chapter has introduced the work, and provided the aims and reasons for research. A literature review is provided in chapter 2. Chapter 2 also provides theory on the main components used.

Chapters 3, 4 and 5 present the main bodies of research conducted. Chapter 3 presents the methodology and results of an Ion Beam Induced Charge Collection (IBICC) study into the SPAD4 detectors. Chapter 4 gives the results of an investigation into altering the scintillation light output of the LYSO crystals used. This includes experimental surface profiling, the Monte Carlo simulation work and experimental collection efficiency measurements using LYSO crystal and the SPAD4 photodiodes. Chapter 5 presents coincidence timing measurements using LYSO crystal coupled to the SPAD4 detector and a photomultiplier tube.

Chapter 6 provides conclusions and discussions into the work completed, along with suggestions for future work.

Chapter 2 – Theory

2.1 Literature Review

2.1.1 Positron Emission Tomography

Positron Emission Tomography (PET) is a medical imaging tool which provides information on the body's chemistry, cell function and disease location. Radiotracers are used to produce an image through quantifying *in vivo* physiological and biochemical processes.

PET is a functional imaging technique. PET however has a poor spatial resolution in the final image when compared to both CT and MRI images. CT and MRI scans provide mainly anatomical information, and MRI gives some physiological information, whereas PET scans reveal a quantitative distribution of radiotracer uptake within the region of interest. Thus PET reveals both molecular function and activity, not structure, and can thus differentiate between normal and abnormal (cancer/tumour) or live versus dead tissue. Therefore, from the resultant image, the physician is able to better understand the complexity of the disease, the staging of the disease and from this information, the subsequent treatment [5].

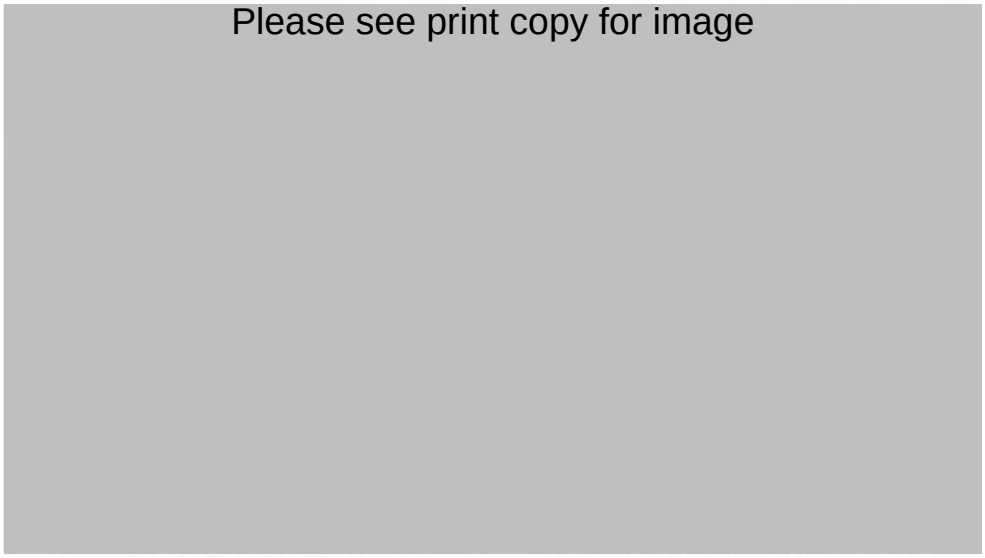

Figure 2.1: Basic Physics of Positron Emission Tomography [6]

In PET the radiation detected is due to the interaction of positrons and electrons, resulting in an annihilation reaction. This annihilation reaction produces two 511 keV annihilation photons which are emitted in opposite directions, thus giving a means for localisation of the origin of the photons and the radioactive decay process of the photons. In a typical PET system, the patient is surrounded by a ring of detectors. When detectors on opposite sides of the patient register annihilation photons within a coincidence timing window, the positron electron annihilation is assumed to have occurred along the line of response connecting the two detectors. Thus the PET image reveals the number of decays, or counts, occurring in each of the voxels represented by pixels in the image [7].

The most common PET tracer is 2-fluoro-2-deoxy-D-glucose, FDG, which is a compound of positron emitter Fluorine–18 and has a half life of approximately 110 minutes. Biological tissues, such as muscle, take up this compound in a similar way the glucose is taken up as fuel. Cancerous tumours metabolise glucose at a greater rate than normal tissue, and thus FDG becomes concentrated within a tumour, with this greater amount of uptake showing up in a PET scan. Other PET tracers include such radioisotopes as Oxygen-15, Carbon-11 and Nitrogen-13, though these are not as commonly used as FDG. These radioisotopes have much shorter half lives than FDG, with Oxygen-15 having a half life of 2 minutes, Carbon-11 approximately 20 minutes, and Nitrogen-13 approximately 10 minutes. Though all of these radioisotopes are positron emitters, they follow different metabolic functions, with Oxygen-15 becoming a part of the blood flowing in the patient, Carbon-11 used for radioactive labelling of molecules in PET, and Nitrogen-13 used to tag ammonia molecules for PET. However use of these radioisotopes is limited by their short half lives [9].

Timing resolution is a critical part of the localisation of an annihilation event along the line of response. The coincidence timing resolution is defined by the distribution in time of coincident events detected between two detectors. It is measured with a time to amplitude converter and a multi channel analyser. It is expressed as full width at half maximum [10]. Thus the better the coincidence timing resolution, the greater the accuracy of the PET system. A smaller coincidence timing resolution would mean a

smaller time interval in which one photon would need to be detected in order to be accepted in coincidence with another detected photon. This would thus reduce random and scattered coincidences from being recorded, therefore improving the final image. Random coincidences occur when two photons not arising from the same annihilation event are incident on the detectors within the coincidence time window of the system. The scatter coincidence is one in which at least one of the detected photons has undergone at least one scattering event prior to detection. As the direction of the photon is changed during the scattering process, the resulting coincidence event will then be assigned to the incorrect line of response. Scatter coincidences may include events in which either one or both photons have been scattered to produce a coincidence event. A reduction of these would result in a reduction of statistical noise in the system [8].

Improved timing accuracy in PET could allow many advantages. The random event rate may be reduced by using a narrower coincidence timing window, thus increasing the peak Noise Equivalent Count Rate (NECR). Improved timing accuracy would also allow use of time-of-flight in the reconstruction algorithm. Time-of-flight reconstruction involves the accurate measurement of the difference in arrival times of the two annihilation photons. This would constrain the position of the positron to a point rather than a line, so three dimensional images could be obtained without a reconstruction algorithm. Time-of-flight reconstruction will also reduce the noise variance Also, emission and transmission data can be acquired simultaneously, reducing the total scan time. Axial blurring can be reduced by using the time-of-flight to determine the correct axial plane that each event originated from [11].

Studies into the suitability of photodiodes for PET have been conducted in the past, with the replacement of photomultiplier tubes with photodiodes showing a lot of potential if the timing properties can be improved [12]. Most of these studies have culminated in the development and production of small animal PET scanners, some even producing second generations of original small animal PET scanners, such as MADPET – II (Nuclear Medicine Clinic, Technische Universitat Munchen) and MicroPET II (University of California, Los Angeles (UCLA) and Concorde Microsystems, Knoxville) [13, 14, 15].

2.1.2 Ion Beam Induced Charge Collection

Ion Beam Induced Charge Collection (IBICC) is a powerful experimental technique to characterise semiconductor materials and devices. IBICC images the active regions in micro electronic devices, by measuring the induced current caused by a penetrating beam of focused ions or radiation. It also enables active regions to be assessed online for resistance to radiation and damage by radiation [16].

IBICC was initially developed for studying radiation damage of electrically active semi conductors [17, 18] and depletion regions of microelectronic devices [19, 20]. It now has been developed to the point where it can be used for studying the properties of different radiation detectors and with different ion beams [21, 22].

IBICC generally requires the use of a nuclear microprobe and ion beams of different energies. IBICC is accomplished by raster scanning a micron resolution heavy ion beam over the region of the device while the charge resulting from each ion strike is recorded. Charge is measured generally by connecting a charge sensitive preamplifier to the device. The beam position is recorded in an array of pixels, whilst the charge signal is converted into its associated pulse height spectrum associated with each pixel. Thus the charge collection information from one exposure produces a data cube, with this data reduced to a 2-D representation of charge by median filtering the spectral data and applying a colour spectrum to the resulting median charge collected at each pixel [16].

2.1.3 LYSO Scintillator Crystal

In a modern PET systems, an ideal scintillator would have high stopping power, high light output, fast decay time, be rugged, non hydroscopic, have no afterglow, be capable of being mass produced and be relatively inexpensive. Presently the most commonly used scintillator material used in PET systems is BGO ($Bi_4Ge_3O_{12}$). This scintillator has several drawbacks in that it has a low light output (15% of sodium iodide), a slow decay time (300 ns) and has an afterglow and colour centres [23], which is a defect in the regular spacing of atoms within a solid that absorbs visible light of a particular colour, or infrared or ultraviolet radiation which produces a characteristic colour to the solid.

LYSO ($Lu_{0.6}Y_{1.4}SiO_{0.5}$:Ce) stands for Lutetium Yttrium Oxyorthosilicate, and is the scintillator crystal investigated as part of this study. LYSO crystal has high light output, and good energy resolution. It also is a high density material, with a density of 5.37 g/cm^3 and with a fast decay time of 53 ns. Lutetium Oxyorthosilicate (LSO) has a slightly faster decay time of 40 ns. The refractive index refers to the light transmission properties of a material, and is a measure for how much the speed of light is reduced inside the material. LYSO has a refractive index of 1.81, and its peak emission wavelength is 420nm.

	Scintillator Materials			
	LYSO	**LSO**	**GSO**	**BGO**
Decay Time (ns) **(Fast/Slow Ratio)**	53	40	60 / 600 (7 / 1)	60 / 300 (1 / 10)
Light Output vs NaI (PMT) (%)	75	75	20	15
Light Output vs NaI (APD) (%)	85	85	40	30
Peak Emission (nm)	420	420	430	480
Index of Refraction	1.81	1.82	1.85	2.15
Density (g/cm^3)	5.37	7.35	6.71	7.13
Effective Z	54	65	58	73
1/μ 511 keV (mm)	20.0	12.3	15.0	11.6

Table 2.1 – Properties of Scintillators [3]

As may be seen from table 2.1, LYSO is faster and several times more efficient than BGO and GSO in converting absorbed gamma ray energy to light. The increased speed reduces the dead time of an individual PET detector module and thus allows for faster scan times. The higher light output improves the signal to noise ratio, improving the image quality. This may be seen in table 2.1, as LYSO has a much higher light output vs NaI than both GSO and BGO producing a 75% yield when compared to NaI, as opposed to 20% for GSO and 15% for BGO. $1/\mu$ is the inverse linear attenuation coefficient and defines λ, the mean free path. This defines the average distance travelled in the crystal before an interaction takes place [24]. LYSO has a slightly higher $1/\mu$ for 511 keV photons compared to LSO, GSO and BGO.

Studies on different surface treatments of LYSO have been conducted previously. Generally these studies involve a comparison between unpolished and chemically etched crystals [2, 3]. The general trend established by this research has been that the surface finish plays a large part in the light output and energy resolution obtained. Through chemical etching the light output was improved significantly for all sized LYSO crystals, with the energy resolution only improving dramatically for smaller crystals (2x2x10 mm^3 from [3]). Generally chemical etching also slightly reduces the weight of the crystals, with this possibly explaining the significant results for smaller crystals due to the larger surface to volume ratio.

The LYSO scintillator material was purchased from Crystal Photonics Inc. (CPI), Sanford, Florida, USA [25]. The LYSO was then cut into 3x3x3 mm^3 cubes and polished and the absolute light output was determined by A&D Precision Co., Newtown, MA, USA. The absolute light output was measured to be ~26 photons/keV, which is approximately 65% of the absolute light output of NaI (~40 photons/keV) which is a commonly used scintillator crystal [26].

2.1.4 SPAD Photodiodes

The SPAD detectors are silicon semiconductor photodiode detectors. They were designed at the Centre for Medical Radiation Physics at the University of Wollongong and were manufactured in collaboration with "SPA - BIT" detector, a Ukrainian microelectronics company. Different generations and versions of the SPAD photodiode have been created, each with slightly different characteristics to the other [26, 27, 28] as an investigation into the role of the optical entrance window in relation to the scintillator readout performance of the photodiode detector. The SPAD4 photodiode detector was the SPAD photodiode used in all the measurements presented in this thesis.

The SPAD detector used for the research described in this thesis is schematically shown in Figure 2.2. This single diode is a test structure made from the same wafer as the 8x8 arrays used in the new detector module. The SPAD4 is based on a 300 μm thick layer of high resistivity n-type silicon, with resistivity of 5 kΩcm (Wakar silicon). The SPAD4 has an active area of 3x3 mm^2, with the optical entrance window made up of a layer of silicon oxide (SiO_2), and a layer of silicon nitride (Si_3N_4). The SPAD4 photodiode consists of a p^+ anode and a p^+ guard ring and cathode connection. The SPAD4 optical entrance window appears grey in colour. The SPAD4 consists of a SiO_2 layer of 75 nm and a Si_3N_4 of 61 nm. This photodiode was designed to have a relatively low and flat transmission at λ = 420 nm for incident photons at all angles of incidence [27]. The over layers also protect the outer surface of the photodiode against dust and moisture and other external influences which may affect the dark current. If this wasn't present then ions may reach the surface and cause the formation of charge inversion layers beneath the surface, generating charges which would cause deterioration in the reverse current and add to the noise.

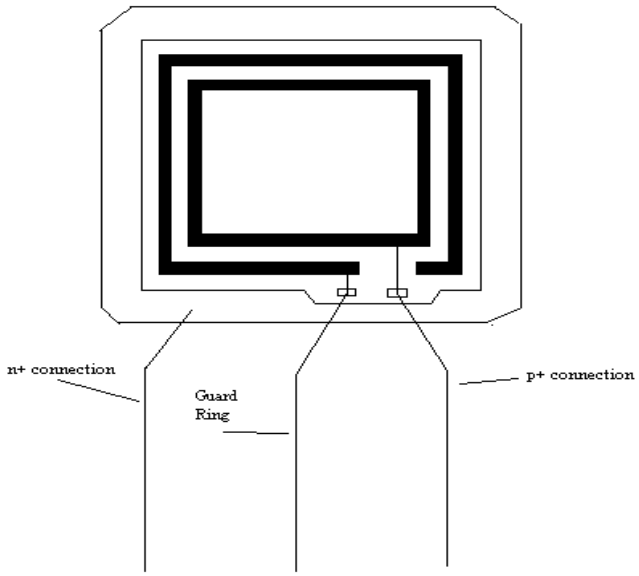

Figure 2.2: SPAD4 Photodiode Schematic

The main aim of the design of the SPAD4 detector is the blue wavelength detection enhancement of the photodiode. In this case the optical absorption curve of the photodiode better matches the optical emission curve of the LYSO scintillator. This design improves the photodiode's quantum efficiency at short wavelengths so as to collect every possible charge carrier while at the same time keeping noise from Auger recombination to a minimum. Auger recombination occurs when an electron and a hole recombine in a band to band transition and give off the resulting energy to another electron or hole. By minimising the noise from Auger recombination, the signal to noise ratio (SNR) should be maximised, allowing for good statistical data when reading out the scintillator crystal.

The optical entrance window contains a p^+ doped layer that is produced using a special boron implantation technique to heighten the electric field in the region very close to the surface of the PD. This is important in our case as the peak wavelength of the scintillation light emitted by the LYSO crystal is at 420 nm and is therefore has a typical absorption length of 0.1 microns in silicon [29]. When the PD is biased at full depletion, a greater electric field exists in the surface region, which correspondingly increases the drift velocities of the charge carriers in this region. This increased conductivity leads to faster

hole collection times, leading to more efficient charge collection because recombination of carriers is less likely and correspondingly, improved signal to noise is achieved. As the efficiency of the charge collection is high, and similar numbers of holes and electrons are collected, the signal is maximised, and thus may produce an improved SNR at shorter peaking times.

Also, by use of the special ion implantation technique, strong electric fields become embedded near the surface of the device. These regions of heightened electric fields ensure that the charges generated are more likely to be swept towards their collection contacts. This leads to a fast and effective charge collection, leading to a fast rise time of the detector signal for improved timing resolution and good energy resolution. Also, using this method, the dead layer may be minimised.

The SPAD detectors are operated at voltages so that they are fully depleted. This ensures the lowest possible capacitance, and thus keeps noise to a minimum and gives the fastest charge collection. If the detector is over biased, the signal waveform deteriorates, along with a loss in energy resolution. Thus the optimum bias is used at all times [30].

Chapter 3 – Ion Beam Induced Charge Collection

3.1 Current – Voltage Measurements

3.1.1 Current - Voltage Measurement Method

Current Voltage (IV) measurements of the SPAD4 photodiodes were carried out at the Australian Nuclear Science and Technology Organisation (ANSTO) in the device characterisation laboratory.

IV measurements were taken with the voltage running through the anode connection with the guard ring connection floating, and also through the guard ring connection with the anode connection floating. IV characteristics were measured for both forward bias and reverse bias.

A schematic of the SPAD4 photodiode is shown in figure 2.2. The p^+ is the anode and n^+ is the cathode. The SPAD4 consists of a 300 μm thick layer of 5kΩcm Wakar type high sensitivity silicon, with a SiO_2 layer of 68 nm and then a layer of Si_3N_4 of 60 nm. The "Metrics" Version 2.1 software was used to record the results. A Keithley 237 High Voltage Source Measure Unit was used to set the voltage and measure the resulting current.

3.1.2 Current - Voltage Measurement Results

The reverse bias IV measurement results are shown below. All the measured photodiodes follow the same trends, with only SPAD4 #2 showing a different response when compared to the other photodiodes. When this photodiode was tested later it was found that it was faulty, exhibiting high dark current when voltage was applied. The IV measurements corroborate this result. The photodiodes used in measurements throughout this thesis, SPAD4 #1, #6 and #7 all show similar IV responses, with very little variation in current produced with increase in bias voltage. The SPAD4 #6 was used in the IBIC measurements. The SPAD4 #1 and SPAD4 #6 were used in the crystal measurements. The SPAD4 #7 was used in the coincident timing resolution measurements.

a)

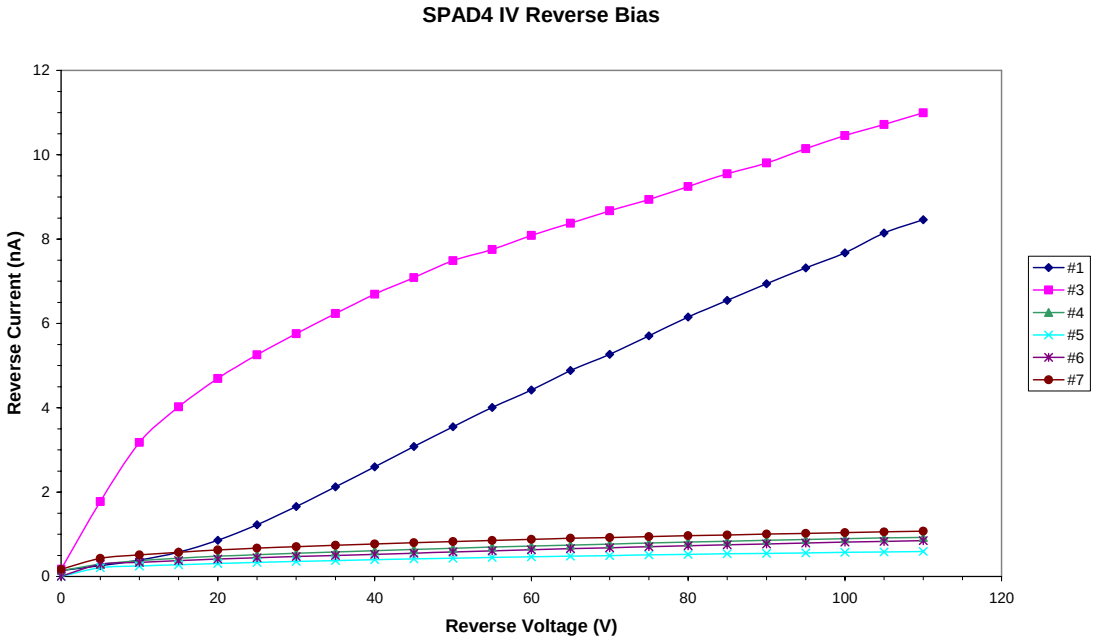

b)

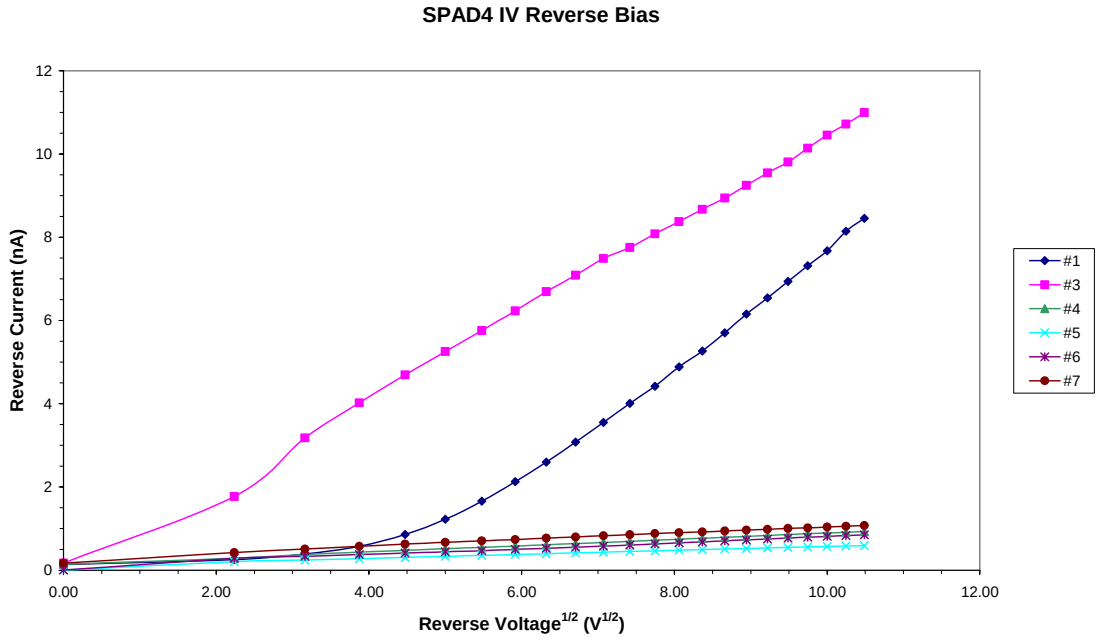

Figure 3.1: SPAD4 Reverse Bias IV Results, a) I vs V, b) I vs $V^{1/2}$

The figure 3.1 a) displays the I vs V relationship and b) displays the SPAD4 reverse bias results with a $V^{0.5}$ relation. Both the plots displayed in figure 3.1 have an approximately linear relationship between current and voltage. A linear relationship is not expected for these photodiodes. Generally with reversed biased diodes, the current increases slightly with increased voltage, in a linear relationship. A breakdown voltage is eventually reached as the voltage is increased further, producing a large increase in current [31]. However, even at a maximum reverse bias voltage of 110 V, breakdown of the SPAD4 was not observed, and thus only a linear relationship is observed.

The forward bias IV results for the SPAD4 photodiodes were also taken. All photodiodes show similar characteristics, with only measurements at a forward bias of 0.16 V taken so as to not damage the photodiodes. As these photodiodes are only operated at reverse bias the results are not entirely significant, though they are important in knowledge of the characteristics of these semiconductor detectors. SPAD4 #1 showed the greatest response when forward biased.

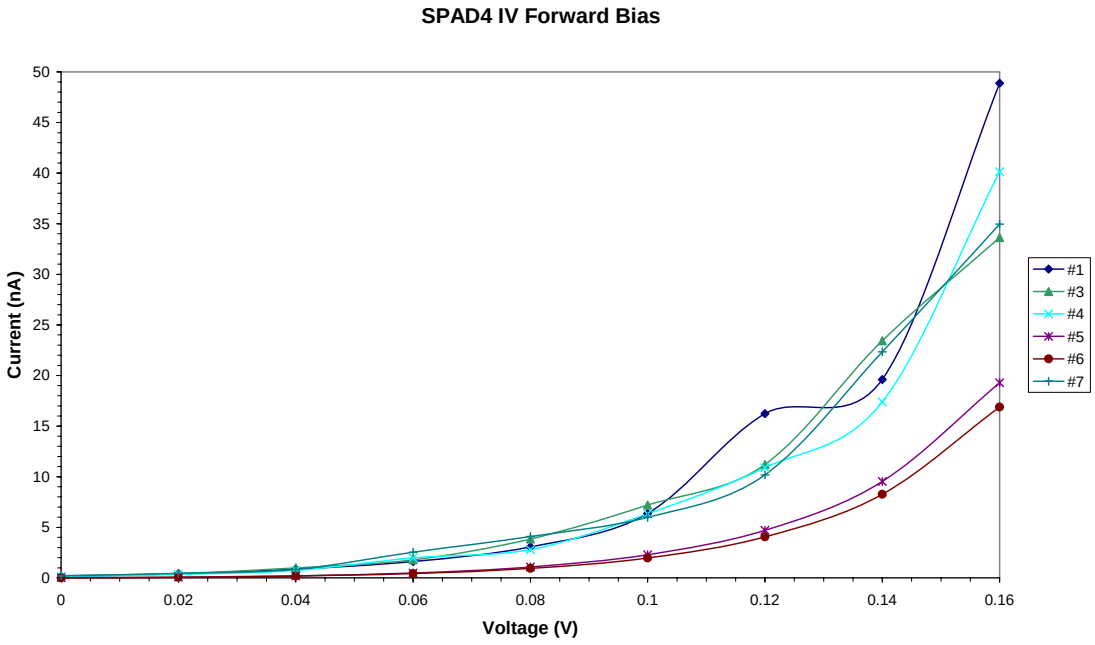

Figure 3.2: SPAD4 Forward Bias IV Results

The IV characteristics of the guard ring were also measured, though the guard ring has never been used in the past and did not have a bias voltage applied at all throughout any measurements conducted in this project. From the guard ring IV characteristics, it can be seen that SPAD4 #5 and #6 all reached breakdown between -80 V and -90 V. The other 2 SPAD4 guard rings which were measured, #1 and #7, did not reach breakdown voltage at all even at -110 V.

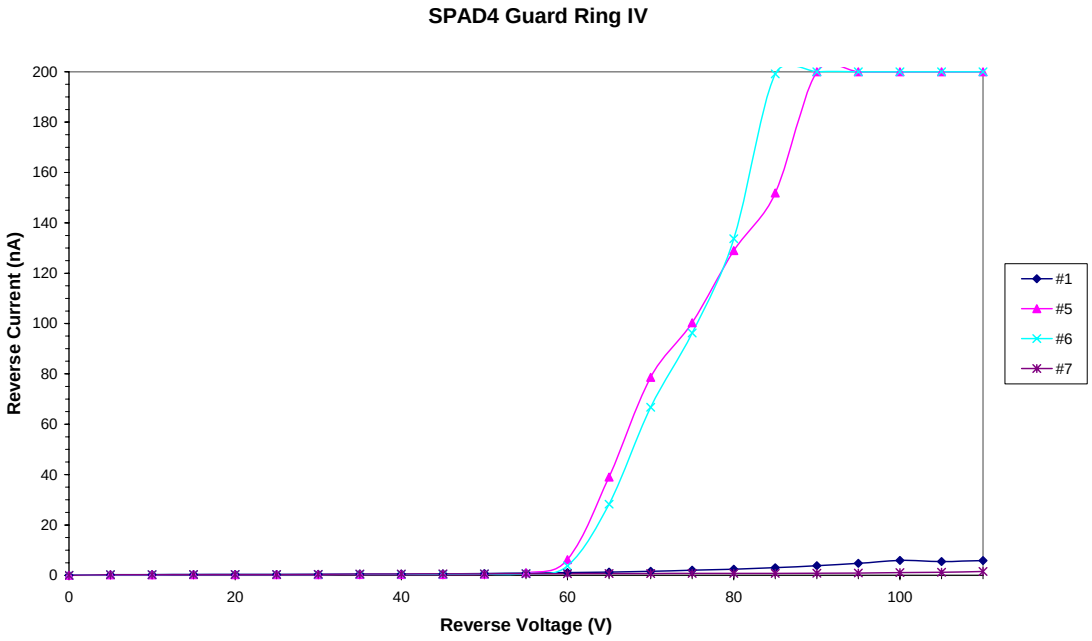

Figure 3.3: SPAD4 Guard Ring IV Results

3.2 Capacitance - Voltage Measurements

3.2.1 Capacitance - Voltage Measurement Method

Capacitance – Voltage (CV) measurements were also carried out at ANSTO in the device characterisation laboratory. A Boonton 7200 Capacitance Meter was used to set the voltage and measure the capacitance. As the response gradient changes the greatest at low voltages, more measurements were conducted at these lower voltages in order to account for any subtle changes which may occur here. All seven SPAD4 photodiode CV characteristics were measured. No bias was applied to the detector guard ring, which was left floating.

3.2.2 Capacitance - Voltage Measurement Results

The results for the SPAD4 CV measurements are shown in the figure below.

a)

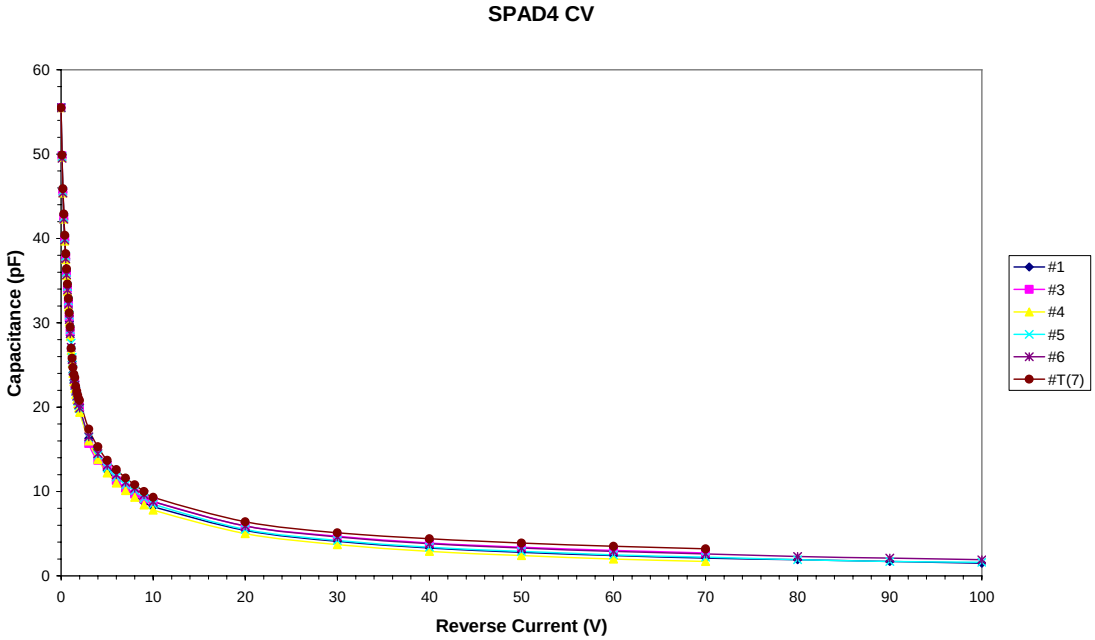

b)

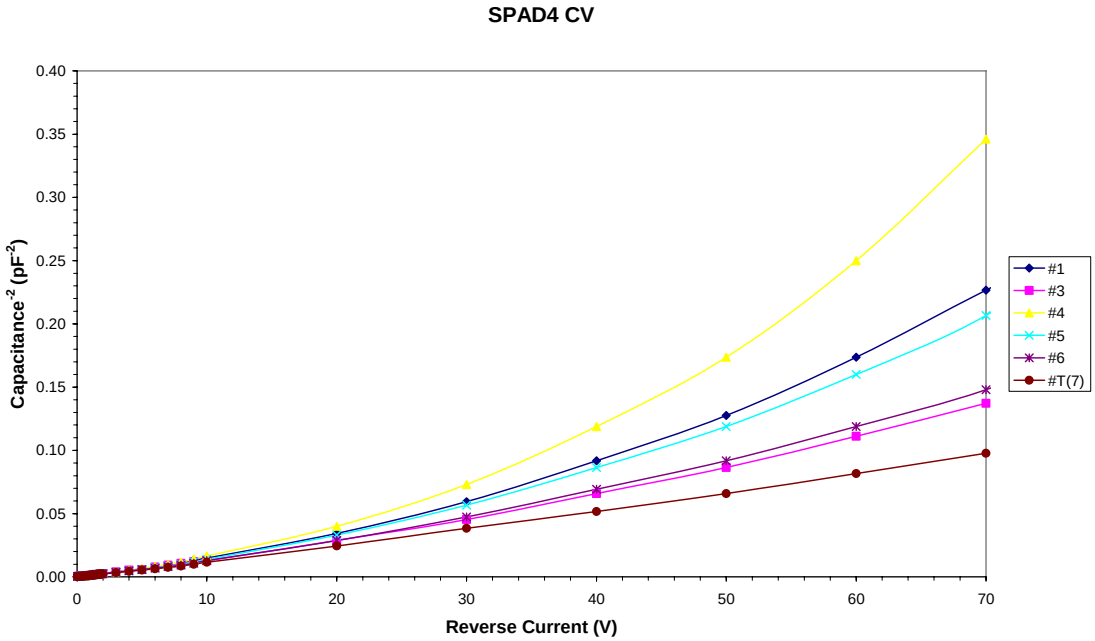

Figure 3.4: SPAD4 CV Results, a) C vs V, b) C^{-2} vs V

Initially measurements were taken up to a reverse bias voltage of 100 V, with very little change in results after 70 V found. Thus the measurements were completed up to 70 V after this was established. Figure 3.4 displays the results in both C vs V format and $1/C^{1/2}$ vs V format. The $1/C^{1/2}$ vs V plot allows estimation of the effective impurity concentration, if necessary.

As may be seen from figure 3.4 a), all the SPAD4 detectors measured have quite similar CV characteristics. Very little variation is seen between any of the SPAD4 photodiodes, with all the photodiodes measured having a capacitance result between 3 pF and 4 pF at a reverse bias of 50 V. As may be seen from the figure 3.4 a), the maximum variation seen between the SPAD4 photodiodes measured is approximately 2.5 pF. The results also approach a constant capacitance value, which indicate that full depletion has been reached. From figure 3.4 a), it could be estimated that full depletion is first achieved at approximately 40 V reverse bias.

3.3 Ion Beam Induced Charge Collection Measurements

3.3.1 Ion Beam Induced Charge Collection Measurement Method

IBICC facilities were originally added to the capabilities of the ANSTO heavy ion microprobe for studies into microdosimeters for hadron therapy, with studies into charge collection efficiency and the LET spectrum conducted [32, 33]. Similar methods were used in the study of the SPAD4 photodiode.

The IBICC measurements were carried out at ANSTO using ANTARES. A 5.5 MeV He^{+} beam was directed at the photodiode sample, and scanned across the sample, with the charge collected measured. Helium ions have been used in the past to study silicon photodiodes [35]. The results were recorded and analysed using the OMDAQ software. The IBICC measurements were taken using the SPAD4 #6.

Measurements were completed with both the guard ring and the anode having the same potential applied and with the guard ring floating. Measurements were taken with both the anode and guard ring held at 0 V to -50 V. Measurements were also taken with the anode and the guard ring floating from 0 V to – 100 V.

Generally when the SPAD4 photodiodes have been used in the past, the guard ring has not been used at all and has no bias applied to it, being left to “float”. The guard ring, if biased and used, needs to have the same bias voltage applied to it as the anode. If different bias voltages are used then a high leakage current is observed, and measurements are unable to be completed.

The measurements were conducted as had been done previously with microdosimeter devices at the CMRP [32, 33, 36, 37]. The SPAD4 photodiode which was to be scanned was attached to the sample holder and positioned in the beam scan area. The ion beam induced charge collection setup consists of a charge sensitive preamplifier (Amptek A250) mounted on a PC250 test board. A 10 pin electrical feed through provides power to the preamplifier, device bias, test pulse signal and charge collection signal to and from the target chamber. A spectroscopy amplifier was used to amplify and shape the

preamplifier output signal. Settings of 100 coarse gain and 0.7 fine gain, along with a 2 μs shaping time were used. The signal was then passed to an ADC channel of the data acquisition system in coincidence with signals indicating the beam position.

The Oxford Microbeam Data AcQuisition system (OMDAQ) consists of Windows based software, a scanning amplifier, ten 2048 channel Analogue to Digital Converters (ADCs) and a current integrator connected to the sample holder. The OMDAQ software stores the signal height for each pulse detected together with x and y beam coordinates as a data triplet, or event (E,x,y) in a file. This list mode file can be played back after the acquisition for re-analysis [36, 38].

The OMDAQ software also was used to convert the list mode spectra data to energy spectra. This software was also able to apply a median pulse height algorithm to each pulse height spectrum per pixel to generate a two dimensional image. This 256 x 256 pixel image is the median energy map. An investigation by Overley, *et. al.* produced a result in which the median selection provides better contrast. Median filtering reduces noise and sharpens certain features, and also produces localisation of features to within 10% of the beam size [39]. Using the average energy may lead to some incorrect conclusions when the probability of outlying events is high [21]. The median is also used in IBICC to reduce sensitivity to outlying events such as those resulting from scattered ions [33]. OMDAQ also allows the investigation of specific regions of the energy spectrum, and was able to produce energy maps of these specific, corresponding regions.

The list mode file was converted to an energy spectrum through use of an excel spreadsheet which converted the raw data into column format. The energy spectrum was calibrated according to the 50 V bias result, with this peak having the best resolution out of all results and so the centroid position of the peak was deduced to be 5.5 MeV, the energy of the He^{+} beam used. Through previous measurements and calibrations of the beam using a Copper (Cu) grid, the beam width is measured to be 1.5 μm [33].

The main source of experimental error in the IBICC measurement setup at this facility is due to vibrations of the sample holder [34]. Uncertainty in the charge collection efficiency measured at each point in the raster scan of the ion beam is dependent on the statistics associated with each 2x2xmicron point. The uncertainty is a trade off between good statistics and radiation damage to the detector induced by the ion beam. While large statistics at each point are necessary to reduce the corresponding measurement uncertainty, radiation damage must be kept to a minimum. Typically there are several hundred to several thousand data point within a given energy window used to display the charge collection within a typical IBIC scan.

3.3.2 Ion Beam Induced Charge Collection Results

The results from the IBICC measurements are shown. With both channels biased the median maps for both the anode output and the guard ring output are displayed. The energy spectrum results for both these outputs are also shown. The charge collection colour bar scale shown below is relevant for both figures 3.6 and 3.9.

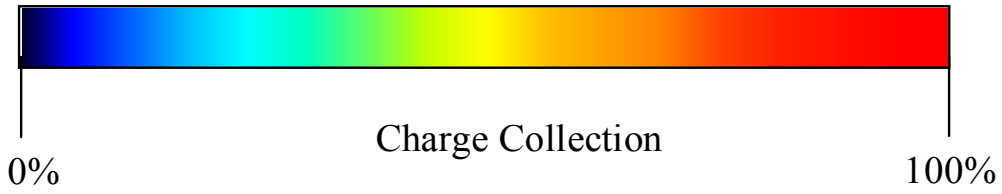

Figure 3.5: Charge Collection Colour Bar

3.3.2.1 Both Channels Reverse Biased

0 V

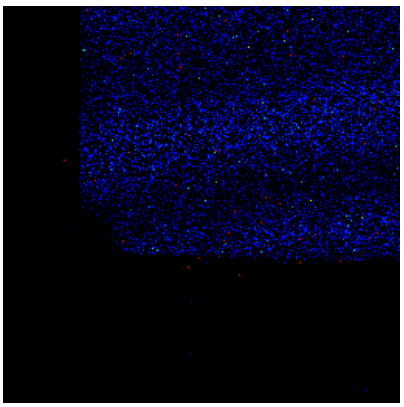

10 V

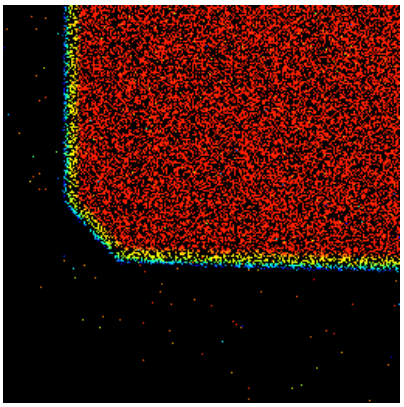

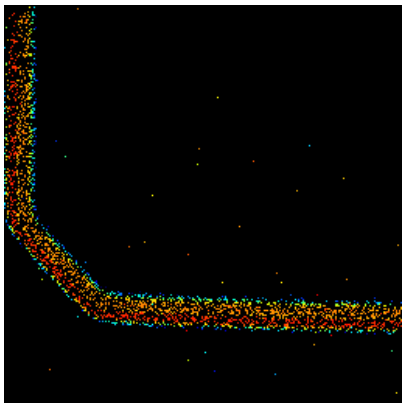

20 V

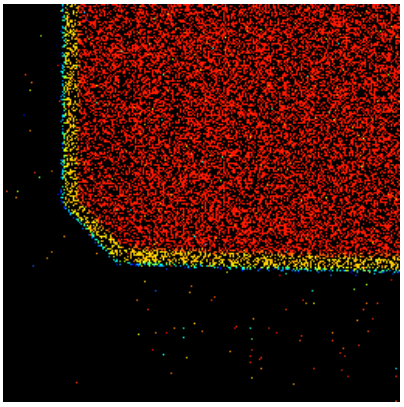

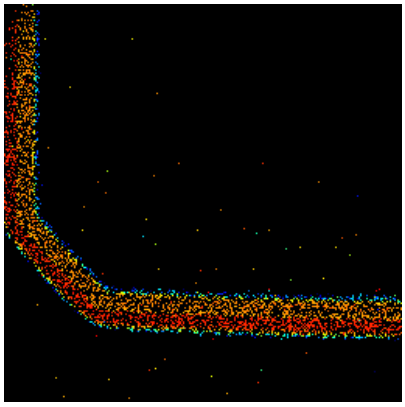

30 V

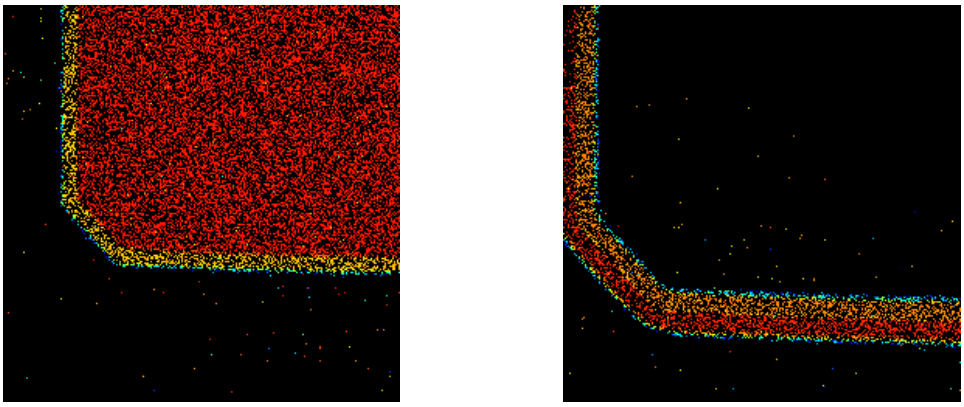

40 V

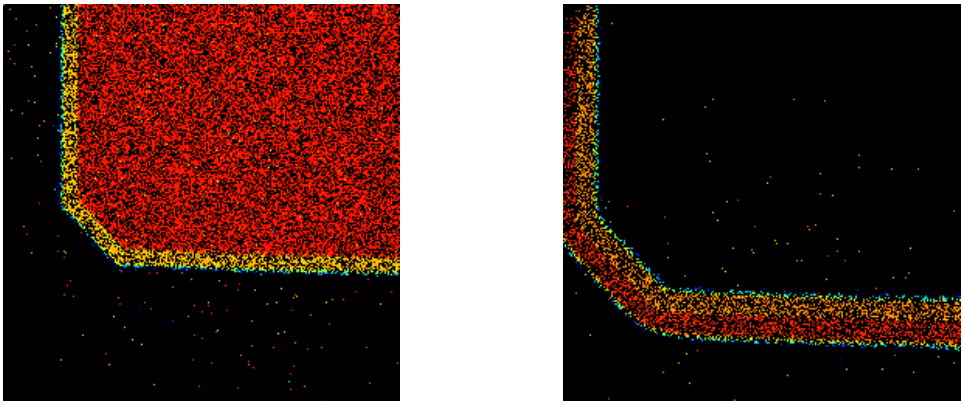

50 V

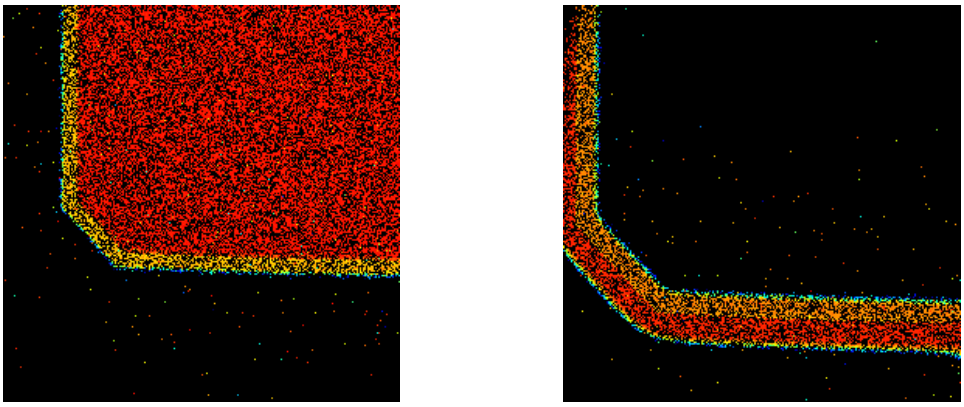

Figure 3.6: 0 V – 50 V Reverse Bias, Guard Ring Connected IBICC Results, Anode Output (Left), Guard Ring Output (Right)

The median energy maps are shown. Incomplete charge collection may be observed at 0 V bias. At 10 V and 20 V bias some incomplete charge collection may also be seen at the edges of the sensitive detector area, with a blue outline able to be observed around the sensitive detector area. It may also be seen that the guard rings work, though they have to be biased to the same voltage as the anode or a high leakage current is observed. To investigate changes between the higher bias voltages, the energy spectrum needs to be studied.

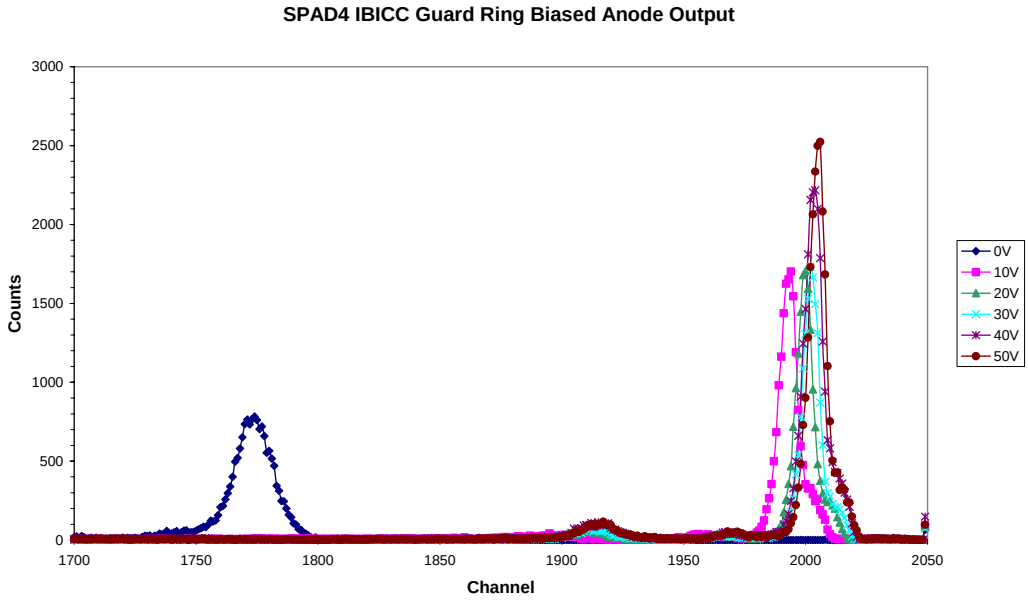

Figure 3.7: IBICC Results Anode Output with Guard Ring Biased Energy Spectrum

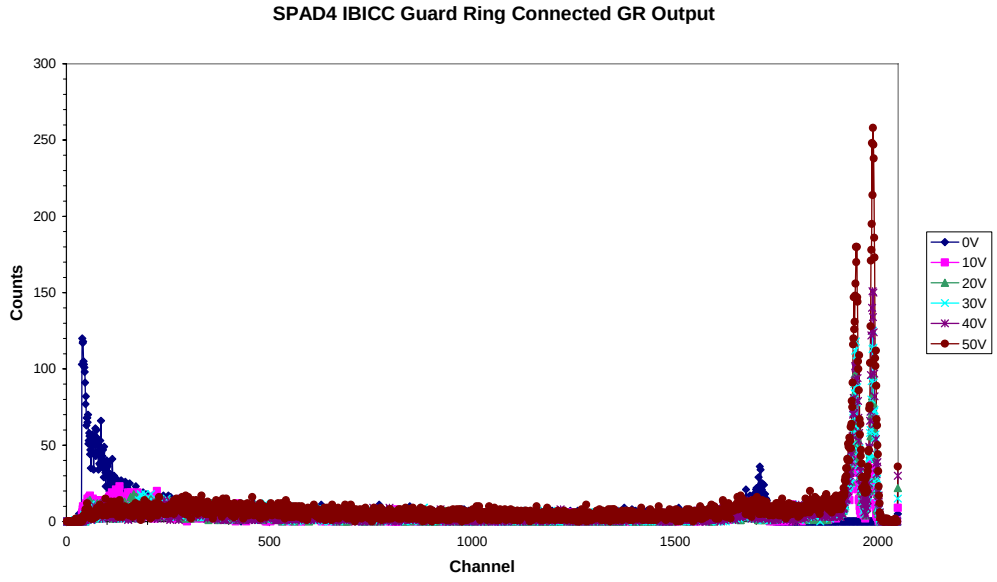

Figure 3.8: IBICC Results Guard Ring Output with Guard Ring Biased Energy Spectrum

The energy spectrum from the anode output indicates the difference in charge collection between the different bias voltages. The 10 V and 20 V bias energy peaks are at a slightly lower channel when compared to the 30 V, 40 V and 50 V bias energy peaks. Thus full charge collection is only just achieved with a bias of 30 V and higher. The 50 V bias result has the highest charge collection, having the most counts in its peak. There is also a high energy tail for biases of 10 V and greater. This may be due to contributions from the guard ring being biased as the high energy tail is not present when the guard ring is left floating, with these results displayed in figure 3.10.

The guard ring is shown to operate correctly when a bias voltage is applied, with charge carriers generated just outside of the depletion region of the photodiode and diffusing away being collected by this ring. This may be observed through the IBICC median energy maps, with ion strikes generating charge carriers within the depletion region being collected by the anode output, and charge carriers generated just outside this region being collected by the guard ring when biased.

3.3.2.2 Anode Channel Reverse Biased, Guard Ring Floating

0 V

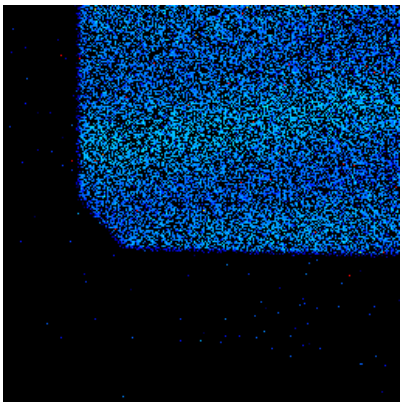

-10 V

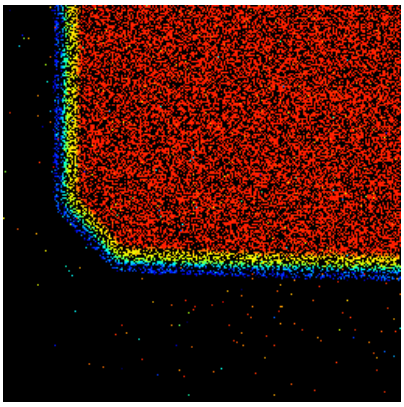

-20 V

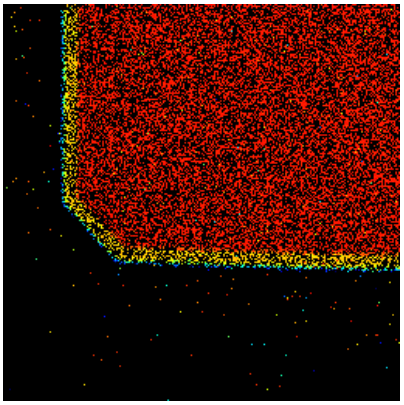

-30 V

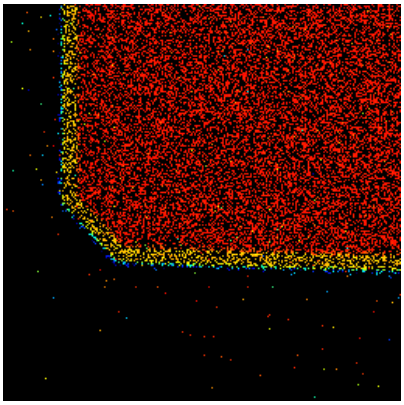

-40 V

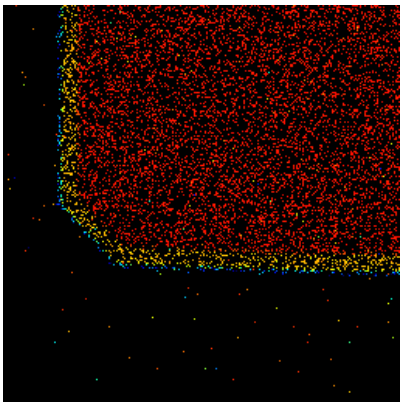

-50 V

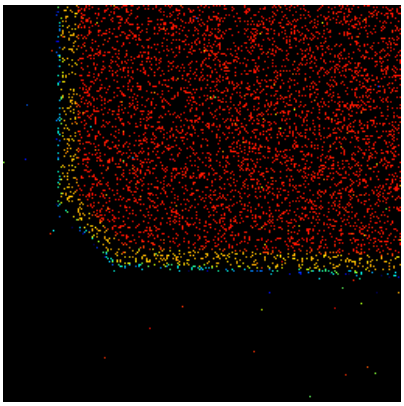

-60 V

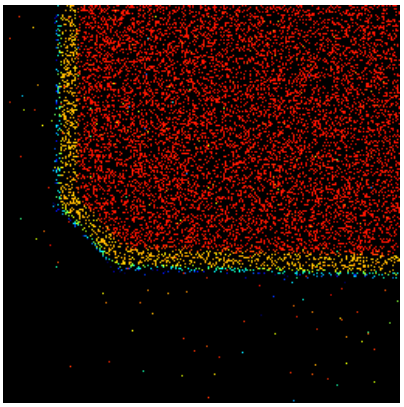

-80 V

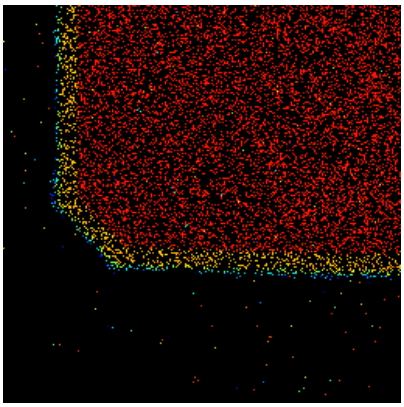

-100 V

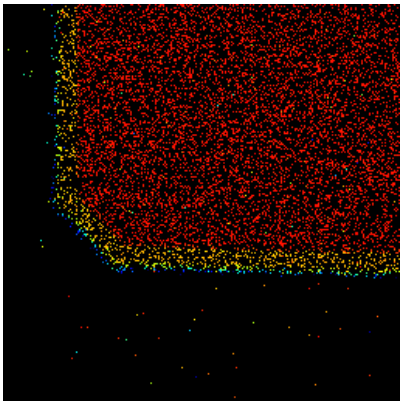

Figure 3.9: 0 V – 100 V Reverse Bias, Guard Ring Floating IBICC Results

The median energy maps for all the results with the guard ring floating are shown in the above figures. From these energy maps it may be seen that incomplete charge collection occurs at 0 V bias, and completely full charge collection does not occur until 40 V bias. From 40 V to 100 V bias the median maps are roughly identical, with very little difference between these voltages being able to be distinguished with the eye. For a more intensive investigation into the subtle differences between these voltages at which there is complete charge collection the energy spectrum for each of these bias voltages with the SPAD4 photodiode need to be considered.

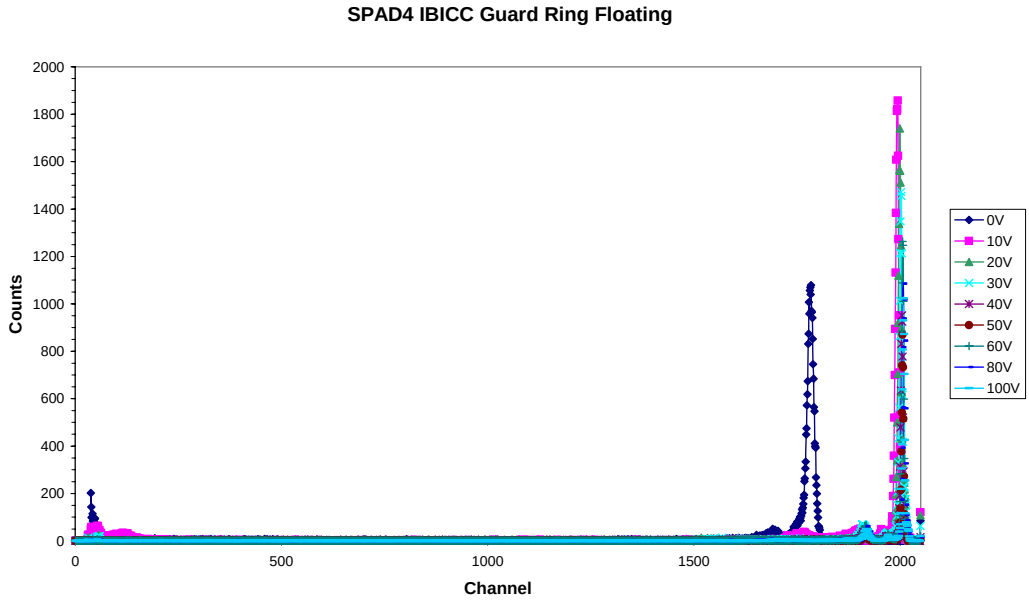

Figure 3.10: IBICC Results Anode Output with Guard Ring Floating Energy Spectrum

With 0 V bias over the SPAD4 photodiode, complete charge collection does not occur. As may be seen from the results the peak is at a much lower channel than the rest of the bias results. Before the main energy peak there are also small peaks at different channels. The OMDAQ software also allows the energy spectrum to be studied in relation to the location of the charge carriers which make up the part of the energy spectrum of interest. If the 50 V bias energy spectrum is studied closely, a small peak may be seen which centres at channel 1914. The energy map for the channels incorporating the peak is shown in figure 3.11. As seen from the figure, almost all the counts in the peak result from interactions with the photodiode guard ring.

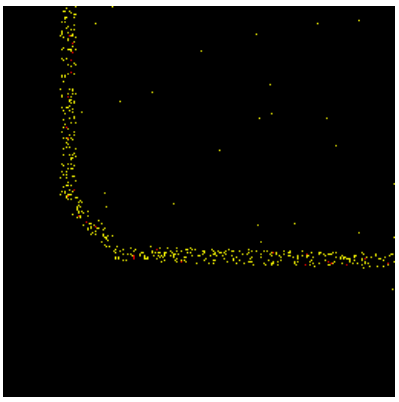

Figure 3.11 – Energy Map for 50 V Bias Guard Ring Floating Energy Spectrum Channel 1888 - 1940

To study the other bias voltages accurately the other results need to be viewed closely. The energy spectrum focussed on channels 1980 to 2020 is shown in figure 3.12.

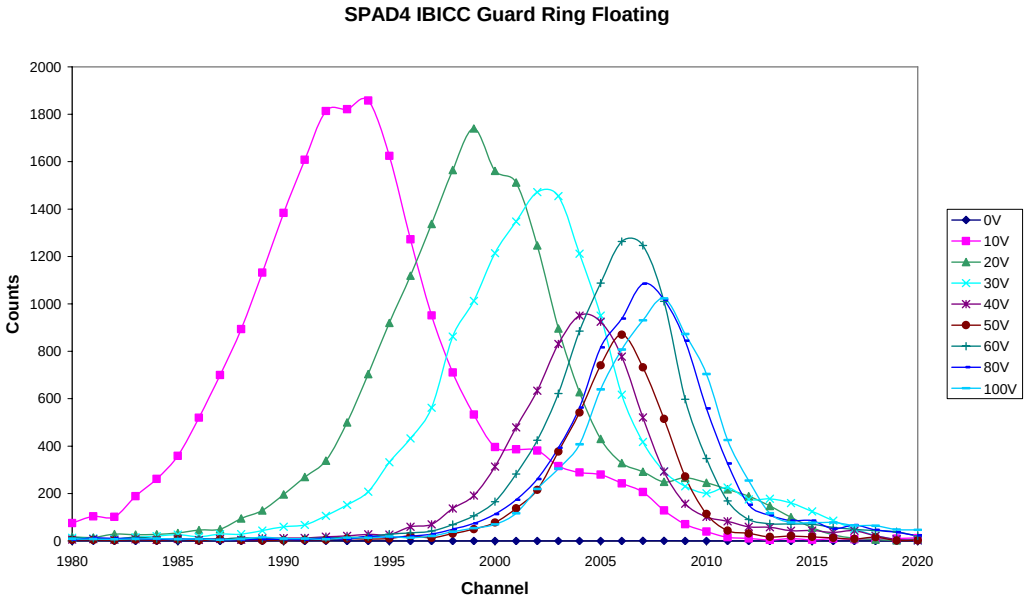

Figure 3.12: Channels 1970 – 2020, IBICC Results Anode Output with Guard Ring Floating Spectrum

From figure 3.12 it may be seen that though in this case the 50 V bias does not have the greatest charge collection, it has the best FWHM energy resolution when compared to the other results. Incomplete charge collection is again observed from the 10 V, 20 V and 30 V bias results, with their energy peaks being at a slightly lower channel when compared to the other peaks. At bias voltages higher than 50 V, the peaks move to slightly higher channels, but the FWHM energy resolution of the peaks increase. This is due to over depletion of the photodiode, which causes loss of energy resolution due to signal waveform deterioration and degradation.

Chapter 4 – LYSO Crystal Simulations and Measurements

4.1 Crystal Profile

Crystal profiles of each side of two different pieces of LYSO crystal were carried out using the DEKTAK 6M Surface Profiler. This profiler has a tip with a radius of 12.5 microns. The shape of the tip governs the shape of the walls for deep pits. These measurements were carried out by Dr Alexey Pan at the University of Wollongong. The results of these measurements were used to calculate the roughness of each side of the LYSO crystal. An average roughness was calculated and then was able to be incorporated into the simulations, in particular the scintillation program simulations. DETECT2000 has pre programmed surface finishes and thus the average roughness could not be incorporated.

Side	Crystal 1	Crystal 2
	Average Roughness (Angstroms)	Average Roughness (Angstroms)
1	0.017845	0.013981
2	0.006922	0.025728
3	0.023129	0.016300
4	0.008806	0.015773
5	0.010150	0.024951
6	0.007038	0.014366

Table 4.1: Average Roughness of each side of the profiled LYSO crystals

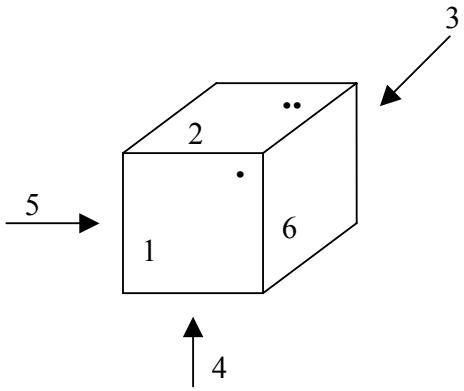

Figure 4.1: Crystal 1 Side Allocation

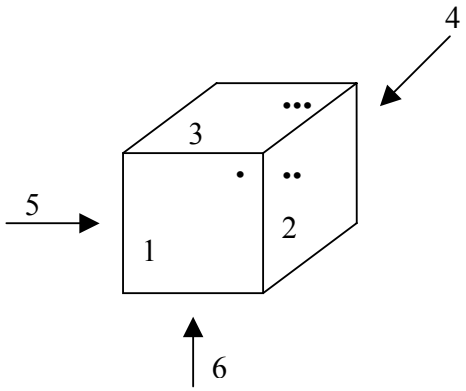

Figure 4.2: Crystal 2 Side Allocation

The crystal profiling results for each individual side are displayed in appendix 1. For crystal 1, from the calculated average roughness, and the surface profile results, it may be concluded that side 3 is the roughest surface. For crystal 2, from the calculated average roughness from the surface profile results, it may be concluded that side 2 is the roughest surface.

The simulation and physical measurement results will only be shown for crystal 2. Crystal 1 was concluded to be a "bad" crystal, and did not produce any results at all when energy spectrum measurements were undertaken. This is an intrinsic property, with crystal surface and roughness not being a factor for this. As can be seen from the crystal profiling results in appendix 1, both crystals are of a similar surface roughness. In every batch of LYSO crystals produced, there will always be some crystals which do not produce any light output, and thus are concluded to be bad. This may be due to the variation of the Ce-concentration in the crystals produced [40]. Unfortunately crystal 1 was one such crystal that was concluded to be bad.

4.2 Light Output Simulations

The light output simulations were conducted with two simulation programs, Scintillation Program written by Dr George Takacs and Dr Phil Simmonds, which was developed at the CMRP (University of Wollongong), and DETECT2000, which was released by Moisan, et al from Laval University in Quebec, Canada [41].

The simulations with both of the programs simulated the paths of 30000 optical photons generated within the scintillator after a gamma ray interaction in the crystal. The simulations are compared with one another using the same settings for the crystal – a crystal volume of 3x3x3 mm^3 and a LYSO refractive index of 1.81. Also, the optical grease refractive index was set to 1.62, and the reflectivity of the cladding was set to 0.93 for both programs. In both programs the measured photons are generated from the centre of the crystal.

Comparisons between the two programs are made with regards to crystal surface settings, and surface cladding configurations.

4.2.1 Scintillation Program Simulations

The Scintillation Program was created at the University of Wollongong and modified by Dr Phil Simmonds. This program was written using the FORTRAN language. The simulation code used for this program was originally written by Dr George Takacs for the Centre for Medical Radiation Physics at the University of Wollongong. [1]

This Monte Carlo (MC) code was developed to track the path of photons within a scintillator after excitation by a gamma ray. To simulate the propagation of scintillation light in the crystal, a specified number of photons are generated at a point in the crystal, with randomly chosen directions with uniform probability per unit solid angle. The point of intersection of the photon trajectory and scintillator surface is determined and the surface conditions are then used along with Fresnel laws for unpolarised light to determine the reflection probability and scattered direction. The simulation code does consider attenuation of photons within the crystal volume. However, due to the small average path lengths of the scintillation photons and large optical attenuation coefficients in the case of the crystals studied in this thesis, such attenuation was ignored. The crystal surface may be specified as being clad with a diffuse reflective material, specular reflector, and detectors or unclad. With diffuse reflection, Lambert's law has been assumed so that the probability for refection at an angle θ to the surface normal is independent of incident angle and proportional to $\sin 2\theta d\theta$. Each photon is followed until it exits the scintillator plus any cladding. If the photon exits on the photo detector surface, the count for the detector it enters is incremented. [1]

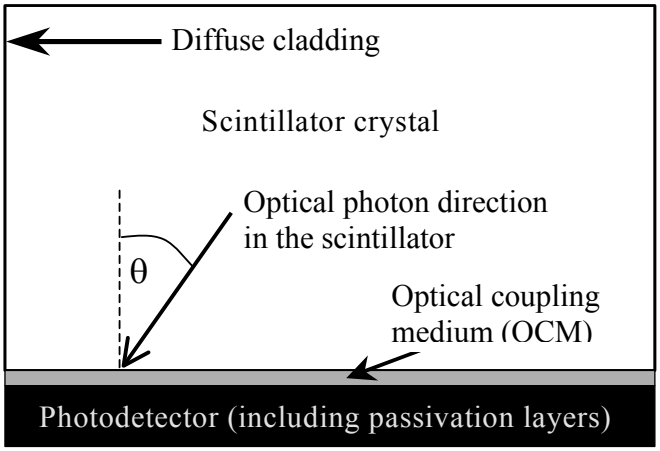

Figure 4.3: Schematic figure of the experimental layout model used in Scintillation Program

The Scintillation Program was extended by Dr Phil Simmonds to include the angular dependant reflectivity, 1 – T(θ) at the scintillator PD interface using look-up tables of separately calculated T(θ) values. Thus the resulting calculated distribution N(θ) represents the distribution of photons transmitted into the silicon PD through the coupling medium (grease or air) and over layers which make up the entrance window of the photodiode. This program treats the optical coupling layer of grease or air as an 'intermediate medium' representative of a film of uneven thickness [27].

The program was used to model the light output from the LYSO crystal into a SPAD4 detector under different conditions. These conditions included when the crystal was clad and unclad, when optical grease was applied between the crystal and the detector, and also when certain sides were clad and unclad. Also, the effect of roughening up the crystal surface was investigated, and the effects on the light output observed through the simulations. Further work was done investigating the use of the code with the SPAD3 and was published in [27].

The ScintX7 executable was used for these simulations. This version of the Scintillation program allowed the roughness of each crystal face to be set.

4.2.1.1 Scintillation Program Inputs

An example of a Scintillation Program input file may be found in appendix 2. Initially the input file specifies the random seed generator and the number of photons in one simulation. The crystal size is then defined, along with the six sides of the crystal. This allows the crystal surface to be set individually in both roughness, cladding (clad or unclad), and contact with the surface, whether it be with air, or with the detector. The z-min axis was set as the side of the crystal in contact with the detector. The input file also allows the reflectivity of diffuse cladding and the reflectivity of metallic cladding to be specified, along with the number of iterations and the scintillator crystal refractive index. A feature of the code is that it allows the specification of the angle to which the photon distribution will be non zero up to. The angular response of the detector was not investigated in the simulations for this thesis, though some were completed and were submitted in [27]. Lastly, the input file specifies the transmission file which is to be called by the program. The transmission file specifies the SPAD4 photodiode to be used, along with the configuration, such as optical grease or air bonding the crystal to photodiode, and the peak wavelength of emission to the detector. The transmission files used, along with their various configurations are shown in table 4.2. Generally the files are named according to the SPAD photodiode they are created for (S), the optical grease refractive index used (G) and the peak wavelength (L). S4G6L42.txt is the transmission file used in the comparison with the DETECT2000 simulations, as it best matches the parameters used in those simulations. This file is specifically used for SPAD4 simulations, and has an optical grease refractive index of 1.62, and a peak wavelength of 420 nm.

Transmission File	Peak Wavelength (nm)	Optical Grease Refractive Index
S4G6L42.txt.	420	1.62
S4G5L42.txt	420	1.53
S4G5L46.txt	460	1.53

Table 4.2 – Scintillation Program SPAD4 Transmission Files Configurations

Simulations were set up under different conditions in an investigation into the best conditions for light collection from the LYSO crystals using the SPAD photodiodes, in particular the SPAD4 photodiodes. Simulations were run with the crystal completely clad, completely unclad, with only the surface opposite the detector surface clad, with only the sides of the crystal clad and the top surface unclad and also with the crystal completely clad except for side 2, which is unclad and roughened.

4.2.1.2 Scintillation Program Simulation Results

Simulations were completed using the three different transmission files outlined in table 4.2. These were the only SPAD4 photodiode transmission files which have been created for the scintillation program thus far. Physically, energy peaks are not resolved with an unclad crystal with no grease medium between crystal and detector. However a clad crystal with an air gap can produce results. This was unfortunately not able to be simulated and compared, as a transmission file with an air gap had not been created for the SPAD4 yet at the time of writing. However, the results for all sets of simulations were quite similar in pattern, with the same variations and trends in both.

Simulations were completed with the 3x3x3 mm LYSO crystal fully clad, the crystal fully unclad, with only the top surface (z-max axis) of the crystal clad, and with only the sides (x-min, x-max and y-min, y-max) clad. The last simulation has the second side unclad with the rest of the crystal faces clad. In all these simulations the crystal face in contact with the detector was modelled as being coupled using optical grease.

	S4G5L42	**S4G5L46**	**S4G6L420**
Description	**% photons**	**% photons**	**%photons**
Clad	50.97	51.75	58.95
Top Clad	47.58	47.74	51.66
Sides Clad	40.73	41.43	49.64
Unclad	37.78	38.49	41.98
Side 2 Unclad, Others Clad	49.11	49.53	55.39

Table 4.3: Comparison of the LYSO states without roughing with Scintillation Program

As can be seen from table 4.3, a clad crystal with grease produces the best results. With all transmission files, the difference between a clad and unclad crystal is in excess of 23%.

The roughness was also varied on side 2 of the crystal, which was modelled as one of the four sides of the crystal, with this side neither the side in contact with the detector or directly opposite this side. This was roughened from 0.1 to 1.0 under different crystal conditions, including clad, unclad and with side 2 unclad only. Only the results using the transmission file S4G6L420.txt will be shown, as it best matches the parameters used in the DETECT2000 simulations. However all transmission files produced the same trends.

	CLAD	**UNCLAD**	**SIDE 2 UNCLAD**
Roughness	**%photons**	**%photons**	**%photons**
0.1	62.84	40.57	54.99
0.2	65.71	38.85	55.38
0.3	67.85	37.75	55.92
0.4	70.29	37.40	56.10
0.5	70.77	36.67	57.08
0.6	72.37	36.64	57.55
0.7	72.75	37.20	57.25
0.8	73.73	36.85	57.87
0.9	74.73	36.94	58.49
1	74.93	36.78	57.89

Table 4.4: Varying Side 2 Roughness under different crystal conditions using Scintillation Program

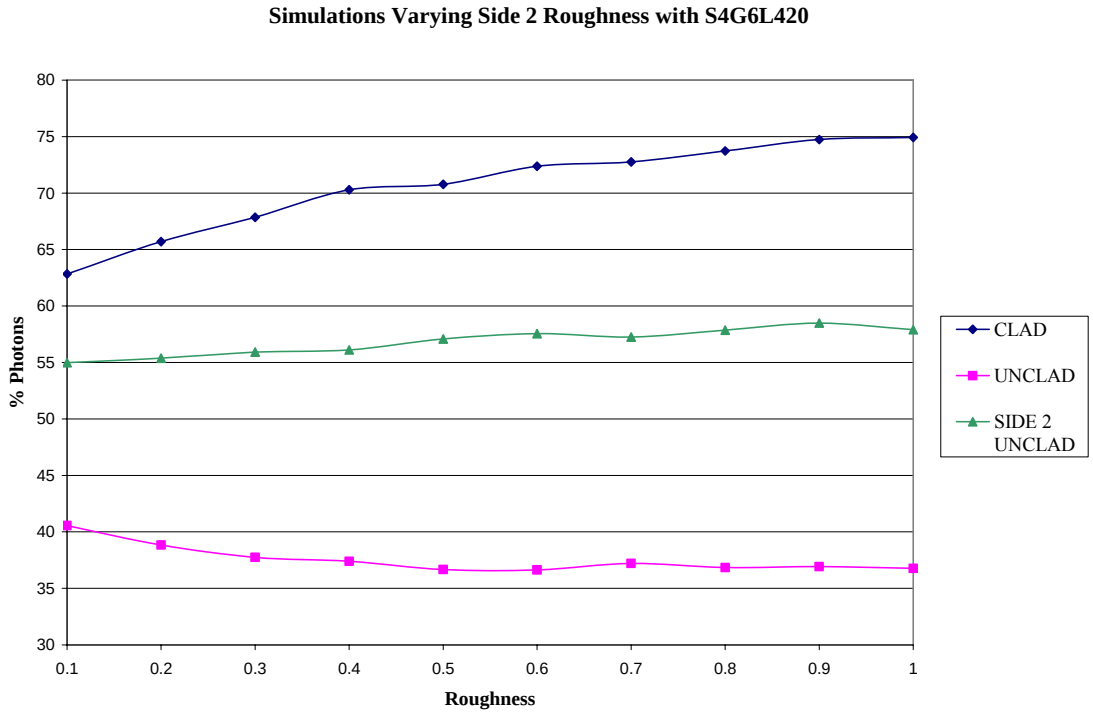

Figure 4.4: Clad, Unclad and Side 2 Unclad Roughness Simulations using Scintillation Program

As may be seen from table 4.4 and figure 4.4, increasing the roughness of the side with cladding increases the number of photons which reach the detector. There is an increase of approximately 16% when one crystal surface is roughened to a unit of 1 as compared to what it is originally when fully clad and not roughened. With the crystal unclad, increasing the roughness slightly decreases the output slightly, with a difference of 5.2%. In the simulations with only side 2 unclad there is only a small increase in output, with a difference of 2.5% when compared with the original result.

4.2.2 DETECT2000 Program Simulations

DETECT2000 is the object orientated C++ version of DETECT and is a program for modelling the optical properties of scintillators. DETECT is a Monte Carlo model of the behaviour of optical systems with a special emphasis on scintillation detectors. The program generates individual scintillation photons in specified portions of the scintillator, follows each photon as it passes through the various components and interactions with surfaces, allows for possible absorption and re-emission by a wave shifting component and records the fate (absorption, escape or detection) of each.

DETECT2000 uses initial definition statements to specify the optical properties of all materials and surface finishes used in the system. Components may then be built from these defined materials, finishes and objects, such as the different layers of photodiodes and crystals. The optical behaviour of each surface is defined by selecting from a set of previously defined surface finishes, with surfaces able to be external (assumed to be an interface with a vacuum) or shared with another component. Photons are isotropically generated within a defined material and volume. Photons are tracked individually until they are absorbed, detected or have escaped from the system. With each photon reflection or scattering, the program logic determines the new direction of the photons, identifies the component in which it is travelling and computes the next intersection with a surface. A random sampling is made to determine if the photon is bulk absorbed, scattered or wavelength shifted over this path, and if none of these occur the optical properties of the next surface determined whether the photon is reflected, refracted, detected or absorbed. This process is then repeated for all subsequent paths and photons. [41]

4.2.2.1 DETECT2000 Input File

The DETECT2000 input file, that is the file which contains all the material, finish and geometry definitions, output options and program control commands, can be produced either by hand or by the packaged program in the Detect Suite, BUILDER [41]. In this case the file was written by hand. An example of a DETECT2000 input file used is shown in appendix 2.

Initially program controls are set. This may point the program to any files which it needs to call upon during its operation. This may include wavelength information and quantum efficiency data. Following this the different materials need to be defined. This includes information such as the refractive index, crystal decay time, absorption and scattering coefficients of the crystal. Then the different types of finishes are defined, with finishes such as paint, polish, and ground or detect used. A detect surface merely counts the number of incident photons which reach it. A direct comparison with the scintillation program in regards to varying the surface roughness parameter cannot be made, as DETECT2000 has preset surface settings. The surface is able to be configured to a range of settings, with a smooth unclad surface being the "POLISH" surface configured for the program. The "PAINT" surface setting was used for a clad surface and a rough surface was set as "GROUND". Next the different planes are defined before each component is defined. In this case each layer of the SPAD4 photodiode was modelled, along with the optical grease layer between the crystal and the photodiode. Lastly, how long each photon is tracked for and the plane in which optical photons will be generated are specified, along with the number of photons to be simulated. The optical photons were generated from both the centre of the crystal and over the entire volume of the crystal.

Simulations were completed with DETECT2000 using different absorption and scattering parameters for LYSO crystal. As no information was found on the use of DETECT2000 with LYSO in literature, the factors for the absorption density and scattering density were acquired from [42]. From [42], the total attenuation length, λ_{total}, for LYSO may be found. The total attenuation length is published for both LYSO with a polished finish and LYSO which has been wrapped with Teflon cladding. A value of 42.0 cm is given for LYSO polished, and 20.0 cm for LYSO Teflon wrapped. From these values, the absorption density and the scattering density can be calculated from the following formula which is published in [43]:

$$\frac{1}{\lambda_{Total}} = \frac{1}{\lambda_{Scat}} + \frac{1}{\lambda_{Abs}} \quad \ldots (1)$$

In the formula, λ is the mean free path in millimetres of the light photons in the bulk material.

For these simulations, the absorption density (AD) and scattering density (SD) were assumed to be equal for simplicity. Thus for a total attenuation length of 42.0 cm, or 420 mm, absorption and scattering densities of the value of 840mm were calculated. For a total attenuation length of 20.0 cm, or 200 mm, absorption and scattering densities of the value of 400 mm were calculated.

4.2.2.2 DETECT2000 Simulation Results

The results for the different absorption and scattering densities due to the different values for the total attenuation length are shown in table 4.5.

	Volume	**Centre**		**Volume**	**Centre**		**Volume**	**Centre**
AD,SD	**400**	**400**		**840**	**840**		**Average**	**Average**
Clad	55.62%	57.32%		56.60%	58.51%		56.11%	57.92%
Unclad	35.00%	34.58%		35.45%	35.79%		35.23%	35.18%
Side 2 Unclad	45.34%	46.26%		46.22%	46.83%		45.78%	46.54%
Side 2 Unclad, Rough	46.69%	48.86%		47.43%	49.60%		47.06%	49.23%
Unclad, Rough	27.18%	29.12%		27.48%	29.34%		27.33%	29.23%

Table 4.5: DETECT2000 Simulations Light Output Results

As may be seen from table 4.5, the highest output was obtained with the crystal fully clad. Also, from the results it can be seen that It appears that roughening the surface only produces a small increase in light output, when a comparison between the results of side 2 unclad and side 2 unclad and rough are considered. The practical impact of this can not be determined from the simulations completed. This was determined from the physical measurements (section 4.3).

4.2.3 Comparison between Simulation Results

In making a direct comparison between the results obtained by the "Scintillation Program" and "DETECT2000", identical parameters and settings must be used. The optical grease parameter n was set to 1.62 in DETECT2000, and the only transmission file this corresponds to for the Scintillation Program is "S4G6L420".

	Scintillation Program	**DETECT2000**
Clad	58.95%	57.92%
Unclad	41.98%	35.18%
Side 2 Unclad	55.39%	46.54%
Side 2 Unclad, Rough	57.89%	49.23%
Unclad, Rough	36.78%	29.23%

Table 4.6 Comparison between Scintillation Program and DETECT2000 of Results

From the simulation results in table 4.6, it may be observed that both programs follow the same trends in regards to crystal surface treatment and photon detection. The fully clad crystal simulation produces the best result, with approximately 1% difference between the two programs. However the unclad crystal produces approximately a 7% difference, with Scintillation Program simulating a result much greater than the DETECT2000 result. With both simulation programs this crystal finish produces the worse light output, before roughening. With both simulation programs, having a side unclad and then roughening it produces an improvement of approximately 2.5%, with this increase being similar for both programs. This however is only a slight increase in the light output, though Scintillation Program again produces a higher result than DETECT2000, though this time the difference between the two programs is approximately 8.5%.

DETECT2000 has been tested extensively, as may be seen in literature. Scintillation Program was created in house at the CMRP. The Scintillation Program input file can be modified so as to be specifically for LYSO crystal and the SPAD4 photodiodes, whereas DETECT2000 requires parameters for both the photodiode and LYSO crystal to be specified. There are some significant differences in results between the two programs,

with possibilities from these resulting from photons being surface absorbed, that is absorbed in the surface of the crystal or the cladding material, according to DETECT2000, with Scintillation Program not having a parameter for this, and thus may produce the greater result. Also, Scintillation Program does not consider the attenuation length or scattering length of photons within the crystal, which DETECT2000 does. This may also contribute to the difference in results between the two programs, though the difference should be insignificant due to the size of the crystals and the attenuation and scattering length parameters used. Generally, error in Monte Carlo simulations is of the order of less than 0.3% [44]. This error is determined through simulating different random seed numbers at a given interaction point and also running the simulating using a given seed number in a number of interaction positions within the scintillator crystal and determining the differences. Any further investigation into errors, associated for example with crystal imperfections, mechanical defects, etc, was beyond the scope of this thesis.

4.3 Crystal Measurements

4.3.1 Crystal Measurements Method

Measurements were taken using the same piece of LYSO crystal as originally measured to verify simulation results. LYSO crystal 2 was used as crystal 1 was concluded to be a bad crystal, producing no results at all when coupled to a photodiode. This is outlined in section 4.1. Thus all crystal measurements shown have been completed with crystal 2. The measurements were taken with the crystal mounted on a SPAD4 photodiode. The crystal was mounted with optical grease and with and without cladding, the same states at which the crystal was modelled in the simulations conducted. Measurements were also taken without optical grease, but no peak was able to be distinguished when the crystal was unclad, which was expected. With a good, clad crystal, a peak could be seen, though with a lower channel position number, and thus decreased light output.

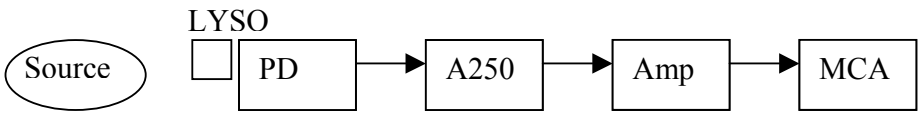

Figure 4.5: LYSO Crystal Measurement Equipment Setup

From the crystal measurement setup in figure 4.5, the signal from the SPAD4 photodiode, which is reversed biased at 50 V, goes through to the Amptek A-250 charge sensitive pre amplifier, before proceeding onto the Canberra 2020 Spectroscopy Amplifier where a shaping time of 0.5 μs and a gain of 3000 is applied to the signal. The signal is then recorded by the MCA which is connected to a PC.

Measurements were taken using I-125, Na-22 and Cs-137 radioisotopes. Different SPAD4 photodiodes were used in these measurements, along with 2 different crystals. SPAD4 #7 was used initially to make the measurements, with this being also the PD used in the coincidence timing measurements. Unfortunately this SPAD4 was damaged during one of the experiments, and so other SPAD4 detectors were used to complete the measurements. For crystal 2, measurements were completed using either the SPAD4 #1 or SPAD4 #6 photodiodes. Two crystals were also used, with one being the one which was profiled and roughened. The other crystal was the LYSO crystal which was also used in the coincidence timing resolution measurements. This reference crystal was already clad.

The I-125 measurements were taken with each SPAD4 with no crystal coupled. The SPAD4 photodiodes were reversed biased to 50 V, and the spectroscopy amplifier was set to a gain of 3000 and a shaping time of 0.5 μs. The MCA was set to 10 V ADC and 1024 channels. These measurements, along with the knowledge that the band gap energy for silicon is 3.62 eV, or 3.62 eV per electron/hole pair [45] allowed calculation of the electron/hole pairs produced per channel. For example, the 27 keV peak produces approximately 7500 electron/hole pairs for photons absorbed in the photodiode depletion layer [46]. This, along with the measurements with the reference crystal with each SPAD4 photodiode allows for comparison between the two detectors used.

The two prominent peaks in the I-125 spectrum are the 21 keV and the 27 keV peaks. Through a comparison between the positions of these peaks, the electron/hole pairs produced per channel can be found. This is done using the following formula:

$$e^{-}/\,hole\ pairs\ produced/Channel = \frac{\left(\frac{27000}{3.62} - \frac{21000}{3.62}\right)}{\left(27\,keV\ Peak\ Position - 21\,keV\ Peak\ Position\right)}$$

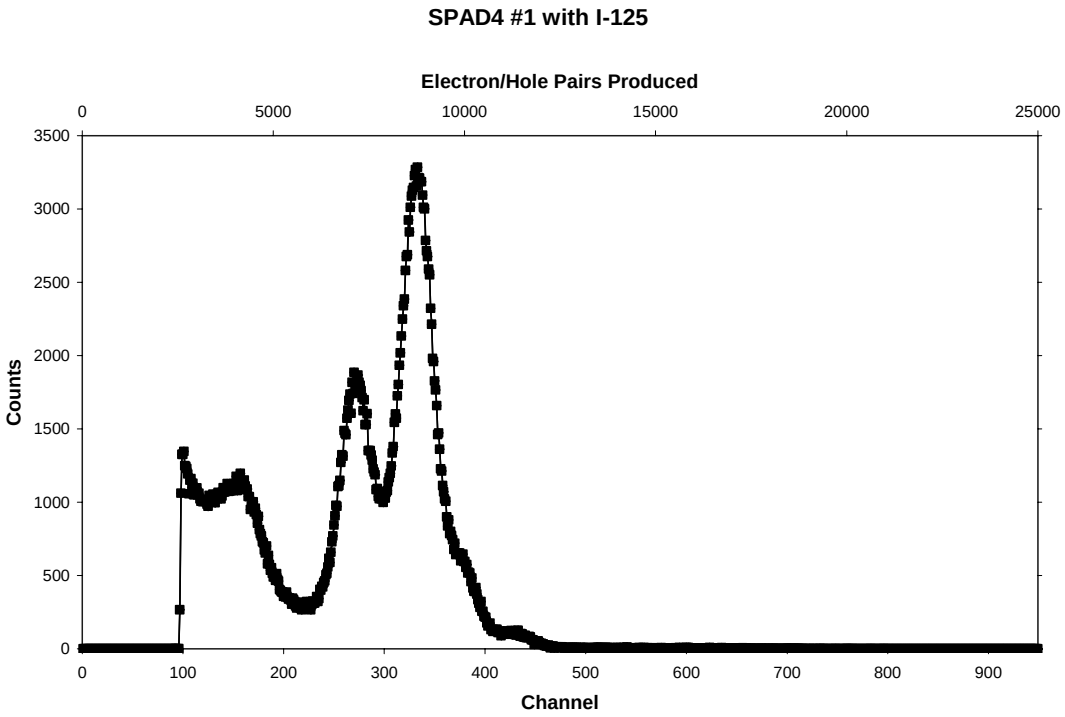

Figure 4.6: I-125 Spectrum with SPAD4 #1

From figure 4.6, the 21 keV peak was centred at channel 268.78 and the 27 keV peak was centred at channel 331.68. Thus this produced a result of 26.35 electron/hole pairs produced per channel.

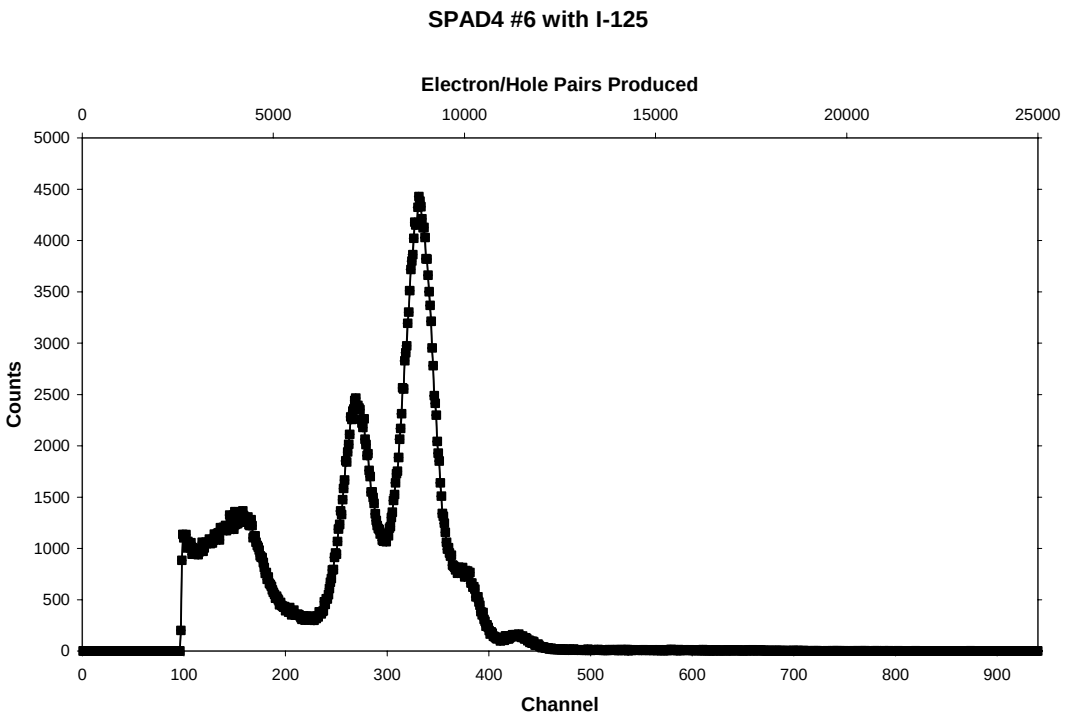

Figure 4.7: I-125 Spectrum with SPAD4 #6

From figure 4.7, the 21 keV peak is centred at channel 267.58 and the 27 keV peak is centred at channel 329.84. Thus this produces 26.62 electron/hole pairs produced per channel for this photodiode.

As the reference crystal will be used to compare the spectra obtained with the different SPAD4 photodiodes, the average electron/hole pairs produced per channel was used. Due to this, 26.49 electron/hole pairs produced per channel was used with all the spectra obtained.

Measurements were taken with the same crystal configurations as was used in the simulations. On the physical crystal, and from the reference system applied to the crystal sides in figure 4.2, side 5 corresponds to side 2 in the simulations. A measurement was also taken with the crystal reclad after roughening.

4.3.2 Crystal Measurements Results

Physical measurements were taken to compare with the simulation results. The resultant peaks are scaled to 1, and for each photodiode used the spectrum obtained with the reference LYSO crystal is also shown. This allows comparison between the results for each photodiode.

The reference LYSO crystal was used to allow comparison between the results from different SPAD4 photodiodes. As two SPAD4 photodiodes were used (#1 and #6), a reference crystal was used to account for any slight discrepancies between the photodiodes. Collection efficiency was able to be countered utilising the reference crystal so that a valid comparison of the measurements using the LYSO crystal could be carried out. These measurements were completed with the reference crystal fully clad and coupled to the relevant SPAD4 photodiode with optical grease.

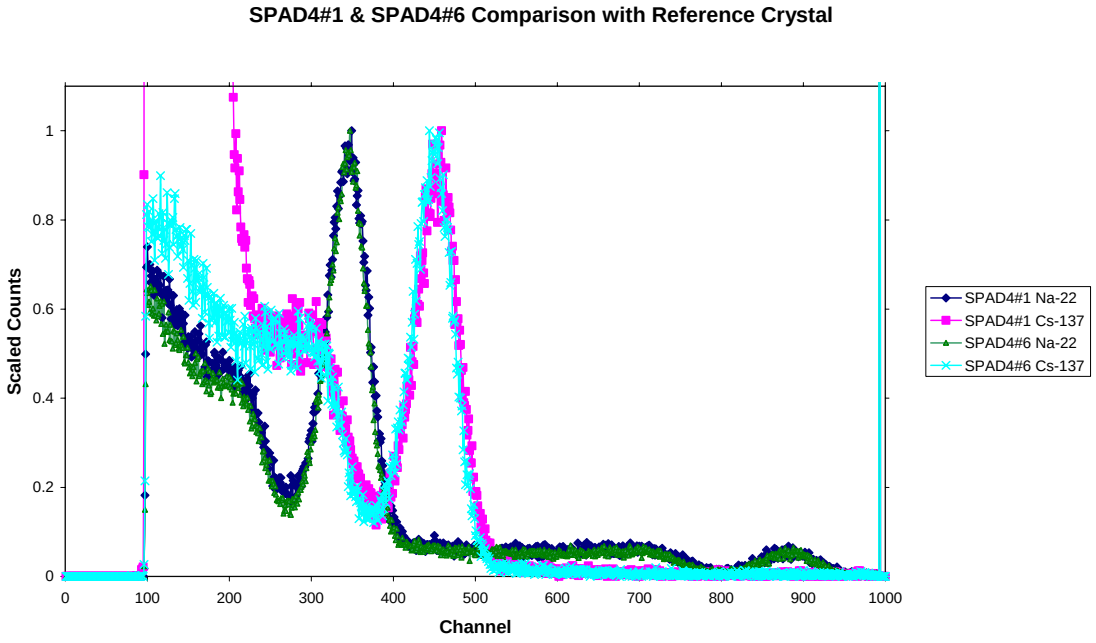

Figure 4.8: Comparison of SPAD4 Reference Crystal Measurements

Description	Centroid Channel	FWHM (Channel)	keV/Chan	511 keV Peak Energy Resolution (%)
SPAD4 #1 Cs-137	451.55	53.99	1.39	
SPAD4 #1 Na-22	342.92	52.32		14.23
SPAD4 #6 Cs-137	446.84	50.62	1.45	
SPAD4 #6 Na-22	342.42	49.58		14.03

Table 4.7: Comparison of SPAD4 Reference Crystal Measurements

From the reference crystal measurements with the two SPAD4 photodiodes, it may be concluded that they are quite similar in output. Their 511 keV energy resolution values were 14.23% and 14.03% for the SPAD4 #1 and the SPAD4 #6 respectively, a difference of 0.2%. However there is a small difference in peak position for both the 511 keV peak from the Na-22 spectra and for the 662 keV peak from the Cs-137 spectra which was not considered relevant.

The number of electron/hole pairs produced per channel was multiplied by the number of channels to calculate the number of electron/hole pairs detected for each peak position. With greater optical light output and better detection, more electron/hole pairs will be produced and the greater the peak position.

The results for the LYSO crystal measurements with Na-22 are shown in table 4.8 and figure 4.9. A description of the crystal surface condition, the SPAD4 used, and the centroid position along with the number of electron/hole pairs collected at the centroid of the 511 keV annihilation peak is shown. The number of electron/hole pairs was calculated by multiplying the centroid channel number by the number of electron/hole pairs produced per channel which was calculated from the I-125 spectra.

Surface	Coupling Medium	SPAD4	Centroid Channel	Electron/Hole pairs Produced
Fully Clad	Air	#1	170.50	4515.88
Fully Clad	Grease	#1	322.13	8531.98
Clad with Side 5 Unclad	Grease	#1	256.03	6781.24
Clad with Side 5 Unclad and Rough	Grease	#6	243.31	6444.34
Fully Clad with Side 5 Rough	Grease	#6	312.42	8274.80

Table 4.8: Na-22 Measurements Results

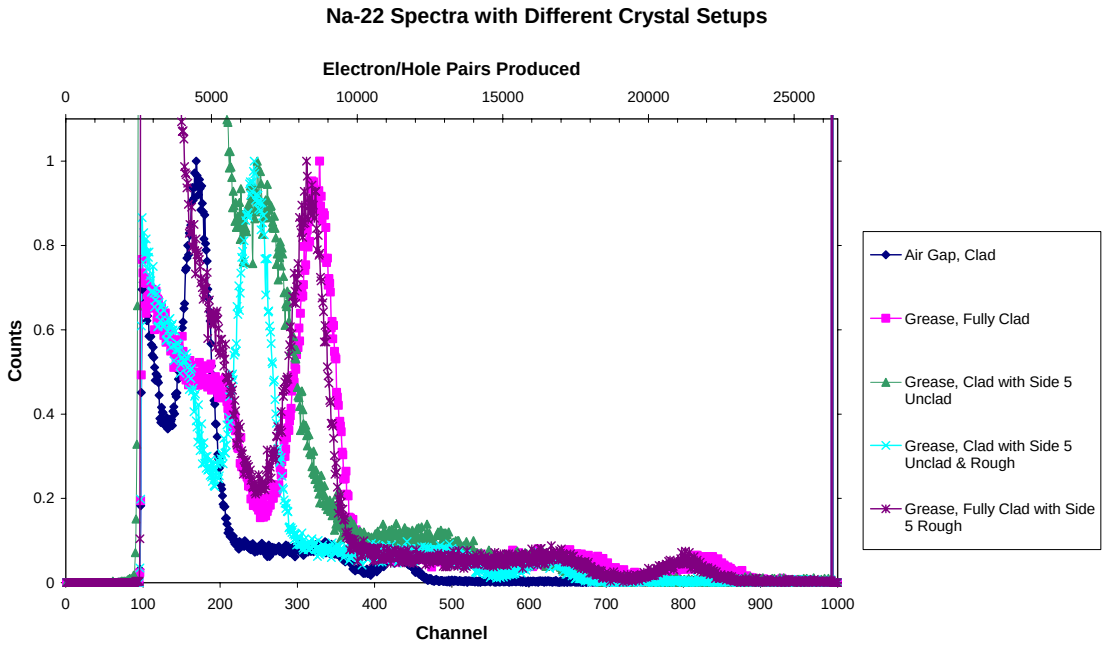

Figure 4.9: Na-22 Spectrum Measurements Results

The last measurements made with the SPAD4 #1 was for the grease, Clad with Side 5 Unclad set up. This measurement, with both Na-22 and Cs-137 has a lot of noise in the spectra, with a peak only just able to be distinguished above the noise. This is due to the degradation of the over layers of the SPAD4 photodiode, with this photodiode no longer operational after these measurements.

The results for the Cs-137 measurements are shown in table 4.9 and figure 4.10. The original centroid position, along with the number of electron/hole pairs produced at the centroid of the 662 keV energy peak is shown. The number of electron/hole pairs produced was calculated by multiplying the corrected centroid channel number by the number of electron/hole pairs produced per channel which was calculated from the I-125 spectra.

Surface	Coupling Medium	SPAD4	Centroid Channel	Electron/Hole Pairs Produced
Fully Clad	Air	#1	223.88	5929.71
Fully Clad	Grease	#1	421.29	11158.34
Clad with Side 5 Unclad	Grease	#1	320.10	8478.21
Clad with Side 5 Unclad and Rough	Grease	#6	318.34	8431.59
Fully Clad with Side 5 Rough	Grease	#6	408.28	10813.76

Table 4.9: Cs-137 Measurements Results

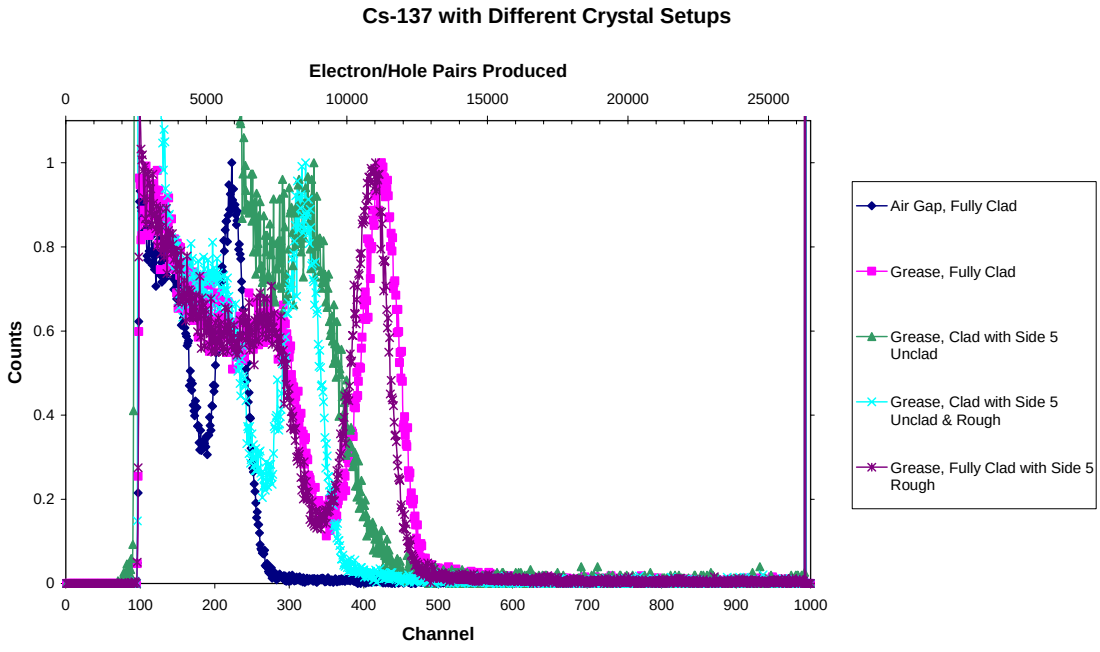

Figure 4.10: Cs-137 Spectrum Measurements Results

4.3.3 LYSO Crystal Measurements Comparison

The crystal measurements do not provide any conclusive evidence as to the effect of roughening of the crystal surface on the light output. The effect of roughening produces a slight decrease in light output with both the Na-22 and Cs-137 measurements. These differences in light output in both the Na-22 and Cs-137 measurements with the roughened crystal are insignificant when the FWHM of these peaks are considered. From figures 4.9 and 4.10, the differences between the results of the crystal with side 5 unclad, and of the crystal with side 5 unclad and roughened and unable to be distinguished, with both peaks appearing almost at the same position. The FWHM of all the energy peaks, for both Na-22 and Cs-137 measurements, range from 34 channels for measurements with an air gap, to 51 channels for Cs-137 measured with a fully clad crystal with one side roughened. The differences in centroid position between the smooth and roughened results were approximately 2 channels for Cs-137 and 13 channels for Na-22. These differences, when compared to the FWHM for the resultant peaks, are insignificant as the increase in light output, or decrease in light output, is unable to be resolved completely and accurately.

The fully clad crystal coupled with optical grease produced the greatest light output in both Cs-137 and Na-22 measurements. The reclad, roughened crystal produced a slightly reduced light output in both measurements when compared to the smooth, fully clad crystal, generating just under 250 more electron/hole pairs in each case. This correlates to approximately 10 channels of difference between the fully clad and the roughened, clad crystal, which when compared to the FWHM is insignificant. This result is the opposite of that which is suggested by Scintillation Program, with the results for roughened, clad crystal shown in figure 4.4.

The effect of using optical grease however can be seen from the results, with a significant increase in light output due to this. The reduction in light output may also be seen with the unclading of a single side, with this producing a significant decrease in light output from the crystal. An unclad crystal did not produce any results, with no peak able to be distinguished above the noise.

4.4 LYSO Crystal Simulations and Measurements Discussion

The LYSO crystal simulations concluded that the best configuration was a fully clad and greased crystal coupled to the SPAD4 photodiode. The measured experimental data also show this.

The effect of using grease to couple the LYSO crystal to the photodiode is quite significant. Though this was not simulated, a physical measurement was made. It could be seen that with grease, the electron/hole pair output which was detected by the photodiode approximately doubled, when compared.

The simulations completed and the measurements can be compared. This is done by comparing the number of electron/hole pairs produced in the crystal measurements and the percentage of photons detected in the Scintillation Program and DETECT2000. Converting the number of electron/hole pairs produced in the crystal measurements to a Scintillator Light Collection Efficiency (SLICE), which is equivalent to the photon detection efficiency for solid state X-ray detectors, or the results from the Scintillation Program and Detect2000 [27, 47]. The SLICE percentage was calculated using the 511 keV photopeak position in the Na-22 spectrum, and the assumption that 13,300 scintillation photons are emitted per 511 keV event in the LYSO scintillator crystals used in the measurements [27]. Both the measured results (SLICE) and simulated results displayed in table 4.10 are a comparison between detected photons and total photons produced in the crystal with a gamma ray interaction.

Surface	SLICE (Measured)	Scint Prog	DETECT2000
Fully Clad	64.15%	58.95%	57.92%
Clad with Side 5 Unclad	50.99%	55.39%	46.54%
Clad with Side 5 Unclad and Rough	48.45%	57.89%	49.23%
Fully Clad with Side 5 Rough	62.22%	74.93%	

Table 4.10: Comparison Between Simulations and Measured Results

The crystal measurements generally did follow the same trends in light output as shown by the simulations completed by the Scintillation Program and DETECT2000 but disagree with the results with roughening, as may be seen in table 4.10. The configuration with the greatest light output is the fully clad crystal coupled to the SPAD4 with optical grease, having a SLICE percentage of 64.15%. This was approximately 5% and 6% higher than the Scintillation Program and DETECT2000 results respectively. Having a side unclad reduced the results when compared to a fully clad crystal, and roughening reduced the light output result slightly for both Cs-137 and Na-22. This result disagrees with the simulation results, though simulation results indicated that an increase of approximately 2.5% would be achieved, and the measured result indicated a decrease of approximately 2.5% for the Na-22 when the SLICE percentage is compared to the simulation results. An unclad crystal measurement was unable to be completed as no peak was distinguished above the noise. Thus the unclad crystal simulation results were unable to be compared to the physical measurements; though being unable to obtain a photo peak produces the inference that an unclad crystal has a far greater reduced light output compared to a clad crystal, and follows the simulation results. Experimental error in the crystal measurements was $\pm$2.5%. This was estimated by removing the crystal and the paint, repainting the crystal in a given configuration and remounting the scintillator on the detector and repeating the experiment for a given detector/scintillator crystal configuration.

In the end it may be concluded that these results are inconclusive in regards to whether or not roughening the crystal surface increases the light output able to be measured by the photodiode. The simulations suggest only a small increase in light output of a few percent is possible with roughening. However the SPAD4 photodiodes optically coupled to LYSO have a 511 keV energy resolution of approximately 14 %. An improvement in detector energy resolution would allow small improvements to be distinguished. Also, it may be possible to observe a greater increase in light output by roughening a greater number of sides, as this may produce a significant increase in light output which may be distinguished. Future work with the LYSO crystal will need to be completed for a conclusive result to be obtained.

Chapter 5 – Coincidence Timing Resolution Measurements

Coincidence Timing Resolution is defined by the distribution in time of coincident events detected between two detectors. It is expressed as full width at half maximum (FWHM) [10]. A smaller timing coincidence resolution would translate into a smaller time interval in which coincident photons would need to be detected in order to be accepted in coincidence with another detected photon by the system. Thus the recording of random and scatter coincidences would be reduced, improving the final image quality.

5.1 Electronics Familiarisation

An investigation into the electronics to be used along with a familiarisation with the capabilities of the electronics has been conducted. For coincidence timing resolution measurements timing modules such as timing filter amplifiers, constant fraction discriminators and a time to amplitude converter need to be utilised.

Timing Filter Amplifiers are used to amplify the timing signal and provide some shaping of the signal, with independent RC integrator and CR differentiator controls. They are designed to have output rise times in the low nanosecond or sub nanosecond range, allowing this without compromising linearity and temperature stability [48].

Constant Fraction Discriminators (CFD) are used to pick off the optimum time signal by triggering at the optimum fraction for any pulse height. Constant fraction timing is a much better method of picking off the timing signal as opposed to leading edge timing.

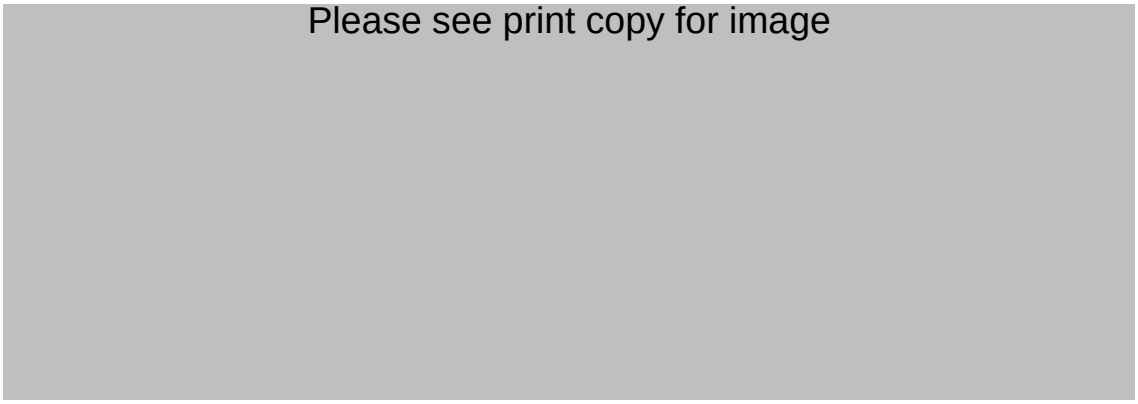

Figure 5.1: Leading Edge Timing (left) and Constant Fraction Timing (right) [49]

As may be seen from the figure on the left in figure 5.1, leading edge timing merely uses the leading edge of an input pulse crossing over a discriminator level. Thus the time of the output pulse will vary with the pulse amplitude, producing an inaccuracy in the timing measurement that is dependant on pulse shape and height. This variation is referred to as time jitter. Constant fraction timing minimises this effect, as it has the same cross over point regardless of pulse height. This may be seen in the figure on the right. Constant fraction timing works by splitting the input pulse into two branches. In one branch the pulse is delayed by a fixed time whilst in the other the pulse is attenuated by a fixed fraction and inverted. The pulses in both branches are added, with the discriminator circuitry triggering if the input pulse is above a certain threshold voltage. However the logic pulse is not produced until the added pulse changes polarity. This crossover point is independent of pulse height. This technique ensures all pulses have the same rise time. The constant fraction discriminator also incorporates a timing discriminator that triggers on the zero crossing, which provides a time marker at the optimum fraction of pulse height [48].

The time to amplitude converter is an essential component in timing measurements. This module produces an output pulse which is proportional to the time between two specific events. The single channel analyser allows discrimination of a particular energy range of the input pulses.

5.1.1 Electronics Familiarisation Experimental Method

The effect of the zero crossing time resolution using just the NIM modules was measured. This involved an investigation into the zero crossing time with variance in the rise time. This was done using the same method as Pausch [50]. The experimental setup used is shown in figure 5.2.

In figure 5.2, the abbreviations represented, and the settings for each piece of equipment are as follows:

PPG – Ortec 419 Precision Pulse Generator, Pulse Height = 2, Normalise = 0, Rise time = min, 50ns, 100ns, 250ns, Attenuated Output used

TFA1 – Ortec 474 Timing Filter Amplifier, Coarse Gain = 1, Fine Gain = 2, Int = 20ns, Diff = 200ns, Non Inv.

TFA2 – Ortec 454 Timing Filter Amplifier, Coarse Gain = 1, Fine Gain = 2, Int = 20ns, Diff = 200ns, Negative.

CFD – Ortec 935 Quad 200MHz Constant Fraction Discriminator

CFD1 – Threshold = 75mV, closed delay

CFD2 – Threshold = 25mV, open delay

DLY – Ortec 425A Delay, Delay = 0ns or 40ns.

TAC – Ortec 567 Time to Amplitude Converter/SCA, Range = 500ns

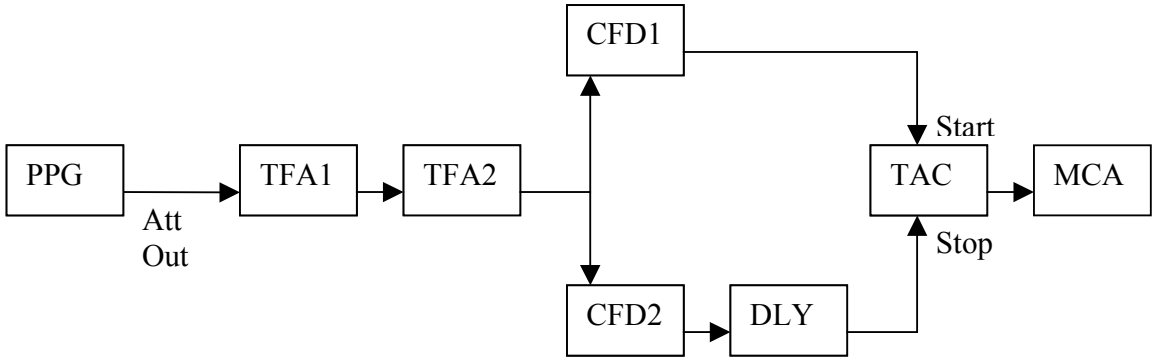

Figure 5.2 – Zero Crossing Time Resolution Measurements with a Pulse Generator

The signal from the precision pulse generator was amplified and shaped by two timing filter amplifiers in series. This was necessary to produce the required amplification required. The signal was then split into two, with the start signal being produced by the constant fraction discriminator with the closed delay, which thus ensures normal operation of the CFD, with the CFD triggering on optimum fraction. The second CFD was set with an open delay, which thus turns it into a zero crossing discriminator, triggering on the zero crossing time.

The rise time of the input pulses was varied, with measurements taken at the minimum rise time, 50 ns, 100 ns, and 250 ns. The delay was used to calibrate the time axis, with a delay time of 40 ns used. These measurements allowed comparison of rise time to FWHM, and rise time to peak position.

The precision pulse generator was then replaced with a photomultiplier tube, with a sodium source used to provide counts. The same measurement was taken with the photomultiplier tube, as the signal measured from radiation is of a slightly different waveform to the perfect pulse given out by the pulse generator. This setup provides a closer look at the capabilities of the electronics using a detector and a source which is closer to the true experimental setup to be used in the coincidence timing resolution measurements.

The settings for the zero crossing time resolution measurements are shown:

PMT - This was a Saint-Gobain Crystals and Detectors, Bicron Model 2M2/2. This PMT has a NaI(Tl) crystal which measures 2” by 2”, along with a PMT size of 2”. This model PMT has an energy range from 15 keV to 3 MeV [51]. PMT was operated with a HV (High Voltage) of 1000 V supplied by an Ortec 459 HV Supply
TFA1 – Ortec 474 Timing Filter Amplifier, Coarse Gain = 20, Fine Gain = 12.5, Int = 20 ns, Diff = 200 ns
TFA2 – Ortec 474 Timing Filter Amplifier, Coarse Gain = 4, Fine Gain = 2, Int = 20 ns, Diff = 200 ns
CFD – Ortec 935 Quad 200MHz Constant Fraction Discriminator
CFD1 - Threshold = 100 mV, closed delay
CFD2 - Threshold = 100 mV, open delay
Delay – Ortec 425A Delay, Set to 0 ns, or 40 ns for time calibration
TAC/SCA – Ortec 567 TAC/SCA – Time Range = 500 ns, TAC output to MCA input
MCA – Amptek MCA 8000A – 10 V ADC

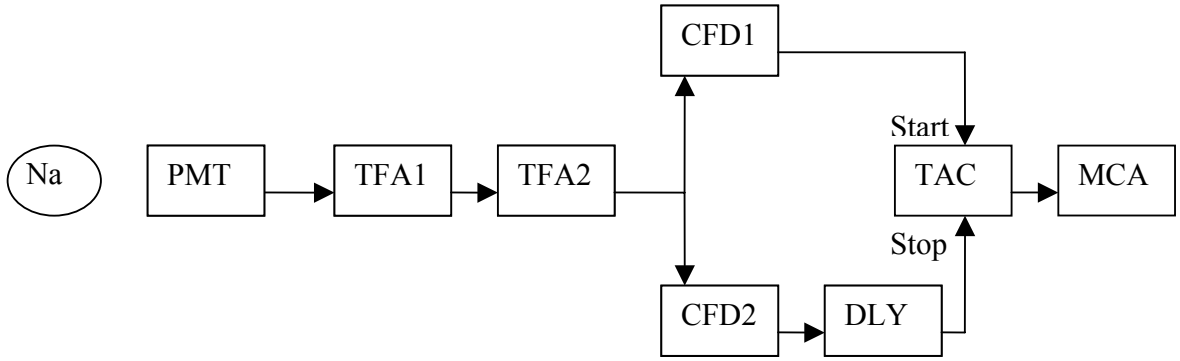

Figure 5.3: Zero Crossing Time Resolution Measurements with a PMT

A gated channel was also included to investigate the effect of an energy gate with only one channel. The gating channel was set by measuring the 511 keV peak, and setting the SCA to accept only these pulses. The logic shaper and delay is set to ensure that the gating channel occurs at the same time as the output from the TAC. The modules and the settings for those used in the gating channel are shown:

Spec Amp – Canberra 2020 Spectroscopy Amplifier, Coarse Gain = 3000, Fine Gain = 1, Shaping Time = 0.25 μs, Negative Input Polarity
SCA – Ortec 551 Timing SCA, Window = 5, Lower Level = 5.6, Window Mode
LS/D – Canberra 2055 Logic Shaper and Delay, Delay = 1 μs, Width =3. 5, Amp = 5

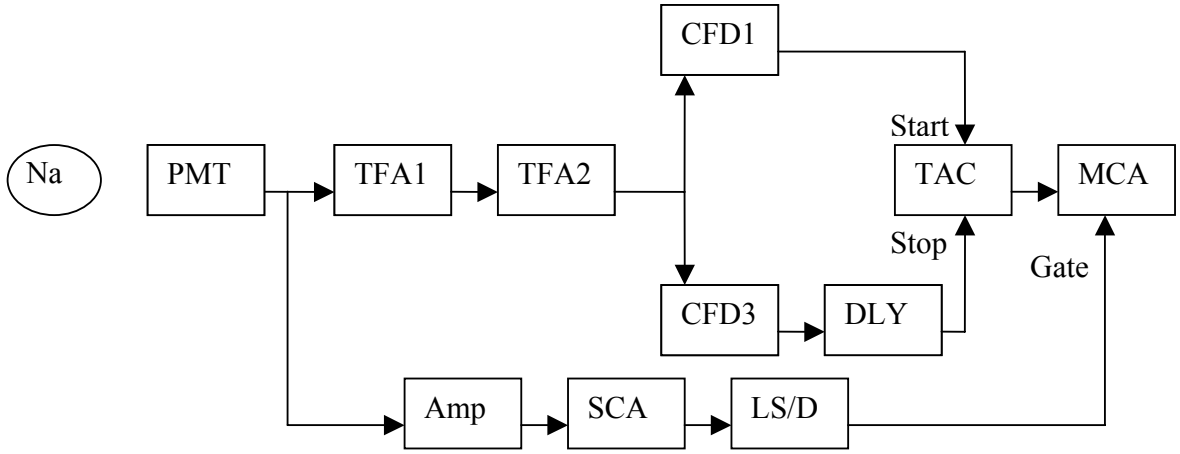

Figure 5.4: Gated Zero Crossing Time Resolution Measurements with a PMT

5.1.2 Electronics Familiarisation Results

The results for the electronics zero crossing time FWHM measurements are shown. Initially the time axis was calibrated.

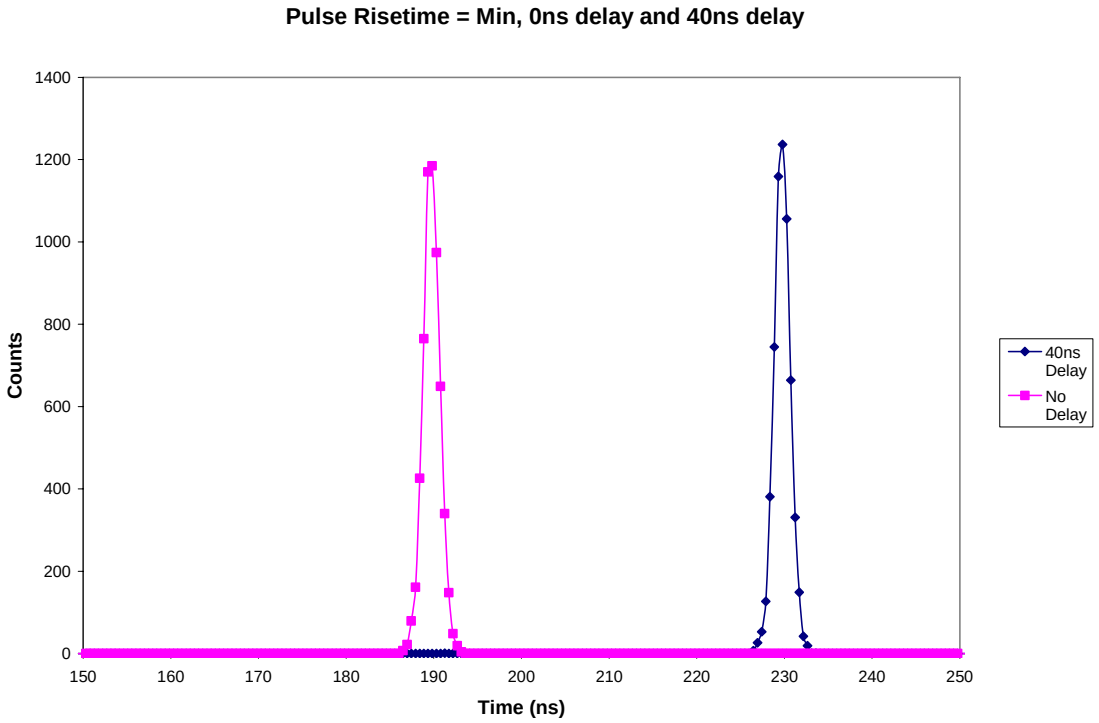

Figure 5.5: Time Axis Calibration Spectrum

As may be seen from the previous spectra, the 40 ns delay was used to calibrate the time axis. This produced a time calibration value of 0.48 ns/channel. This value was multiplied by the channel to produce results in ns.

Rise time (ns)	Centroid (ns)	FWHM (ns)
0	189.27	2.16
50	195.44	2.30
100	209.41	2.99
250	219.61	5.13

Table 5.1: Results of Varying Rise time

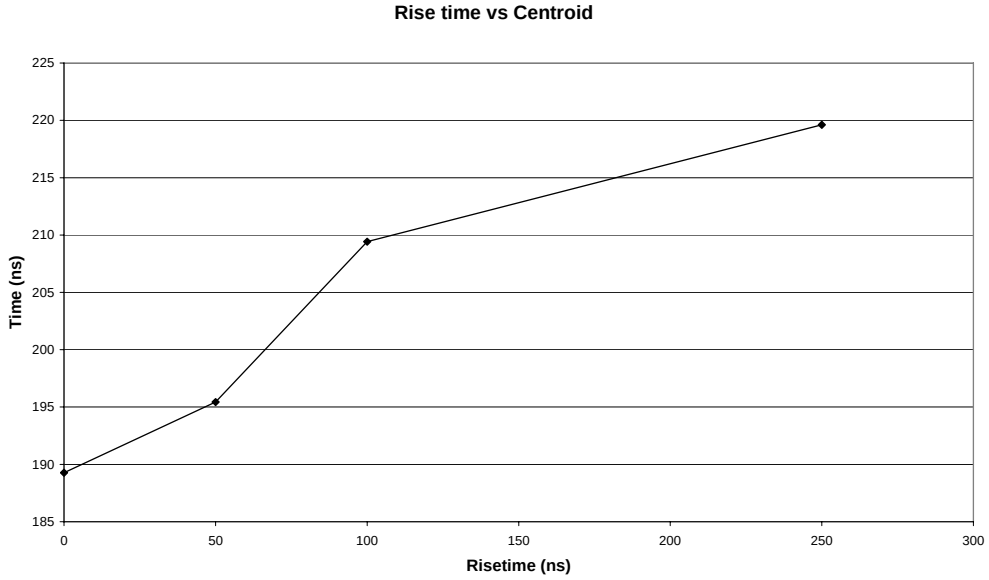

Figure 5.6: Timing Signal Centroid as a Function of Signal Rise Time

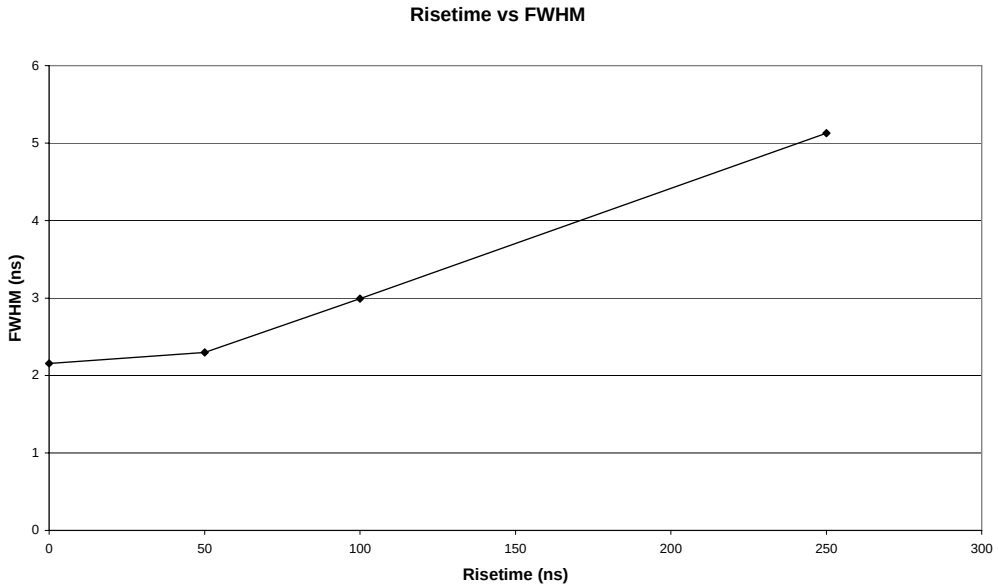

Figure 5.7: Timing Signal FWHM as a Function of Signal Rise Time

With increasing rise time, both the FWHM and the peak position increases. Therefore best results will be obtained with a smaller rise time of the initial pulse.

The results for the PMT zero crossing time measurements are shown in figure 5.8.

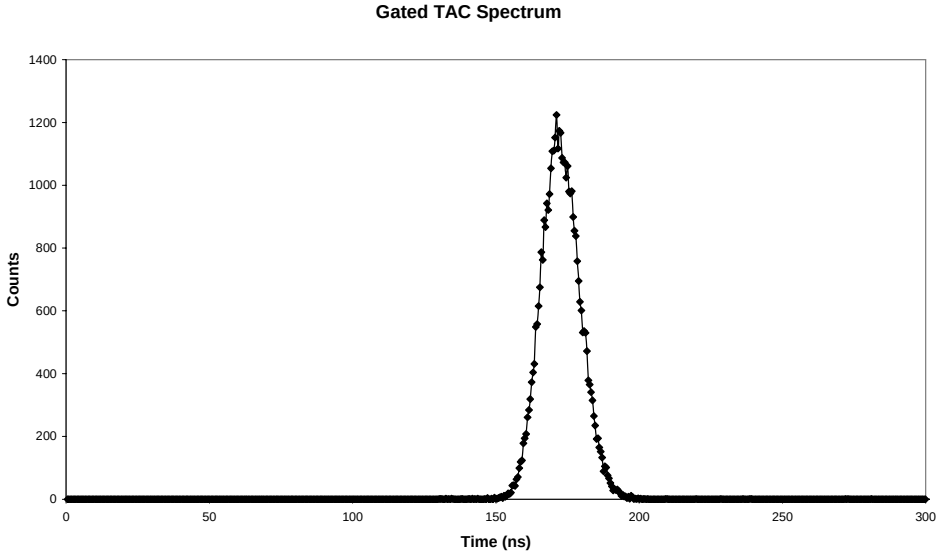

Figure 5.8: Gated TAC Spectrum

The resolution of the PMT zero crossing time measurement was calculated to be 10.30 ns FWHM. The ungated TAC spectrum is shown below, with the gate producing a better result in the resolution. The pulses recorded with the PMT and Na-22 has a greater fluctuation in rise time, and this produces the variance in time. The use of the gate improves the resolution, removing the counts not related to the emission of the Na-22 source.

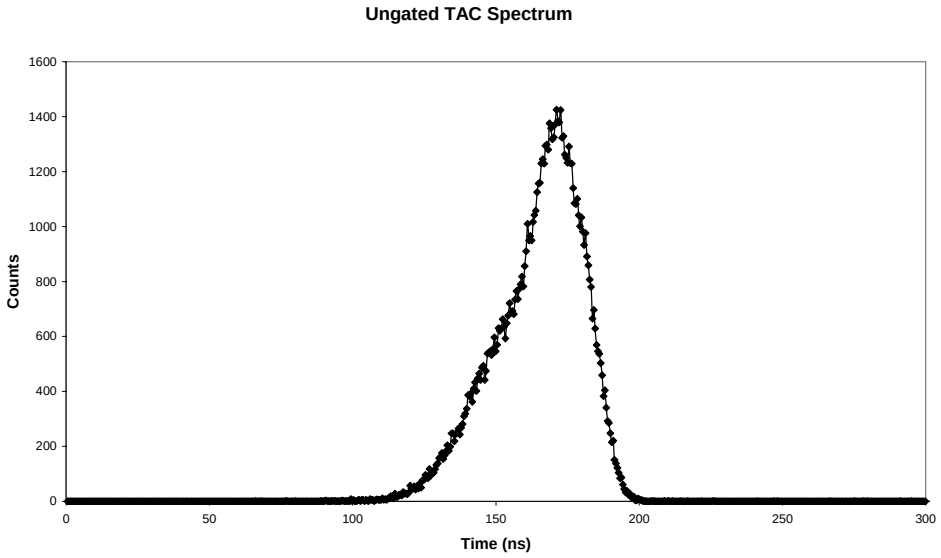

Figure 5.9: Ungated TAC Spectrum

5.2 Single Gate Timing Coincidence Measurements

5.2.1 Single Gate Method

The timing resolution was measured using a similar experimental setup to a previous honours project [52].

In figure 5.10, the equipment and settings used are as follows:

PMT – Photomultiplier Tubes with NaI crystals mounted. PMT1 was operated with a HV (High Voltage) of 1000 V supplied by an Ortec 459 HV Supply

PD – Photodiode with 3 mm x 3 mm LYSO crystal mounted with optical grease, Operated at 50 V reverse biased

TFA – Ortec 474 Timing Filter Amplifier, Coarse Gain = 10, Fine Gain = 12.5, Int = Out, Diff = 50 ns

Pulse Amp – Type 235 Pulse Amplifier, Coarse Gain = 500, Fine Gain = 10, Int = 100 ns, Diff = 50 ns

P/A/S – Ortec 4890 Pre-amp/Amp/SCA, Coarse Gain = 64, Fine Gain = 10, Window = 1.42, Lower Level = 2.15

LS/D – Canberra 2055 Logic Shaper and Delay, Delay = 2.96 μs, Width = 4.5, Amp = 9

CFD – Ortec 935 Quad 200MHz Constant Fraction Discriminator, CFD1 Threshold = 100 mV, CFD2 Threshold = 45 mV

Delay - Ortec 425A Delay, Set to 48 ns, or 98 ns for time calibration

TAC/SCA – Ortec 567 TAC/SCA – Time Range = 500 ns, TAC output to MCA input

MCA – Amptek MCA 8000A – 10 V ADC

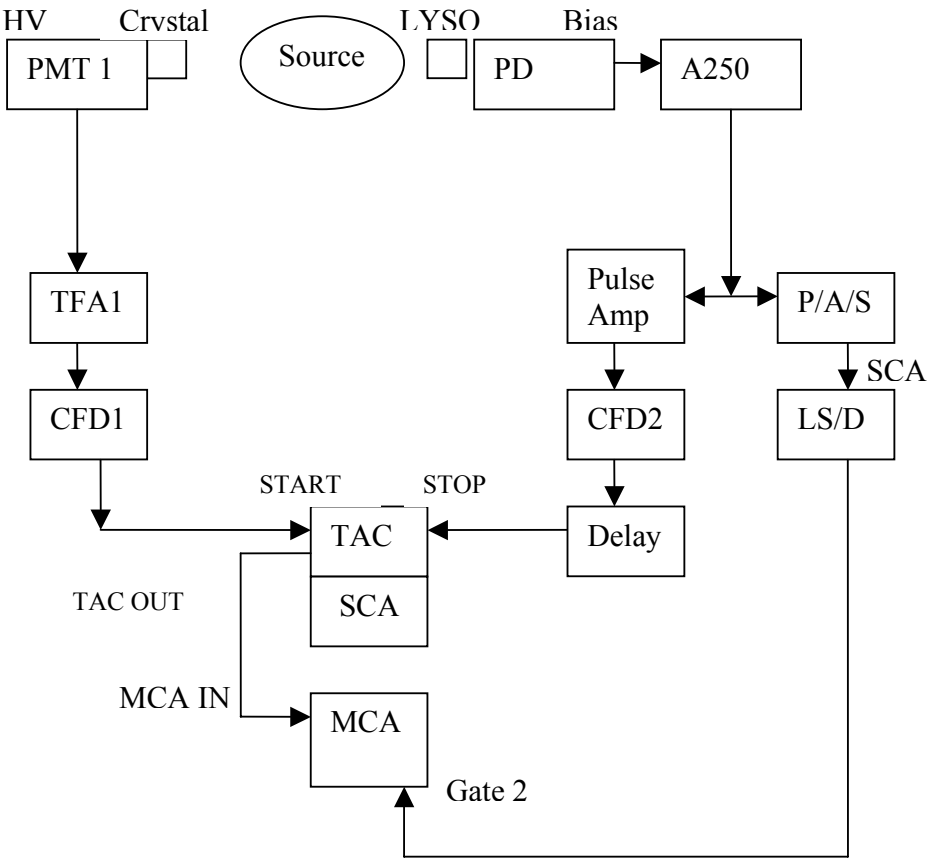

Figure 5.10: Single Gate Time Resolution Equipment Diagram

The gate was set using the amp output of the Preamp/Amp/SCA. A Na-22 spectrum was obtained using this output, and the position and FWHM of the 511 keV peak were recorded. The settings of the SCA were then set for this peak, and the SCA output was used in the "Gate 2" input of the MCA. Another spectrum was obtained, with the SCA settings and use of the gate only allowing a small range of pulses to be recorded. The SCA settings were then reset to ensure that only the counts which contributed to the 511 keV peak were allowed by the gate.

5.2.2 Single Gate Measurement Results

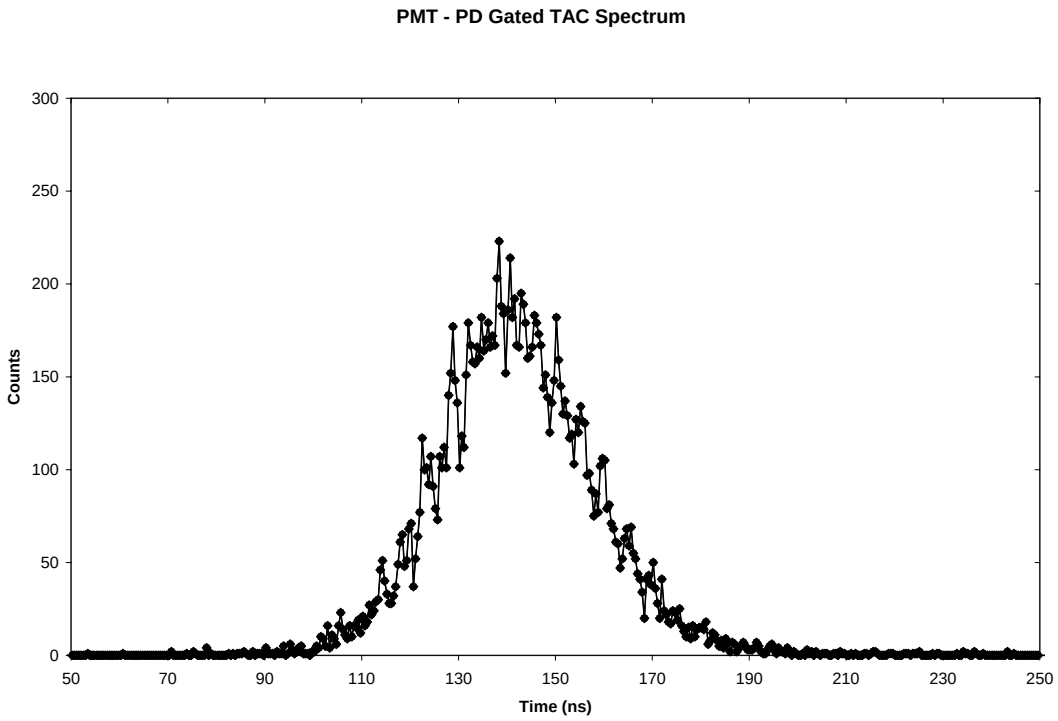

Figure 5.11: Single Gated PMT – PD TAC Spectrum

The FWHM for this peak is 49.399 channels, and its Centroid occurs at 205.61. The calculated time calibration, when compared to the spectrum with the 50 ns delay incorporated, is 0.45 ns/channel. Thus the full width time resolution is 22.44 ns. This result is equivalent to the results obtained previously with a similar setup before corrections were applied. The ungated TAC spectrum is shown to indicate the effects of the gate on the results.

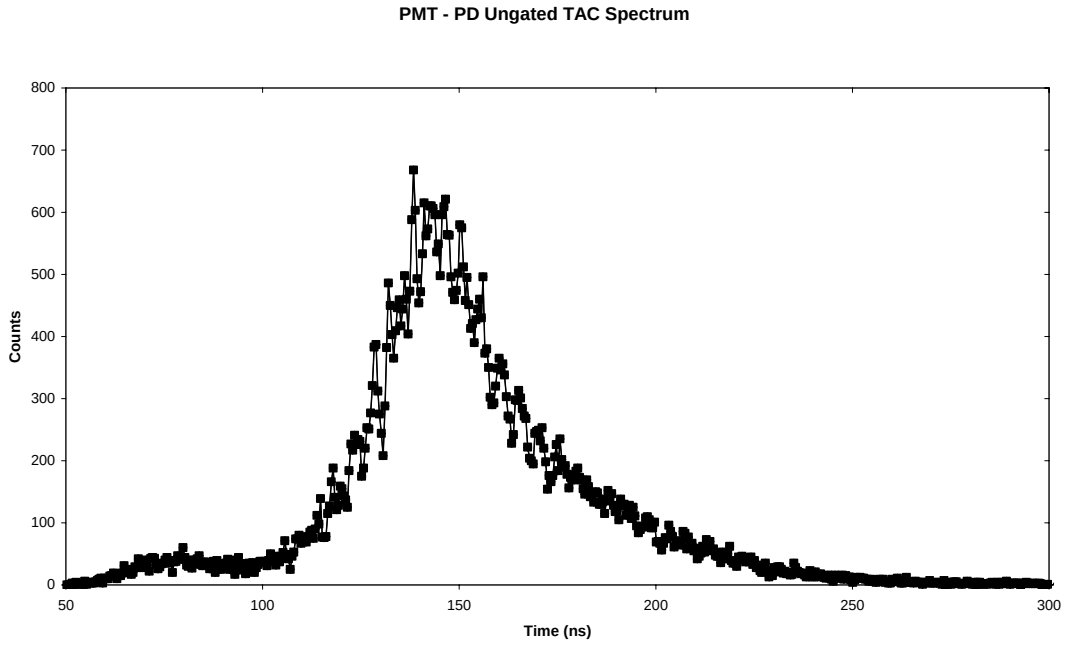

Figure 5.12– PMT – PD Ungated TAC Spectrum

When comparing the gated and ungated PMT – PD TAC spectra, it may be observed that gating provides much better time resolution through allowing only the 511 keV counts to be accepted. This reduction in time resolution is quite significant even with the presence of the single gate. Much of the noise and scatter which occurs before the peak is removed. It was anticipated that gating the TAC output through both channels would produce an even better result, as this would reduce noise and scatter from both channels. This was also investigated.

5.3 Double Gate Timing Coincidence Measurements

5.3.1 Double Gate Method

The timing resolution was measured with a double gate using a similar experimental setup to that utilised in the previous section.

In figure 5.13, the equipment and settings used are as follows:

PMT – Photomultiplier Tubes with NaI crystals mounted. PMT1 was operated with a HV (High Voltage) of 1000 V supplied by an Ortec 459 HV Supply

PD – Photodiode with 3 mm x 3 mm LYSO crystal mounted with optical grease, Operated at 50 V reverse biased

TFA – Ortec 474 Timing Filter Amplifier, Coarse Gain = 10, Fine Gain = 12, Int = Out, Diff = 50 ns

Pulse Amp – Type 235 Pulse Amplifier, Coarse Gain = 500, Fine Gain = 10, Int = 100 ns, Diff = 50 ns

P/A/S – Ortec 4890 Pre-amp/Amp/SCA, Coarse Gain = 64, Fine Gain = 10, Window = 1.42, Lower Level = 2.15

LS/D – Canberra 2055 Logic Shaper and Delay, Delay = 2.96 μs, Width = 5, Amp = 7

Spec Amp – Canberra 2020 Spectroscopy Amplifier, Coarse Gain = 300, Fine Gain = 1.3, Shaping Time = 0.25 μs, Negative Input Polarity

SCA – Ortec 551 Timing SCA, Window = 1.30, Lower Level = 0.70, μs = 5

G/DG – Ortec 416A Gate and Delay Generator, Delay = 2.84 μs, 11 μs range, Positive Output to Gate 2

CFD – Ortec 935 Quad 200MHz Constant Fraction Discriminator, CFD1 Threshold = 100 mV, CFD2 Threshold = 50 mV

Delay – Ortec 425A Delay, Set to 50 ns, or 90 ns for time calibration

TAC/SCA – Ortec 567 TAC/SCA – Time Range = 500 ns, TAC output to MCA input

MCA – Amptek MCA 8000A – 10 V ADC

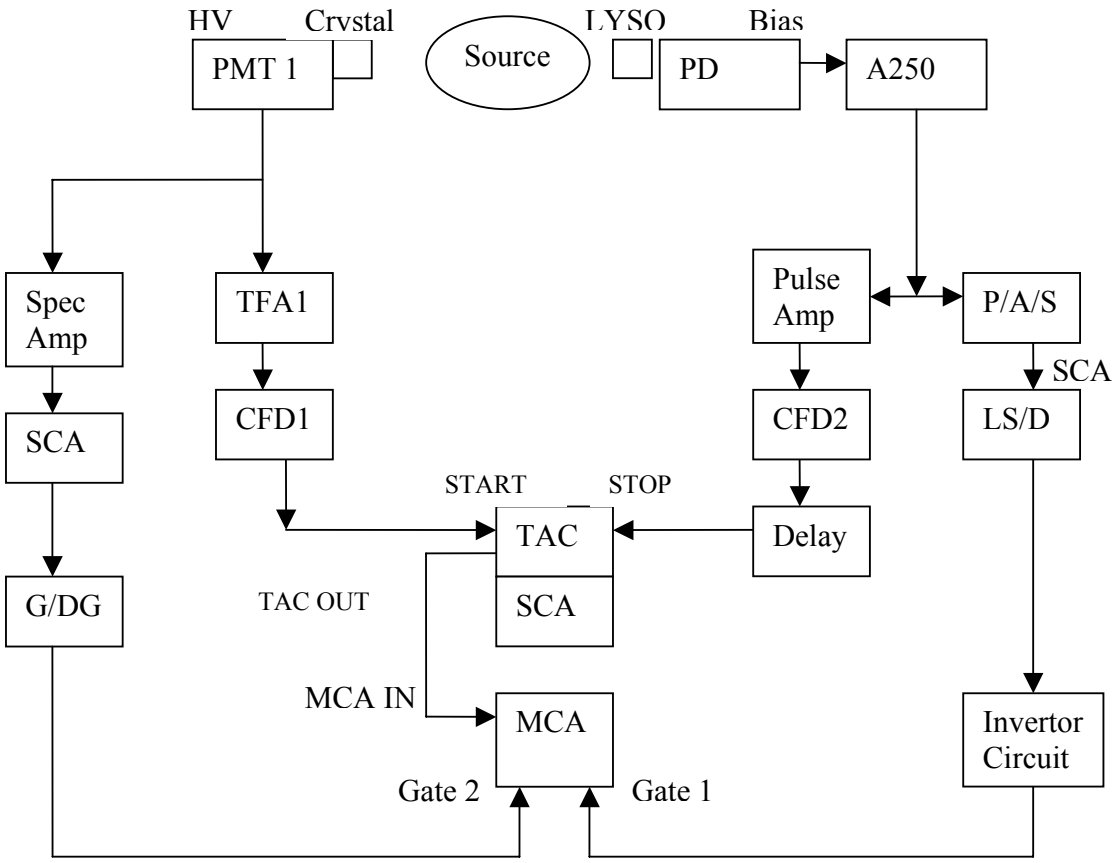

Figure 5.13: Double Gate Time Resolution Equipment Diagram

Gate 1 is the "Active High" gate; the signal stays "high" and does not accept counts unless the gate pulse drops "low", allowing counts to be accepted. Gate 2 is the "Active Low" gate; the signal stays "low" until an event is measured which occurs within the gating signal, which then causes it to produce a "high" logic pulse, accepting the counts. When the signal stays "low" no input is recorded.

Gate 1 had been set earlier for the single gated measurements. Gate 2 was set much in a similar manner to Gate 1. The SCA settings were determined by taking a Na-22 spectrum using the spectroscopy amplifier, and setting the lower level and window as to only accept counts from the 511 keV peak.

Both gates were set similarly, with the amp outputs being input into the MCA, and this gated with an SCA output. These gates are delayed slightly to match up with the output from the TAC, with a CRO being used for this.

The connection diagram of the inverter is shown below. 5 V was input into the V_{CE} pin on the chip. The input from the gate channel was then connected to A1, and the inverted output was taken from Y1, and this was input into "gate 1" on the MCA. This inverter circuit had not been used previously, and was necessary due to the configuration of the gating mechanisms associated with the MCA.

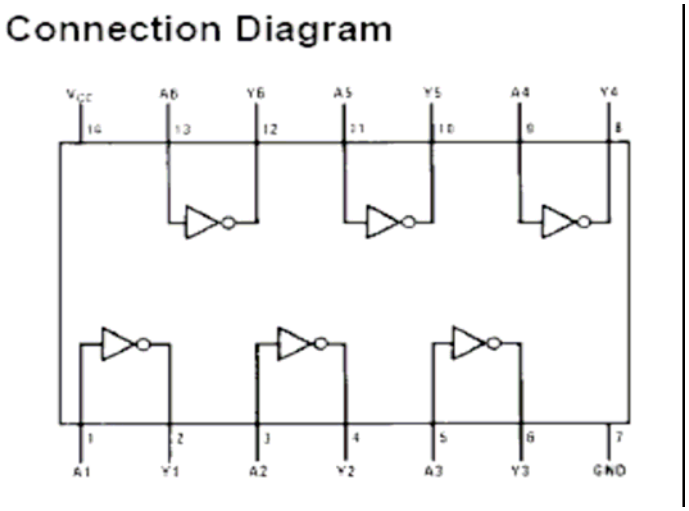

Figure 5.14– 74LS04N Hex Inverting Gate Connection Diagram

$Y = \overline{A}$

Input	Output
A	Y
L	H
H	L

H = HIGH Logic Level
L = LOW Logic Level

Table 5.2: Function Table for 74LS04N Hex Inverting Gate

5.3.2 Double Gate Results

The results shown were the best obtained. These results occurred with settings of:

TFA – Int = out, Diff = 50 ns

Pulse Amp – Int = 100 ns, Diff = 50 ns.

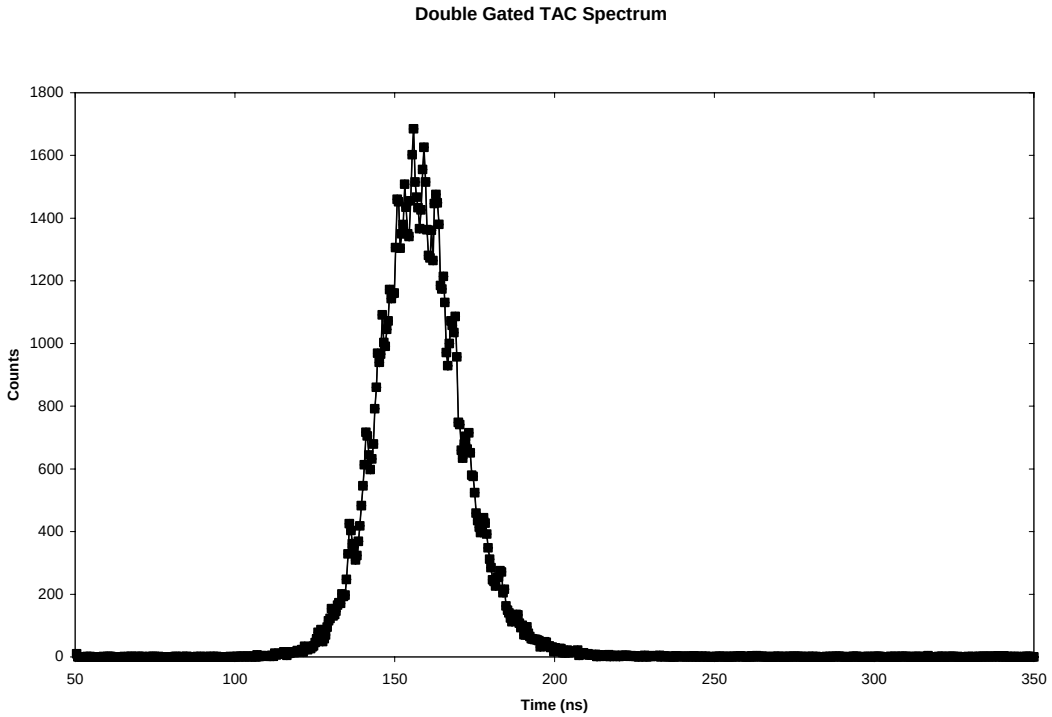

Figure 5.15: Double Gated TAC Spectrum

The FWHM for this peak is 54.59 channels, and its Centroid occurs at channel 229.59. The calculated time calibration, when compared to the spectrum with the 40 ns delay incorporated, is 0.47 ns/channel. A result of 25.47 ns was obtained with the double gate. The presence of the double gate reduces the FWHM of the timing peak quite dramatically when compared to the ungated TAC spectrum. However this result is comparable to the single gated TAC spectrum results though it is slightly higher.

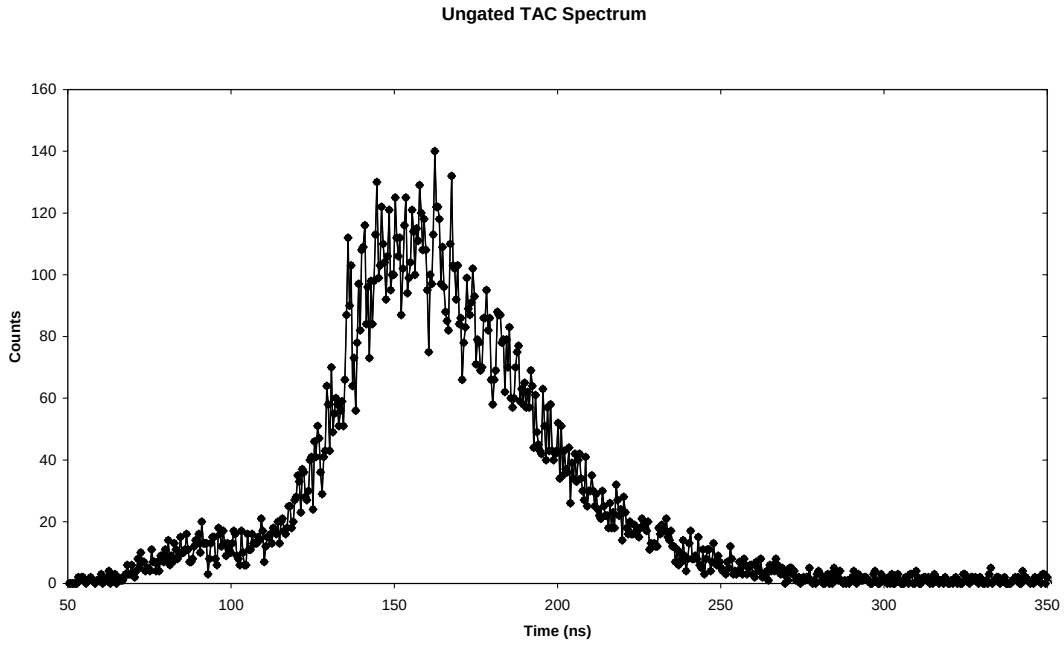

Figure 5.16: Ungated TAC Spectrum

The ungated TAC spectrum is much the same as seen in the previous section. Again the presence of gating removes any counts outside of the gating window, with only 511 keV counts registered by the MCA. This produces an obvious narrowing of the peak, and removes all of the noise which occurs before and after the main timing peak. However there was not as much of an improvement as had been expected. This will be discussed in the next section.

5.4 Coincidence Time Resolution Discussion

The best timing resolution achieved with the single gating setup was 22.44 ns. The best timing resolution achieved with the double gating setup was 25.47 ns. This result is not as anticipated, as the expectation was for the double gate setup to show the best timing resolution. These results are significantly higher than the 9.4 ns FWHM timing resolution which was achieved by Levin [4]. Levin's result was achieved using LSO crystal coupled to the photomultiplier tube, which is much faster than the NaI crystal used here. Levin also had Fluorine–18 (F–18) sources available, which are much stronger positron emitters than Na-22.

The coincident timing resolution is a measure of the uncertainty in the arrival time (as measured by the detector system) of the back-to-back 511 keV gamma ray photons emitted simultaneously on annihilation of the positron with the electron. There is a contribution due to the electronics and each detector module which adds in quadrature to give the final measured timing resolution. The experimentally deduced 3σ value, where σ is equal to the FWHM divided by 2.35, of the measured timing resolution is an estimate of the coincident timing window necessary for the maximum detection efficiency possible for the given detector/scintillator configuration used to make up the PET scanner.

Experimental errors in the measurement of the coincidence time resolution may be due to a combination of factors. Initially, measurements were made to investigate the contribution to the error from the electronics (section 5.1). Contributions to experimental error would arise from the electronics noise, the detectors and statistical error. The main source of experimental error in coincidence timing resolution measurements is due to electronic noise in the CFD signal, which causes fluctuations in the triggering time and produces timing jitter.

There are many possible reasons why the time resolution results were not improved with the double gate setup. During the experiments many problems due to the noise level were encountered, with on many occasions and with many settings a signal unable to be recognised from the noise. Though this wasn't tested at the time, it was concluded that it was due to the age of the equipment and cabling used. There is also the statistical difference between the number of counts taken in these spectra, the single gated TAC spectrum peak has just over 200 counts maximum, whilst the double gated TAC spectrum peak has approximately 1600 counts maximum. There is the possibility that with better statistics, and if the single gated spectrum had been taken for a longer period of time, the corresponding FWHM results could be reversed, as there is a high probability that the peak width will widen with a greater number of counts in the peak.

Chapter 6 – Conclusions

An investigation into the charge collection properties of PET detectors, in particular SPAD4 photodiodes coupled with LYSO crystals has been completed. This involved the use of three different techniques to look into different aspects of the PET detectors.

The Ion Beam Induced Charge Collection characteristics of the SPAD4 photodiodes were examined. The IV and CV characteristics for each SPAD4 photodiode were measured, and then a single SPAD4 photodiode was bombarded with ions and the charge measured for different bias voltages. The effect on the guard ring of the SPAD4 was also observed, with this guard ring generally not being used and biased during measurements with these photodiodes.

From the IBICC measurements, it was concluded that 50 V reverse bias over the SPAD4 photodiodes produced best FWHM energy resolution, along with good charge collection efficiency. At voltages lower than 30 V, incomplete charge collection occurred, and at voltages greater than 60 V over depletion of the photodiode occurred. As 50 V reverse bias produced the best FWHM energy resolution, along with full charge collection, this was concluded to be the most suitable bias voltage for use with the SPAD4 photodiode.

The scintillation photon collecting capabilities of the LYSO crystals were simulated and their efficiency at collection when coupled with SPAD4 photodiodes was measured experimentally. The scintillation photon collecting capabilities were simulated using two different simulation programs, Scintillation Program and DETECT2000, and compared against each other. Each produces similar trends, though they both modelled the crystal interactions slightly differently.

Both Scintillation Program and DETECT2000 produced similar results for a fully clad crystal, with 58.95 % and 57.95 % light output respectively. This was the best result simulated which was able to be compared between both programs. Both programs also simulated a slight increase in light output when one side is roughened. Scintillation Program produced results of 55.39 % with all sides clad except for side 2, and 57.89 %

when the unclad side was roughened. Similarly with DETECT2000, results of 46.54 % and 49.23 % were obtained before and after roughening side 2.

Physical measurements with the SPAD4 photodiodes and LYSO crystal in regards to the effect of roughening the crystal surface proved to be inconclusive. A slight increase in light output was obtained with the roughened LYSO crystal with Cs-137. However a slight decrease in light output was obtained with the roughened LYSO crystal with Na-22. Also, the increase, or decrease in light output was insignificant when the FWHM of the energy peaks are considered. Detectors with improved energy resolution, along with measurements with more crystal sides roughened, would be beneficial in concluding whether roughening the crystal surface improves the light output as the simulations suggest.

The timing resolution properties of the SPAD4 photodiodes when coupled with LYSO crystal and in coincidence with a photomultiplier tube were also investigated. Through the use of gating, the coincidence timing resolution results were 22.44 ns with a single gate and 25.47 ns with a double gate setup. Though experimentally better results have been obtained in the past, with results sub 20 ns having been achieved with these photodiodes in a previous project, the use of a double gate had not yet been attempted with these photodiodes. Though the results were poorer than that which had been achieved in the past, they are significant as they show that the use of a double gate is possible. Many improvements could be made, one being a stronger source which would improve the count rate, along with a faster PMT. The gating setup could also be simplified, though that would require the purchase of new equipment for this to occur. As always, the results could be improved with faster equipment, more efficient detectors and crystals with a faster decay time. Also, perhaps due to the low signal to noise ratio, and low count rates with a single crystal, development in arrays of SPAD photodiodes with LYSO crystal arrays would be the focus of future work.

Reference:

[1] – Takacs, G.J., Rosenfeld, A.B., Lerch, M.L.F. – "Design and Simulation of Continuous Scintillator With Pixellated Photodetector", IEEE Transactions on Nuclear Science, Vol. 48, No. 4, August 2001, pg 1412 - 1417

[2] – Doshi, Niraj K., et al – "Comparison of Typical Scintillators for PET" IEEE Nuclear Science Symposium Conference Record, 2002, Volume 3, pg 1420 - 1423

[3] - Pepin, Catherine Michelle, Berard, Philippe, Perrot, Anne-Laure, et al. - "Properties of LYSO and Recent LSO Scintillators for Phoswich PET Detectors", IEEE Transactions on Nuclear Science, Vol 52, No. 3, June 2004, pg 789 – 795

[4] - Levin, Craig S., Hoffman, Edward J. - "Investigation of a New Readout Scheme for High Resolution Scintillation Crystal Arrays Using Photodiodes" IEEE Transactions on Nuclear Science, Vol 44, No. 3, June 1997, pg 1208 – 1213

[5] - http://www.pet.dote.hu/Local_Information/Tech__Background/PET_Camera/body_pet_camera.html

[6] - http://dels.nas.edu/ilar_n/ilarjournal/42_3/4203_cherry_fig_1_441.jpg

[7] – Hendee, W.R., Ritenour, E.R. – "Medical Imaging Physics" Fourth Edition, Wiley-Liss, 2002, pg 212 - 214

[8] – Sorenson, J.A., Phelps, M.E. – "Physics in Nuclear Medicine" Second Edition, W.B. Saunders Company, 1987, pg 429 – 450

[9] – www.sasta.asn.au/pdfs/PET%20notes.doc

[10] - Hooper, Peter R. – "Development of a New Silicon Based Detector Module for PET", Masters Thesis, Centre for Medical Radiation Physics, 2003, pg 3 – 6

[11] - Moses, W.W. – "Advantages of improved timing accuracy in PET cameras using LSO scintillator", IEEE Nuclear Science Symposium Conference Record, Vol. 3, Nov. 2002, pg 1670 – 1675

[12] – Frach, T; Ruetten, W, Fiedler, K, Maehlum, G., Solf, T., Thon, A. – "Assessment of photodiodes as a light detector for PET scanners", IEEE Nuclear Science Symposium Conference Record Vol. 7, Oct. 2004, pg 4177 – 4181

[13] – Ziegler, S.I. – "Development of a small animal PET system", Proceedings of the IEEE, Vol. 93, Issue 4, Apr. 2005, pg 763 – 770

[14] – McElroy, D.P., Pimpl, W., Pichler, B.J., Rafecas, M., Schuler, T., Ziegler, S.I. – "Characterisation and Readout of MADPET-II Detector Modules: Validation of a Unique Design Concept for High Resolution Small Animal PET", IEEE Transactions on Nuclear Science, Vol. 52, No. 1, Feb. 2005, pg 199 - 204

[15] – Tai, Y.-C., Chatziioannou, Silverman, R.W., Meadors, K., Siegel, S., Newport, D.F., Yang, Y., Stickel, J.R., Cherry, S.R. – "MicroPET II: an ultra-high resolution small animal PET system", IEEE Nuclear Science Symposium Conference Record, Vol. 3, Nov. 2002, pg 1848 - 1852

[16] – Sexton, F.W., Horn, K.M., Doyle, B.L., Shaneyfelt, M.R., Meisenheimer, T.L. – "Effects of Ion Damage on IBICC and SEU Imaging", IEEE Transactions on Nuclear Science, Vol. 42, No. 6, Dec. 1995, pg 1940 – 1948

[17] – Angell, D., Marsh, B.B., Cue, N., Jing-Wei, M. – "Charge collection ion microscopy: Imaging of defects in semiconductors with a positive ion microbeam", Nuclear Instruments and Methods in Physics Research B Vol. 44, Issue 2, Dec 1989, pg 172 – 178

[18] – Campbell, A., Knudson, A., McMorrow, D., Anderson, W., Roussos, J., Espy, S., Buchner, S., Kang, K., Kerns, D., Kerns, S. – "Ion Induced Charge Collection in GaAs MESFETs", IEEE Transactions on Nuclear Science, Vol. 36, No. 6, Dec 1989

[19] – Breese, M.B.H., Grime, G.W., Watt, F. – "The generation and applications of ion beam induced charge images", Nuclear Instruments and Methods in Physics Research B, Vol. 77, Issues 1-4, May 1993, pg 301 – 311

[20] – Normand, E., Oberg, D.L., Wert, J.L., Ness, J.D., Majewski, P.P. – "Single Event Upset and Charge Collection Measurements Using High Energy Protons and Neutrons", IEEE Transactions on Nuclear Science, Vol. 41, No. 6, Dec. 1994, pg 2203 – 2210

[21] – Bogdanovic, I., et al. – "Imaging of radiation detectors properties by IBIC", Nuclear Instruments and Methods in Physics Research B 130 (1997) 513 - 517

[22] – Yang, C., Jamieson, D.N., Hearne, S.M., Pakes, C.I., Rout, B., Gauja, E., Dzurak, A.J., Clark, R.G. – "Ion-beam-induced-charge characterization of particle detectors", Nuclear Instruments and Methods in Physics Research B. 190 (2002) pg 212 - 216

[23] – Kimble, T., Chou, M., Chai, B.H.T. – "Scintillation Properties of LYSO Crystals" IEEE Nuclear Science Symposium Conference Record, 2002, Volume 3, pg 1434 – 1437

[24] – Knoll, G. – "Radiation Detection and Measurement" Third Edition, John Wiley and Sons, 2002, pg 53 – 54

[25] - www.photonicmaterials.com/Lyso%20Product%20Spec.pdf

[26] – Lerch, M.L.F., Ward, R., Simmonds, P.E., Pervertailo, V.L., Meikle, S.R., Taylor, G.N., Rosenfeld, A.B. – "Readout of LYSO using a new silicon photodetector for positron emission tomography", IEEE Nuclear Science Symposium Conference Record, Vol. 2, Oct. 2003, pg 1408 – 1412

[27] - Lerch, M.L., Simmonds, P.E., Young, T., Takacs, G.J., Rozenfeld, A., Perevertaylo, V. & Meikle, S., "Modelling the readout performance of a new silicon photodetector for use in PET", IEEE Transactions on Nuclear Science (2007), Submitted.

[28] – Lerch, M.L.F., Rosenfeld, A.B., Simmonds, P.E., Taylor, G.N., Meikle, S.R., Pervertailo, V.L. – "Spectral characterization of a blue enhanced silicon photodetector", IEEE Transactions on Nuclear Science, Vol. 48, Issue 4, Part 1, Aug. 2001, pg 1220 – 1224

[29] – S.E. Holland, N.W. Wang, W.W. Moses – "Development of low noise, back side illuminated silicon photodiode arrays", IEEE Transactions on Nuclear Sciences, Vol. 44, Issue 3, Part 1, June 1997, pg 443 – 447

[30] - Hooper, Peter R. – "Development of a New Silicon Based Detector Module for PET", Masters Thesis, Centre for Medical Radiation Physics, 2003, pg 48 – 52

[31] – Williams, Barry W. – "Principles and Elements of Power Electronics: Devices, Drivers, Applications, and Passive Components", Barry W. Williams 2006

[32] – Cornelius, I., Siegele, R., Rosenfeld, A.B., Cohen, D.D. – "Ion beam induced charge characterisation of a silicon microdosimeter using a heavy ion microprobe", Nuclear Instrument and Methods in Physics Research B 190 (2002) 335 - 338

[33] – Cornelius, I., Rosenfeld, A.B., Siegele, R., Cohen, D.D. – "LET Dependence of the Charge Collection Efficiency of Silicon Microdosimeters", IEEE Transactions on Nuclear Science Vol. 50, No. 6, Dec 2003

[34] - Cornelius, Iwan – "Towards silicon micro dosimetry based verification of Monte Carlo calculations in hadron therapy", Ph.D thesis, University of Wollongong, 2003 pg 45 – 47

[35] – Simon, A., Kalinka, G. – "Investigation of charge collection in a silicon PIN photodiode", Nuclear Instruments and Methods in Physics Research B 231 (2005) pg 507 – 512

[36] – Cornelius, Iwan – "Towards silicon micro dosimetry based verification of Monte Carlo calculations in hadron therapy", Ph.D thesis, University of Wollongong, 2003 pg 38 – 39

[37] – Bradley, P.D., Rosenfeld, A.B., Lee, K.K., Jamieson, D.N., Heiser, G., Satoh, S. – "Charge Collection and Radiation Hardness of a SOI Microdosimeter for Medical and Space Applications", IEEE Transactions on Nuclear Science, Vol. 45, No. 6, Dec 1998, pg 2700 – 2711

[38] – http://www.microbeams.co.uk/Products.html#omdaq

[39] – Overley, J.C., Schofield, R.M.S., Macdonald, J.D., Lefevre, H.W. – "Energy-loss image formation in scanning transmission ion microscopy", Nuclear Instruments and Methods in Physics Research B, Vol. 30, Issue 3, March 1988, pg 337 – 341

[40] – Novotny, R.W., Doring, W.M., Dormenev, V., Drexler, P., Rost, M., Thiel, M. Thomas, A. – "High-Energy Photon Detection With LYSO Crystals", IEEE Nuclear Science Symposium Conference Record, 2006, Volume 2, pg 1118 – 1121

[41] – Moisan, C., Cayouet, F., McDonald, G. – "DETECT2000 – The Object Orientated C++ Language Version of DETECT" Manual Version 5.0, September 1, 2000.

[42] – Vilardi, I., et al. – "Optimization of the effective light attenuation length of YAP:Ce and LYSO:Ce crystals for a novel geometrical PET concept", Nuclear Instruments and Methods in Physics Research A 564 (2006) 506 – 514

[43] – Rothfuss, H., et al – "Monte Carlo Simulation Study of LSO Crystals", IEEE Transactions on Nuclear Science, Vol. 51, No. 3, June 2004

[44] - Dr Phil Simmonds – Private communication

[45] – Moszynski, M, Kapusta, M., Mayhugh, M., Wolski, D., Flyckt, S.O. – "Absolute light output of scintillators", IEEE Transactions on Nuclear Science, Vol. 44, Issue 3, Part 1, June 1997, pg 1052 – 1061

[46] – Holl, I., Lorenz, E., Mageras, G. – "A measurement of the light yield of common inorganic scintillators", IEEE Transactions on Nuclear Science, Vol. 35, Issue 1, Part 1-2, Feb. 1988, pg 105 – 109

[47] – G. Bertuccio and R. Casiraghi – "Study of Silicon Carbide for X-ray Detection and Spectroscopy", IEEE Transcations on Nuclear Sciences, Vol. 50, No. 1, August 2003, pg 175 - 185

[48] - Ortec Modular Pulse Processing Electronics Manual

[49] - Canberra Nuclear Products Group Manual (Edition 8)

[50] – G. Pausch, H-G Ortlepp, W. Bohne, H. Grawe, D. Hilscher, M. Moszynski, D. Wolski, R. Schubart, G. de Angelis and M. de Poli - "Identification of light charged particles and heavy ions in silicon detectors by means of pulse – shape discrimination"

IEEE Transactions on Nuclear Sciences, Vol. 43, No. 3, June 1996

[52] - http://www.bicrondirect.com/msty.htm

[51] – Young, Tony – “Timing Properties of Detectors for PET”, Honours Thesis, Centre for Medical Radiation Physics, 2005

Appendix 1 – Crystal Profile Data

Crystal 1

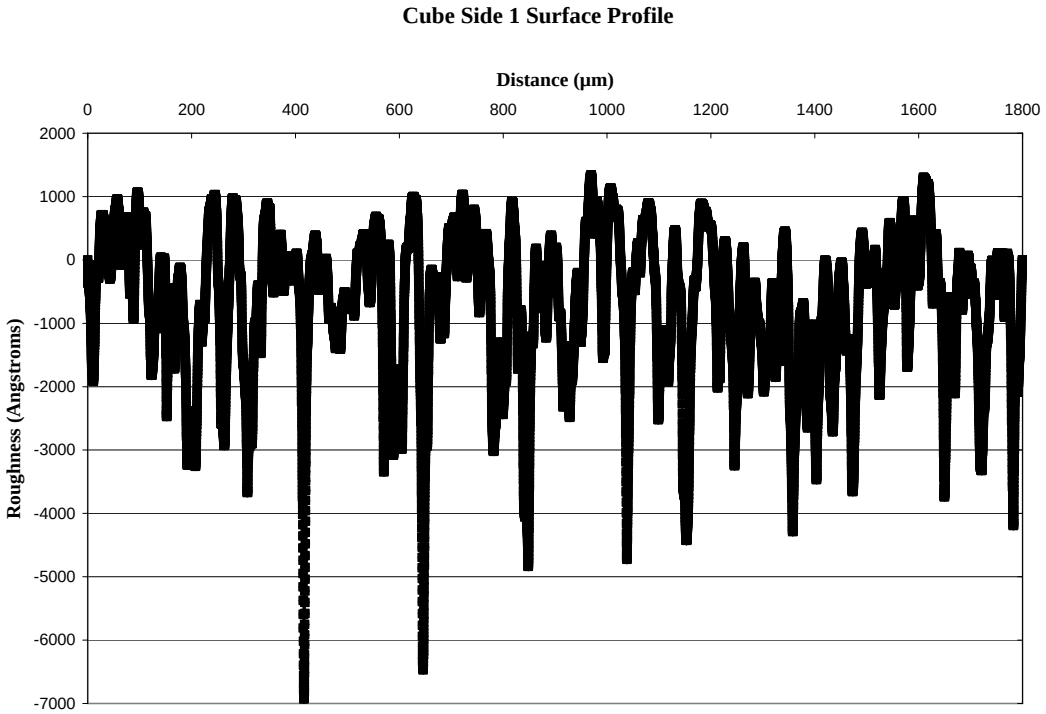

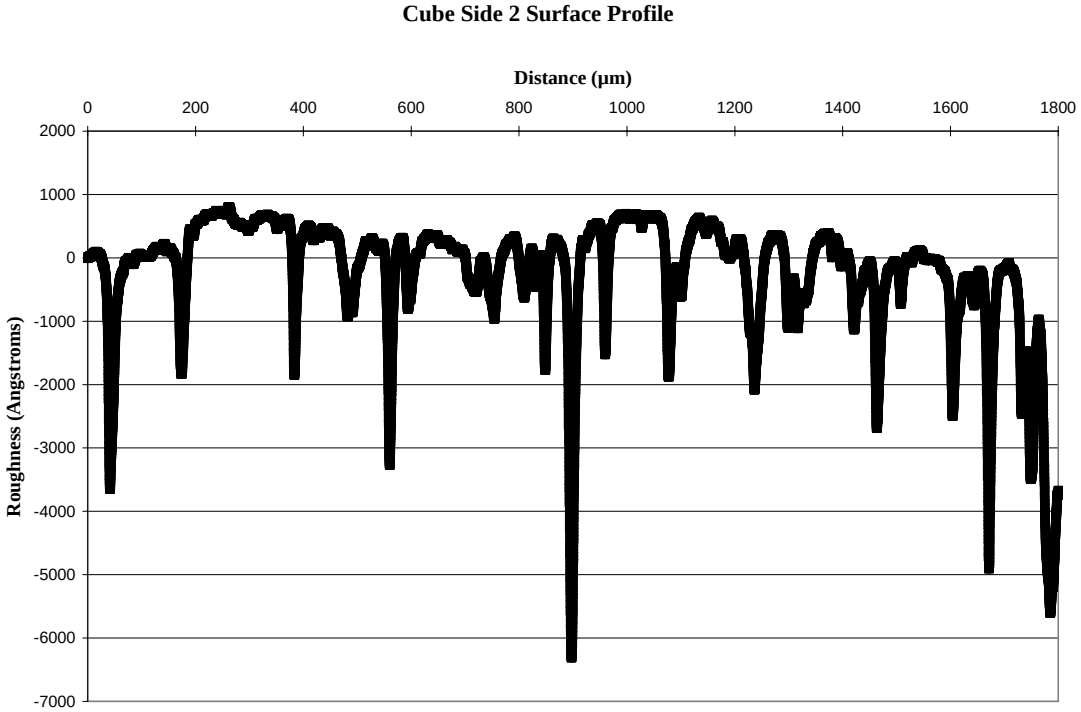

Cube Side 3 Surface Profile

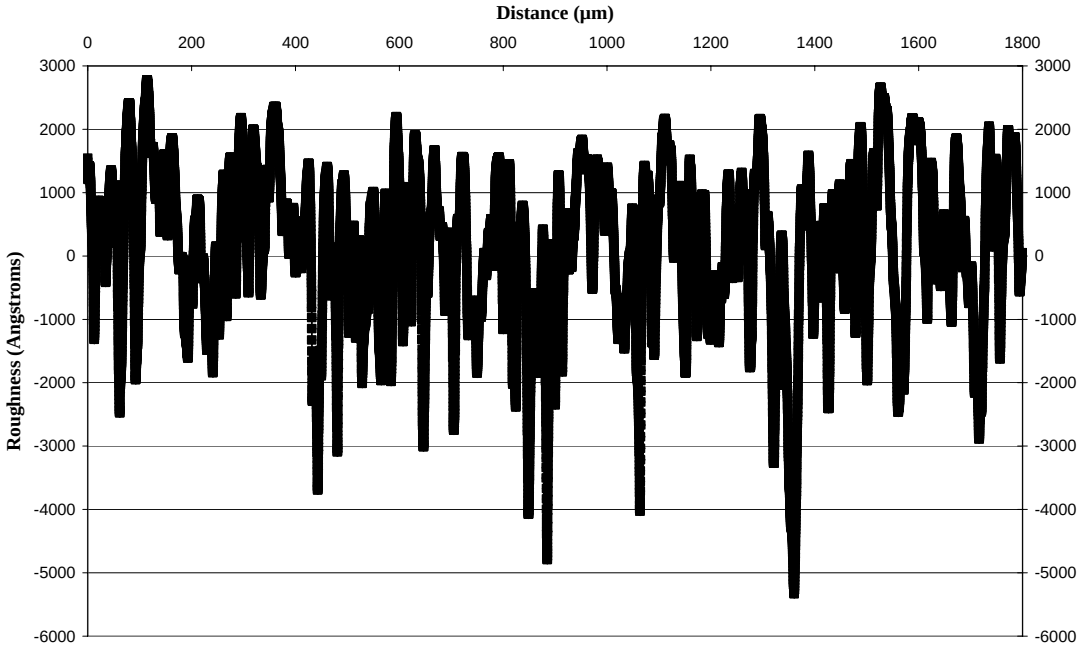

Cube Side 4 Surface Profile

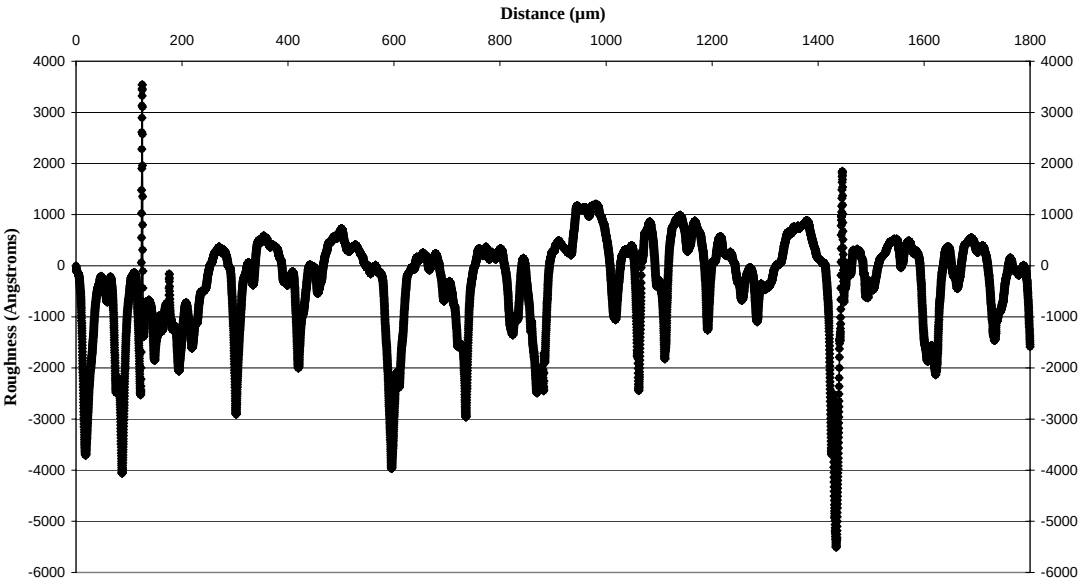

Cube Side 5 Surface Profile

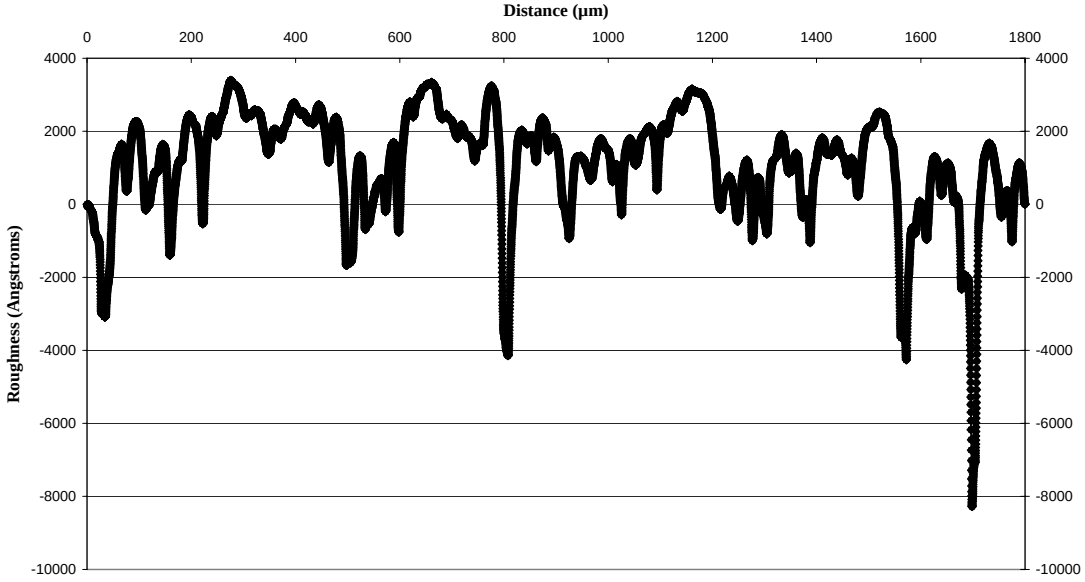

Cube Side 6 Surface Profile

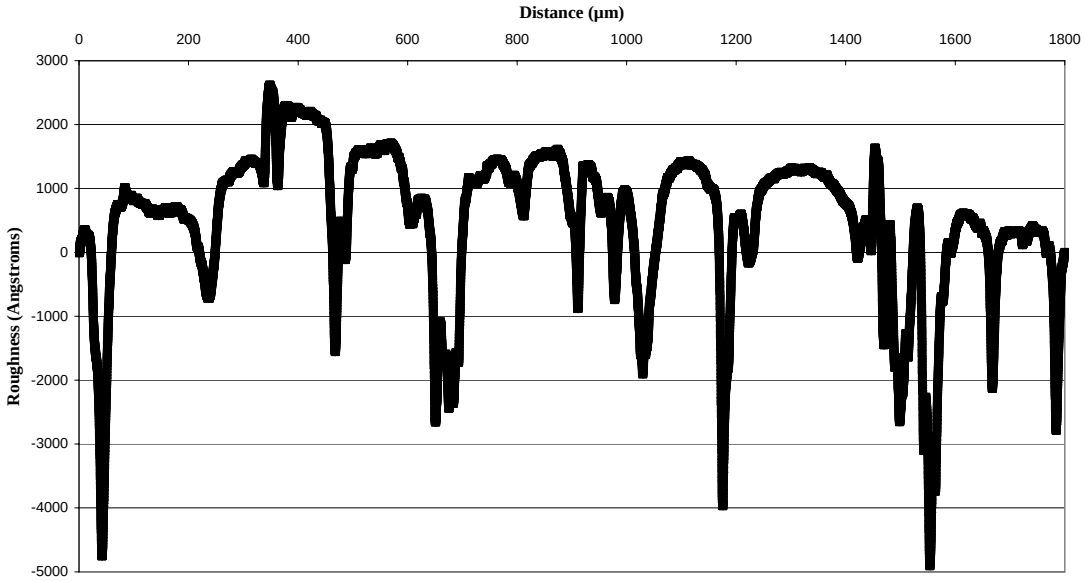

Crystal 2

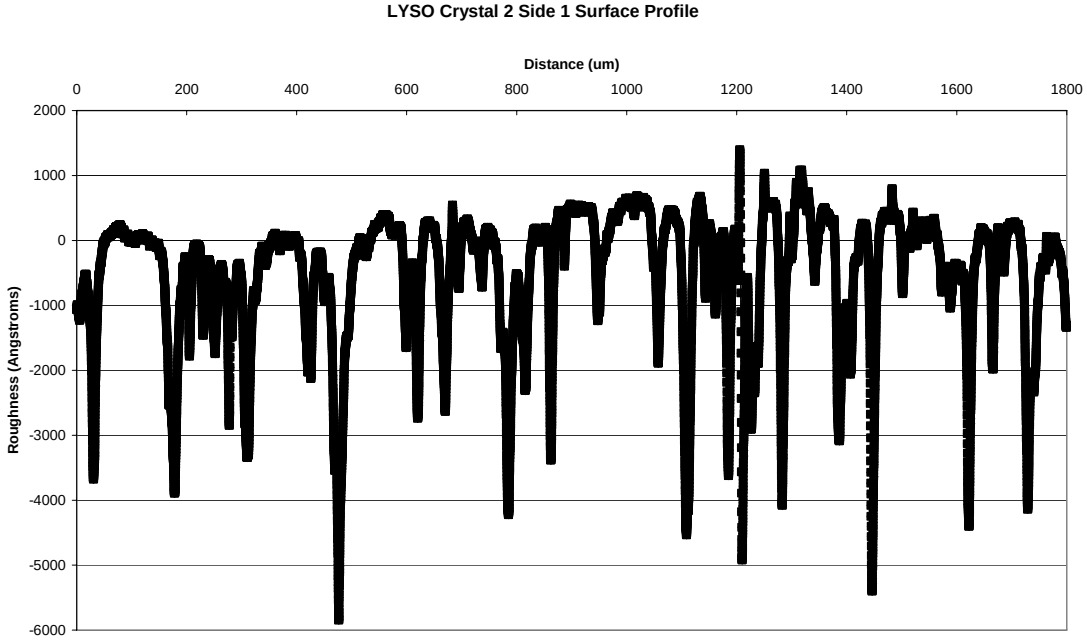
LYSO Crystal 2 Side 1 Surface Profile
Distance (um)
0
200
400
600
800
1000
1200
1400
1600
1800
2000
1000
0
-1000
-2000
-3000
-4000
-5000
-6000
Roughness (Angstroms)

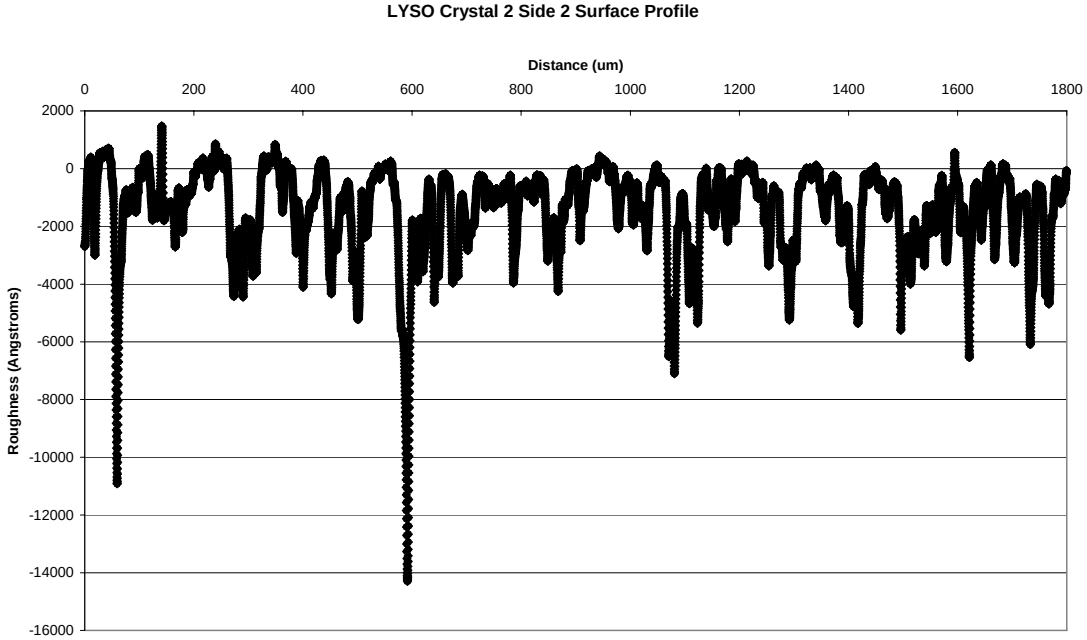
LYSO Crystal 2 Side 2 Surface Profile
Distance (um)
0
200
400
600
800
1000
1200
1400
1600
1800
2000
0
-2000
-4000
-6000
-8000
-10000
-12000
-14000
-16000
Roughness (Angstroms)

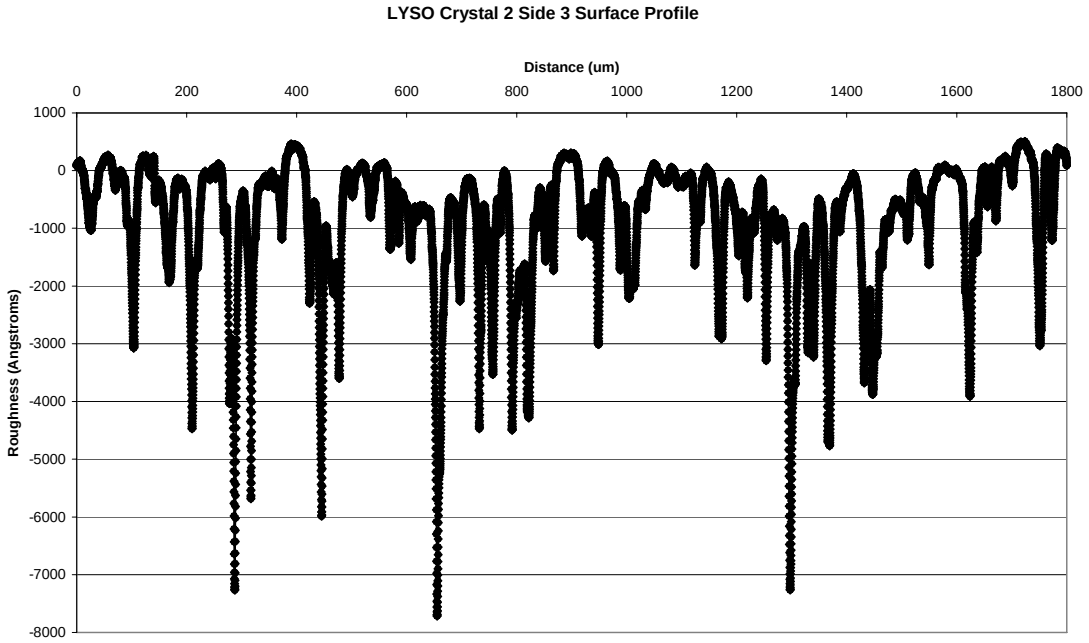
LYSO Crystal 2 Side 3 Surface Profile
Distance (um)
0
200
400
600
800
1000
1200
1400
1600
1800
1000
0
-1000
-2000
-3000
-4000
-5000
-6000
-7000
-8000
Roughness (Angstroms)

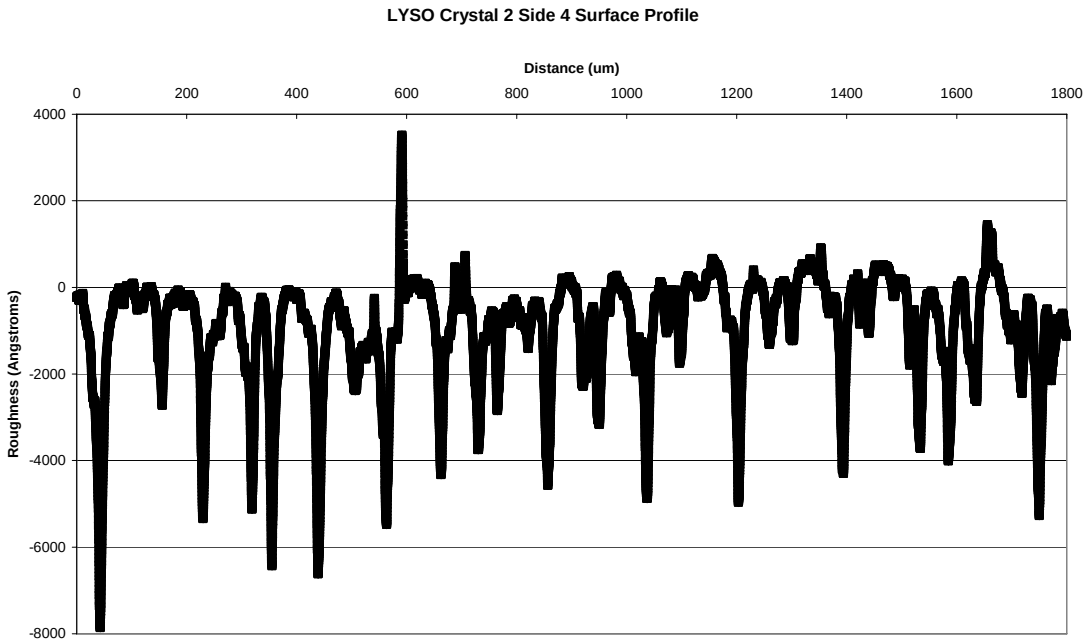
LYSO Crystal 2 Side 4 Surface Profile
Distance (um)
0
200
400
600
800
1000
1200
1400
1600
1800
4000
2000
0
-2000
-4000
-6000
-8000
Roughness (Angstroms)

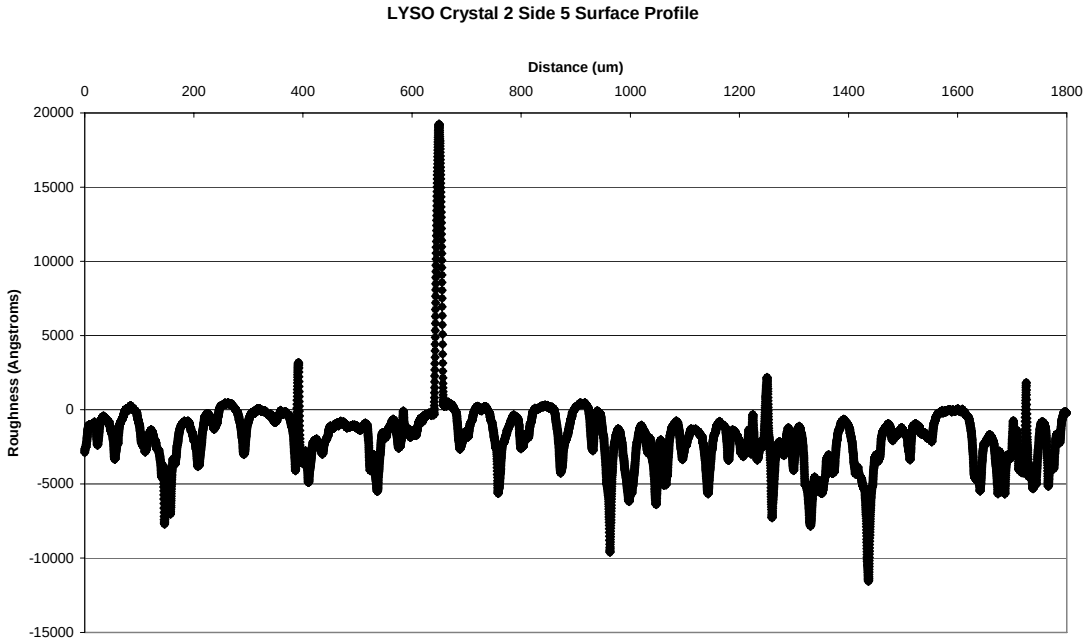
LYSO Crystal 2 Side 5 Surface Profile
Distance (um)
0
200
400
600
800
1000
1200
1400
1600
1800
Roughness (Angstroms)
20000
15000
10000
5000
0
-5000
-10000
-15000

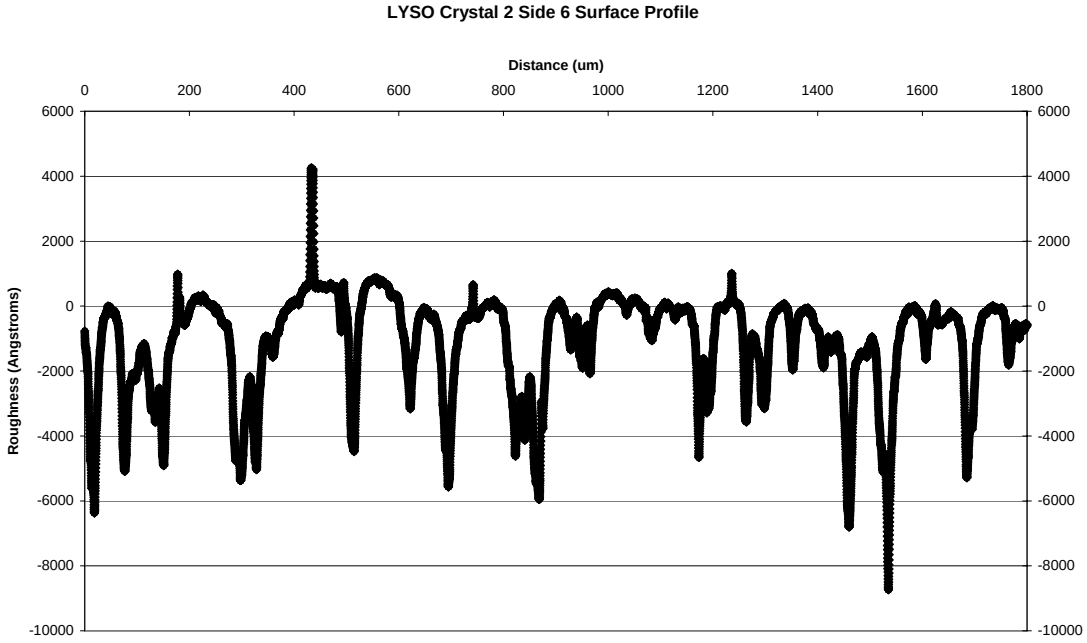
LYSO Crystal 2 Side 6 Surface Profile
Distance (um)
0
200
400
600
800
1000
1200
1400
1600
1800
Roughness (Angstroms)
6000
4000
2000
0
-2000
-4000
-6000
-8000
-10000

Appendix 2 – Simulation Input File Examples:

Scintillation Program –

```
1       -575    30000
3        3
r c     1.0     0.0257          f n
r c     1.0     0.0250          f n
r c     1.0     0.0140          f n
r c     1.0     0.0158          f n
r c     1.0     0.0163          f n
s d     1.53    0.0144          t n
0.93    0.93    1       1.81
90
S4G5L46.TXT
```

DETECT2000 -

```
;3x3x3mm LYSO crystal with SPAD4 PD

FLAG,0FAST_QE,1VERBOSE

DMAT1, 1.810N,400.0AD,400.0SD,1PLF,DT1,40TAU,1.0TAUW        ;LYSO
DMAT2, 1.620N                                               ;Grease
DMAT3, 1.950N                                               ;Si3N4
DMAT4, 1.463N                                               ;SiO2
DMAT5, 4.600N                                               ;Si

DFIN1,DETECT                    ;Detector Sensitive Surface
DFIN2,PAINT,0.93RC              ;Paint Surface Finish
DFIN3,POLISH                    ;Smooth Surface Finish
DFIN4,GROUND                    ;Rough Surface Finish

DPLN1,-1.5X                     ;-1.5mm in X dir
DPLN2,1.5X                      ; 1.5mm in X dir
DPLN3,-1.5Y                     ;-1.5mm in Y dir
DPLN4,1.5Y                      ; 1.5mm in Y dir
DPLN5,0.0Z                      ; top of crystal
DPLN6,3.0Z                      ; 3mm crystal in Z dir
```

```
DPLN7,3.000001Z          ; 1nm Optical Grease
DPLN8,3.0000625Z         ; 61.5nm Si3N4 in Z dir
DPLN9,3.0001375Z         ; 75nm SiO2 in Z dir
DPLN10,3.0001975Z        ; 60nm Si in Z dir - detect layer

COMP1,MAT1               ;Crystal
SURF,FIN2,PLN1,XL
SURF,FIN2,PLN2,XS
SURF,FIN2,PLN3,YL
SURF,FIN2,PLN4,YS
SURF,FIN2,PLN5,ZL
SURF,FIN3,PLN6,ZS,C2

COMP2,MAT2               ;Optical Grease Layer
SURF,FIN2,PLN1,XL
SURF,FIN2,PLN2,XS
SURF,FIN2,PLN3,YL
SURF,FIN2,PLN4,YS
SURF,FIN3,PLN6,ZL,C1
SURF,FIN3,PLN7,ZS,C3

COMP3,MAT3               ;Si3N4 Layer
SURF,FIN2,PLN1,XL
SURF,FIN2,PLN2,XS
SURF,FIN2,PLN3,YL
SURF,FIN2,PLN4,YS
SURF,FIN3,PLN7,ZL,C2
SURF,FIN3,PLN8,ZS,C4

COMP4,MAT4               ;SiO2 Layer
SURF,FIN2,PLN1,XL
SURF,FIN2,PLN2,XS
SURF,FIN2,PLN3,YL
SURF,FIN2,PLN4,YS
SURF,FIN3,PLN8,ZL,C3
SURF,FIN3,PLN9,ZS,C5

COMP5,MAT5               ;Detect Layer
SURF,FIN2,PLN1,XL
SURF,FIN2,PLN2,XS
SURF,FIN2,PLN3,YL
SURF,FIN2,PLN4,YS
SURF,FIN3,PLN9,ZL,C4
SURF,FIN1,PLN10,ZS

LIFE10000
```

```
FATES5
SEED1
GEN,MAT1,1.5XS,-1.5XL,1.5YS,-1.5YL,0.0ZS,3.0ZL     ;Photon Generation Point
RUN30000                                           ;Photons Generated

END
```